MICROWAVE CIRCUIT ELECTRIC FIELD IMAGING SYSTEMS

by

Thomas Philip Budka

A dissertation submitted in partial fulfillment
of the requirements for the degree of
Doctor of Philosophy
(Electrical Engineering)
in The University of Michigan
1995

Doctoral Committee:

Associate Professor Gabriel M. Rebeiz, Chair
Research Scientist Jack R. East
Associate Professor Karem A. Sakallah
Professor Fawwaz T. Ulaby

To my parents

ACKNOWLEDGEMENTS

This level of achievement would not have been possible without the constant loving support and self-sacrifices of my mother (Phyllis), my father (Alfred) and my wife (Sandy). I would like to thank my brother (Ken) and sister (Chris) for sharing their moral support during all of the struggles in the pursuit of higher education. My thanks to all of my friends and family for their support of my work.

I would like to thank Scott Waclawik for his excellent engineering support in building the 2-18 GHz RF Imager, the filter and the directional coupler tested in this dissertation. For their very helpful discussions about this work, I would like to thank Chen-Yu Chi, Daniel Ross, Brian Kormanyos, Emmanouil Tentzeris, Jian Gong and Curtis Ling. It was a pleasure working with fellow graduate students: Scott Barker, Andy Brown, Alan Courtay, Rhonda Drayton, Dan Filipovic, Gildas Gauthier, Rashaunda Henderson, Katherine Herrick, Steve Mollenkopf, John Papapolymerou, Sanjay Raman, Steve Robertson, and Tom Weller. For their expert help with semiconductor fabrication, I would like to thank Steven Gearhart, Walid Ali-Ahmad, Phil Marsh, Changshun Kim, Jeff Kempisty, Terry Hull, Janet Robertson and Christine Mason. I would also like to thank The Radiation Laboratory faculty, students and staff for creating an excellent working environment for graduate study. This work was funded by The NASA Center for Space Terahertz Technology. I especially would like to thank Gabriel Rebeiz for his animated enthusiasm, for his enlightening discussions, for his sense of humor, and for the confidence he placed in me to pursue the ideas presented in this thesis.

PREFACE

At present there are no commercially available methods of mapping the near electric fields above planar circuits that operate at frequencies higher than 500 MHz and give better than 1 mm spatial electric field resolution. This thesis presents a low-cost and wide-bandwidth methods for experimentally mapping electric fields above microwave circuits with spatial resolutions of 100 μm at heights less than 20 μm above the surface. The emphasis of this work has been on reducing the electric field imaging system cost and increasing the system's ease of use, thereby increasing the system's possible acceptance as a diagnostic tool in the microwave industry. With this goal in mind, an indirect method of measuring the electric field above a microwave circuit (modulated scattering) was chosen. There are drawbacks in using an indirect measurement method, however, since the system is completely coaxial, compatible with present network analyzer testing techniques and easy to use, the benefits of the information received from an indirect electric field map far outweigh the drawbacks.

TABLE OF CONTENTS

LIST OF FIGURES

Figure

LIST OF APPENDICES

Appendix

CHAPTER I

INTRODUCTION

Presently most standard testing techniques for monolithic microwave integrated circuits (MMIC) involve on-wafer probing where the device under test (DUT) is contacted at several ports outside the circuit. Using common calibration techniques such as Through-Reflect-Line (TRL) and Line-Reflect-Match (LRM), the scattering parameters (S-parameters) of the DUT can be determined. S-parameter measurement systems have been demonstrated up to W-band with passive probing [1]-[3] and extending the operating frequency of these S-parameter measurement systems appears promising with active non-linear transmission lines [4]-[6]. These methods of characterization are adequate for single chips or devices, but as the complexity of the circuit increases, knowledge of the operation of the individual components does not guarantee that the combined circuit will perform as expected.

Both active and passive probes yield important S-parameter information for microwave circuit design but fail to describe the internal operation of devices contained within a MMIC. The mapping of the electromagnetic fields above a MMIC can be of great importance in detecting electric field magnitude, electric field direction, phase information, substrate modes and device to device interactions. With a map of the electric field intensity above the substrate, one can define low electric field regions around a device that could be used for placement of more circuitry, thus saving valuable chip real-estate. With tighter control over line lengths and losses that may be derived from electric field intensity and

phase maps, it may be possible to reduce the number of iterations during the design of MMIC's and multi-chip modules (MCM). Currently, electromagnetic field mapping is possible with electro-optic sampling [7]-[16], photo-emission sampling [18], electron-beam sampling [19], [20], scanning force microscopy [21]-[23], passive detection schemes [24]-[25] and modulated scattering [26]-[33]. Electro-optic, photo-emission and electron-beam sampling are generally time-domain methods where the electric field time waveform at each point above the circuit must be stored to generate a complete electric field image of the DUT. The latter methods (scanning force microscopy, passive detection and modulated scattering) are frequency domain methods where the DUT is tested at a specific frequency of interest. The electric field phase and magnitude at each frequency of interest must be stored to have a complete picture of the DUT's operation. By using the modulated scattering technique, the direction, magnitude and phase delay of the electric fields at each position over a DUT can be determined up to very high operating frequencies (500 GHz).

It is the author's opinion that of all the electromagnetic field detection methods at present, the easiest to implement and the best results will be obtained through the use of the modulated scattering method proposed in the 1950's by Richmond [26], Cullen and Parr [27], and Justice and Rumsey [28] and applied to planar microwave circuits by Zürcher [29] in 1992. This thesis introduces and explains in detail the method of electromagnetic field mapping through modulated scattering. In Chapter I, various methods of electric field mapping of microwave circuits are presented and explained. In Chapter II, the method of modulated scattering that has been used for this dissertation is explained in detail. A coaxial measurement system is described that is used for electric field mapping of microwave circuits in the frequency range of 500 MHz to 18 GHz. Next a quasi-optical modulated scattering system is proposed that can be used with radiating circuits. The

design and fabrication of hybrid probes and integrated probes is discussed as well as their invasiveness to the DUT. In Chapter III, the theory of modulated scattering is developed and explained. The response of a dipole probe versus height above a microstrip line is presented and is shown to match well with calculated results. In Chapter IV, results of the coaxial modulated scattering system are presented over 50 Ω transmission lines (microstrip and CPW) with different terminations: load, short and open. These results are compared with the theory of operation and verify the operation of the modulated scattering system. Also, electric field maps from a patch antenna, a meander line and a -12 dB directional coupler are presented and compared with the expected mode of operation for these circuits. In Chapter V, studies of all components of the electric fields over a three stage coupled line filter are presented and compared with the calculated electric fields from the finite difference time domain (FDTD) technique.

1.1 Electro-Optic Sampling

The method of electro-optic sampling is a proven technique to measure the electric fields over high frequency circuits. Electro-optic crystals, such as gallium arsenide (GaAs), potassium dihydrogen phosphate (KDP) and lithium tantalate (LiTaO3), change their indices of refraction when an electric field is present. The relationship between electric field and index of refraction can be summarized in the following equation [15]:

$$\Delta\left(\frac{1}{n^2}\right) = rE + PE^2 \tag{1.1}$$

where the linear term is associated with Pockels effect and the quadratic term is associated with the Kerr effect. If the orientation of an electro-optic crystal, such as a KDP crystal, is chosen properly where the Kerr constant (P) is very small, the following simple relations

can be derived between the electric field intercepted by the crystal and the crystal's index of refraction along a specific axis [15]:

$$n_x = n_o + \frac{n_o}{2} r E_z \tag{1.2}$$

$$n_y = n_o - \frac{n_o}{2} r E_z \tag{1.3}$$

From these relations, if a circularly polarized beam of light is incident upon an electro-optic crystal of the proper orientation, an elliptically polarized beam will be reflected. The stronger the electric field in the z-direction, the greater the deviation of the reflected light from circular polarization. Thus it is possible to perform a measurement of the normal electric fields within an electro-optic crystal with these simple relations. In order to measure the tangential electric fields, a properly oriented GaAs crystal is typically employed [12].

Figure 1.1 displays the two methods that emerge for measuring the electric fields of microwave circuits by exploiting the electro-optic effect at GHz frequencies. Either the microwave substrate itself is used as the electro-optic crystal (direct electro-optic sampling) in figure 1.1a) or an electro-optic crystal is used as a probe and is placed above a microwave circuit (indirect electro-optic sampling) in figure 1.1b). With direct electro-optic sampling, the microwave circuit to be tested must not have a ground plane if it is to be illuminated from the back side of the wafer (typically GaAs). Although backside illumination is a noninvasive method, the system is limited to transmission lines and circuits that either have no lower ground plane such as coplanar waveguide and coplanar strip transmission lines or have a ground plane that is transparent to the laser illumination such as indium tin oxide (ITO) [13]. The backside illumination method also suffers in the spatial resolution of the measured electric field because the circularly polarized beam of light

must travel through the entire substrate before it is reflected back. The measured electric field must therefore be deembedded from the integrated effect of the beam travelling through a region of constantly varying index of refraction as the electric fields decay away from the conducting lines of the circuit. It is often difficult to deembed this information and this limits the performance and applicability of the direct electro-optic sampling technique. If the wafer is to be illuminated from the front side of the wafer, then the only valid test regions would be in areas where the electro-optic substrate is exposed. This limitation prevents the measurement of the fields over conducting lines and ground planes on the patterned side of the DUT.

For the case of indirect electro-optic sampling, a 100-200 μm thick electro-optic crystal is placed in close proximity with a microwave circuit [12] or antenna [16]. The electro-optic probe tip is then moved over the microwave circuit and an electric field map of the normal fields (with a KDP probe) and the tangential fields (with a GaAs probe) can be collected [12]. Typically, the electro-optic crystal is brought into contact with the DUT for mapping of the electric field waveform [17]. In order for indirect electro-optic sampling to become a viable technology for commercial use, a smaller probe tip and lower dielectric constant electro-optic crystal must be found and a lower cost pulsed laser must be developed.

Cheng et. al. [9], [10] have demonstrated an electro-optic sampling technique up to frequencies greater than 1 THz by integrating a thin, low temperature grown GaAs (LT-GaAs) film with the microwave circuit. This technique is compatible with microwave substrates such as quartz, silicon and alumina but is not compatible with commonly used PTFE (polytetrafluoroethylene) substrates such as Roger's RT/duroid™. The thin film

a)

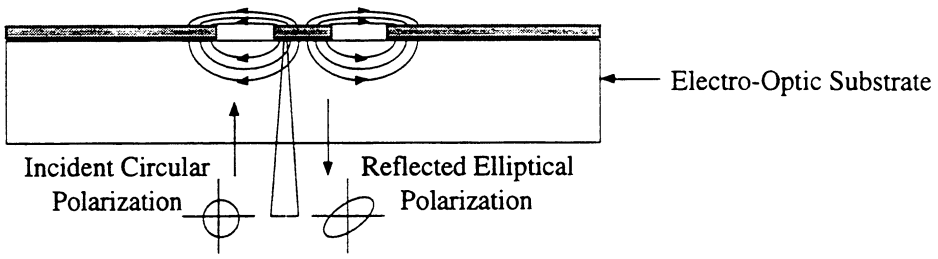

b)

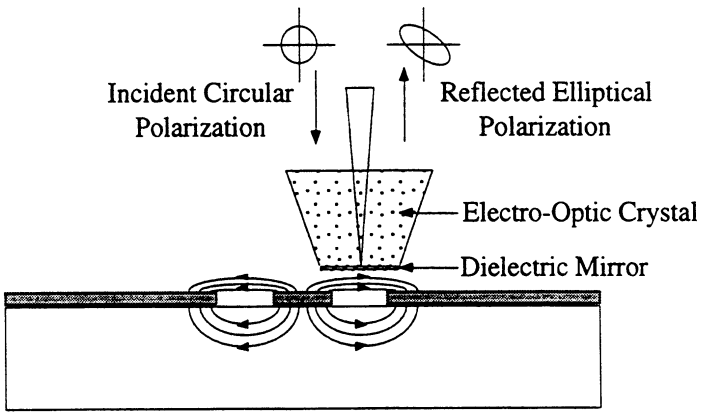

Figure 1.1: a) Direct electro-optic sampling technique where the substrate is used as the electro-optic crystal. b) Indirect electro-optic sampling technique where a 100 μm thick electro-optic crystal is placed in close proximity to the microwave circuit.

is used to produce an electrical impulse along a transmission line [10] and is bonded to a quartz substrate by the Van der Waals force. Once bonding is completed, the rest of the circuit can be fabricated on top of this layer. The measurements were performed on coplanar strip (CPS) where pulses were measured in the time domain at various distances away from the region where the pulse was created. To create a pulse, the lines of the CPS are DC biased, a pulse of light liberates highly mobile electric charges in the LT-GaAs strip that momentarily short-circuits the CPS line. The sharp electrical pulse propagates along the transmission line and is detected by a $LiTaO_3$ electro-optic sampling probe that samples the electric fields above the CPS line or capacitive gap in the time domain [9].

1.2 Electron Beam Sampling

Another method of sampling the electric fields around a microwave circuit is the technique of electron beam sampling. In reference [19], a scanning electron microscope is operated in stroboscopic mode at 9.0 GHz with a beam diameter of 0.3 μm and with beam pulse lengths of 10 ps. Through high frequency pulsing of the electron beam, secondary electrons scattering from the DUT are accelerated across a grid and then viewed as a function of their energy spectrum. The energy spectrum of the secondary electrons shifts linearly with the voltage at the point of emission [20]. Elaborate microwave bunchers and beam blanking systems are necessary at X-band and the resolution of this type of system is limited by the transit time of the electrons in the dynamic RF field [20]. To date, this method of testing has been successful in the characterization of discrete Gunn diode oscillators [19] and with the mapping of coplanar strip and coplanar waveguide lines [20]. Cost considerations of operating a special scanning electron microscope and the difficulty of testing a microwave circuit in vacuum will ultimately limit the widespread acceptance of this technique.

1.3 Photo-Emission Sampling

A similar electric field mapping technique is photo-emission sampling. This method is a hybrid between electron beam testing and electro-optic sampling. By exploiting the multiphoton photo-electric effect induced by a continuous wave (CW) mode-locked laser, sampling the time domain voltage waveform on a simple transmission line is possible. By studying the energies of the electrons emitted from the surface of the strip, the emission point potential at the arrival time of the laser pulse can be determined. The voltage waveform can be determined with picosecond resolution and millivolt sensitivity. The time (frequency) resolution is better than 40 ps (25 GHz). As with the technique of electron beam sampling, electrons are collected after being accelerated past an extraction grid. The magnitude of the electron energy is proportional to the local voltage on the line [18]. This technique can only measure the voltages along conductors and is not capable of mapping the electric fields over dielectrics. Photoemission sampling is an extremely expensive measurement technique for mapping the voltages over microwave circuits and is not expected to gain acceptance as a standard tool in the microwave circuit industry.

1.4 Passive Electric Field Detection

There are many techniques of passive detection of the electric fields over microwave circuits. Typically a small antenna (dipole, monopole, loop etc...) is scanned over the DUT and weakly couples a small RF signal into a power detector such as a bolometer, diode video detector or a spectrum analyzer. By using a power detector, only the intensity of the intercepted electric field may be measured by a simple antenna. Passive electric field detection systems are capable of operating over decades of bandwidth. Thin film micro-bolometers have been demonstrated to detect power at terahertz frequencies by

Neikirk [35] and Gearhart [36]. If intensity information of the electric field is the only desired information, then a passive electric field detection system should be chosen.

Osofsky and Schwarz [24] describe a noncontacting magnetic field probe for use in the internal characterization of microwave circuits. In their experiment, a double loop magnetic field probe is fabricated and operated in the frequency range of 0.1 GHz to 0.3 GHz. By using a double loop instead of a single loop, the contribution to the detected magnetic field of a distant radiating source will be minimized because these fields will tend to cancel in the loops [24]. Tests are performed over microstrip and coplanar waveguide transmission lines and showed promising results. Gao and Wolff [25] present magnetic field maps over microstrip lines at 20 GHz by using a single loop (710 μm by 710 μm) at a height of 200 μm above the circuit. The experimental system uses a network analyzer as the detector and an automated computer controlled motor for probe positioning. The large size of the loop and the height at which tests were performed limit the resolution of this type of probe; however, other probes could be designed with finer dimensions and would work well with this technique. Because the RF signal is received by the probe which has been connected to a 50 Ω transmission line, this technique will tend to load the circuit more than an indirect sampling technique such as modulated scattering.

1.5 Scanning Force Microscopy

The technique of scanning force microscopy shows promising results for measuring the normal electric fields over microwave circuits in frequency domain. A system is currently commercially available from Park Scientific Instruments [21] and has been demonstrated by Mueller [22], Böhm [23] and other groups. Figure 1.2 displays a typical experimental setup used for scanning force microscopy (SFM). A cantilever arm with a

needle-like tip is placed in close proximity to a microwave circuit. The cantilever arm is typically resonant at a low frequency (f_{res} between 1 KHz and 20 KHz). If the DUT is operating at a high frequency, (f), and a slightly higher frequency signal, ($f+f_{res}$), is applied to the cantilever arm, the cantilever arm will oscillate with an amplitude proportional to the amplitude of the normal electric field intercepted by the tip of the SFM. The amplitude of this oscillation is determined by measuring the deflection of a HeNe laser that is focused on the tip of the cantilever arm. A disadvantage of this system is that two high frequency synthesized oscillators are needed, one for the circuit and one for the SFM probe. Although this method works fairly well with normal electric fields, implementing a tangential electric field probe with this technique will be very difficult. Another disadvantage of this system is that the cantilever arm is quite large (100 μm wide by 1000 μm long) its effects on the DUT will be difficult to deembed from the measurements over complex circuits. Unlike the other electric field mapping systems for microwave circuits, the cost of implementing SFM is relatively low.

1.6 Modulated Scattering

A convenient technique for measuring the electric fields around horn antennas, called modulated scattering, was developed by several groups in 1955 (Richmond [26], Cullen et al. [27] and Justice et al. [28]). Figure 1.3 displays the experiment used by Richmond [26] to map the near-fields of pyramidal horn antennas at 9.4 GHz. A small dipole scatterer with a diode mounted at the center is placed in the near field of the antenna of interest. By modulating the bias of the diode at a frequency much lower than the radio frequency (RF), a modulated scattered RF signal returns to the transmitter. By using the transmitter as a receiver, the modulated signal can be detected with little or no distortion of the antenna's field pattern. The strength and phase of the scattered signal is directly

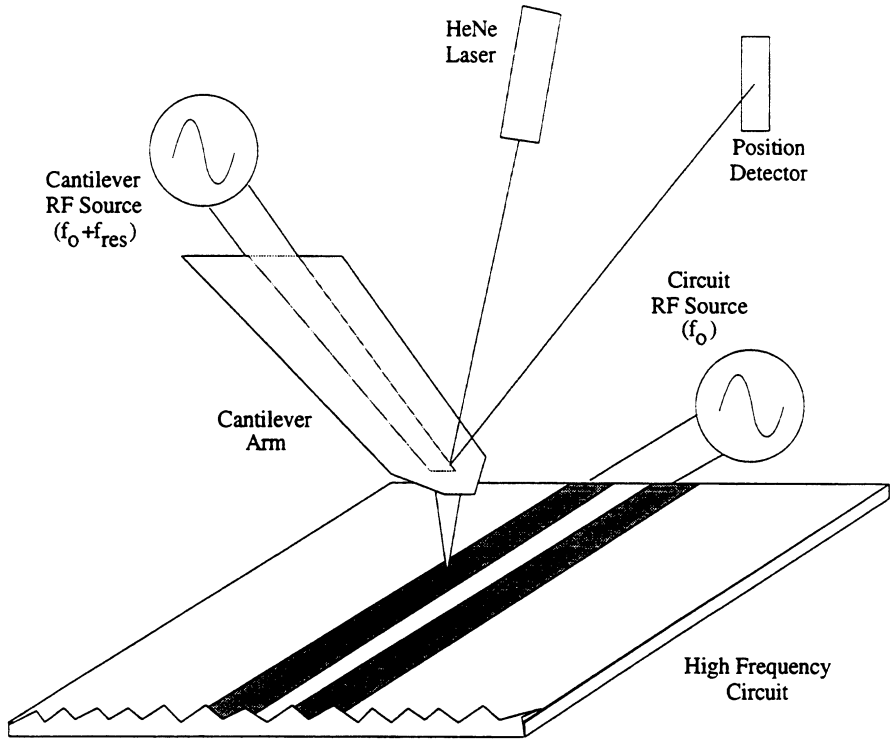

Figure 1.2: Scanning force microscopy system used by Park Scientific Instruments [21] for measuring the normal electric field over high frequency circuits.

proportional to the square of the electric field intercepted at the position of the dipole probe [26]. In the experiment, Richmond used a magic-tee waveguide junction at the feed of the antenna to isolate the transmitted signal from the detector and to direct the received scattered signal to the detector. The scattering probe's effect on the electric fields is minimized by using slightly conducting nylon thread for biasing the diode [26].

Richmond's method was adapted by Zürcher in 1992 to probe the tangential near fields of microstrip circuits (patch antennas and hybrid couplers) at frequencies in the range of 1.4-2.2 GHz [29]. In Zürcher's experiment (see Figure 1.4), a 3-dB hybrid microstrip coupler (instead of a magic-tee waveguide junction) is used to couple the reflected signal into a quadrature mixer detector. The advantage of Zürcher's system is that it is completely coaxial. This reduces the cost and improves the utility of the system for microwave circuit characterization. The power divider, microstrip coupler, and quadrature mixer are fabricated on the same substrate and limit the operating bandwidth of the system. As with Richmond's experiment, this method loses half of the reflected modulated signal from the 3-dB coupler. Zürcher also does not mention how the electric field phase is calculated. This dissertation will show that the measured phase is a net electrical phase delay of the "round trip" path from the input port to the point of interest.

In this dissertation, the basic theory of operation of a modulated scattering experiment is presented. An improved modulated scattering system that uses a wideband circulator to maximize the signal to noise ratio and operating bandwidth is also described. In addition to looking at the reflected signal, more information of the DUT's operation can be determined from the transmitted signal as well with minimal loss in scattered signal amplitude.

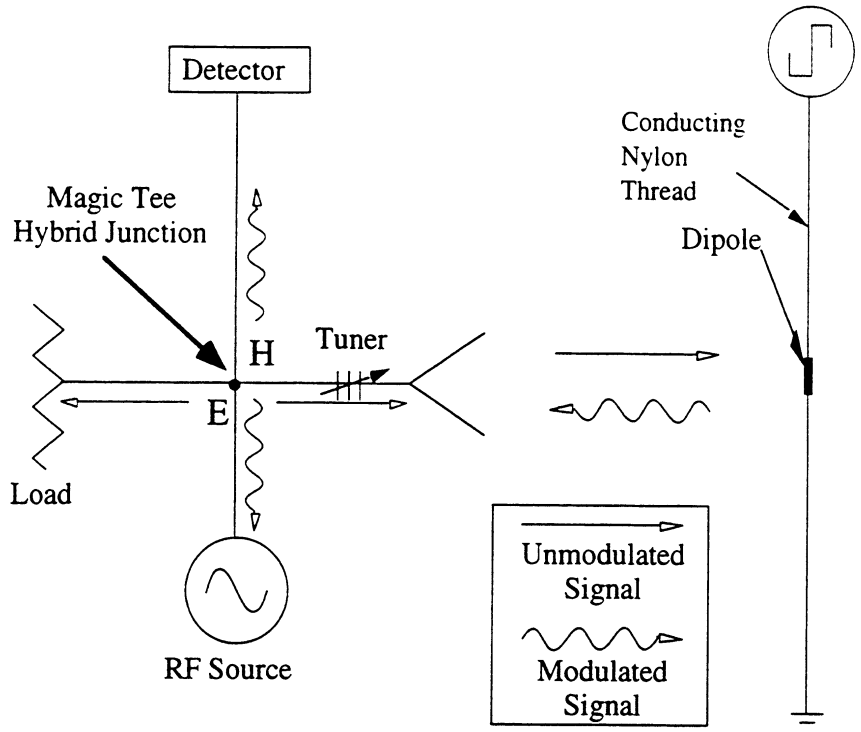

Figure 1.3: Apparatus for electric field measurements of antennas with the modulated scattering technique of Richmond [26].

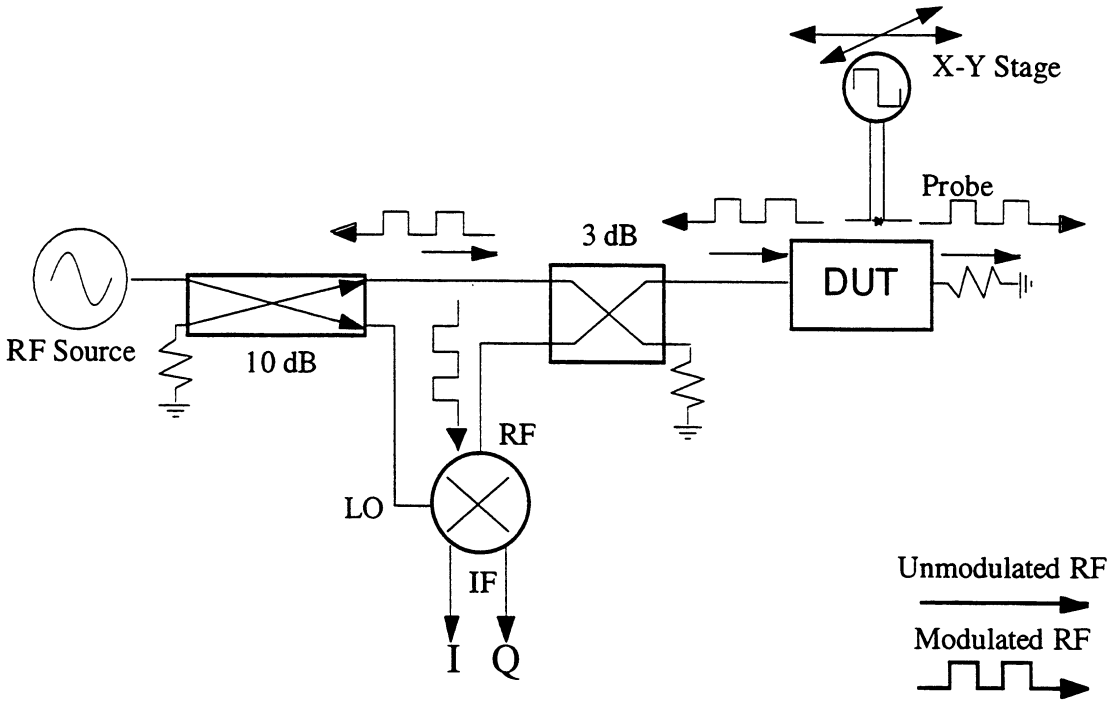

Figure 1.4: The modulated scattering system used by Zürcher to map the near electric fields over planar microwave circuits in the frequency range of 1.4 GHz to 2.2 GHz [29].

1.7 Summary of Present Electric Field Mapping Techniques

Any experimental technique will have limitations depending on the application and the desired emphasis on resolution, bandwidth, compatibility, adaptability, etc.... Table 1 summarizes and compares the six microwave circuit diagnostics for internal characterization of microwave circuits. The first item, *Domain (Frequency or Time)*, specifies the domain which the measurement takes place. If narrow pulses are used to synchronize the measurement with an RF signal, the technique is labelled as a time-domain technique. If mixers are used to extract an intermediate frequency (IF) whose amplitude and/or phase is measured, then the technique is labelled as a frequency-domain technique. If the operation of a circuit over one cycle is nonlinear, generally, a time domain method is most applicable for internally characterizing the circuit. The second item, *Highest Estimated Measurable Frequency*, is the author's estimate of the highest frequency operating point of the technique given the currently available technology. The third item, *Uncorrected Electric Field Resolution (microns)*, is the author's estimate of the spatial electric field resolution of a measurement without correction or data processing. The fourth item, *Probe Invasiveness*, is a qualitative assessment of how much the probe will perturb the operating point of the DUT either in the form of a frequency shift or an increase/decrease in the reflected/transmitted power through the DUT. The fifth item, *Relative Cost to Implement*, is the author's qualitative assessment of the costs involved in building, maintaining and operating an electric field mapping system. The sixth item, *Bandwidth Rating*, describes the operating frequency ranges of the microwave circuit characterization systems. The seventh item, *Compatibility with Standard Techniques*, is an assessment of the compatibility of the mapping system with microwave network analyzer tests and rates how well the technique would fit with a probe station measurement. The eighth item, *Adaptability of Testing Technique for MMIC's*, assesses the applicability of the characterization technique

to the wide variety of MMIC's currently being fabricated. The ninth item, *Ease of Implementation*, rates how easily a system could be built, maintained and operated by a microwave engineer in a research and development laboratory. The tenth item, *Noise Rating*, is a qualitative measure of the output signal from the system and an estimate of the obtainable signal to noise ratio (SNR). A mechanical system will have the highest noise level, such as scanning force microscopy, and a homodyne mixing system will have the lowest noise level, such as modulated scattering. The eleventh item, *Microwave Circuit Compatibility*, describes what types of circuits can be tested with each technique. The twelfth item, *Field Information : Magnitude and/or Phase*, describes what information about the electric field is detectable with each technique. The thirteenth item, *Measurable Electric Field Components*, describes which components (normal and/or tangential) of the electric field each technique is able to measure.

From the table, it is clear that the most practical methods for mapping the electric fields in magnitude and phase over a microwave circuit are indirect electro-optic sampling, scanning force microscopy and modulated scattering. Passive techniques will prevail if only intensity information is desired. The indirect electro-optic sampling technique is the best choice for circuits with nonlinear waveforms in the time domain, however, the main limitations of the electro-optic sampling techniques are the costs involved in operating a pulsed mode-locked laser and related optics and the necessity of contacting a typically high dielectric constant electro-optic probe with the DUT. The scanning force microscopy method requires two stable microwave sources for operation and can only map the normal electric fields over microwave circuits. Also, due to the mechanical nature of the SFM experimental system, the technique will more likely be noise limited and have less dynamic range than an electrically coupled system. It is the author's opinion that the modulated scattering technique is the technique of choice for mapping the electric

fields over linear microwave circuits at frequencies below 200 GHz. The system detects a weakly coupled microwave signal from either a dipole, monopole or loop antenna and is adaptable to many different microwave circuits operating in the linear mode (antennas, amplifiers, mixers, oscillators, etc...). Because this system is modular, it is adaptable to any probe (electric or magnetic) with a modulating impedance state and is capable of mapping the fields near passive as well as active microwave circuits. The modulated scattering technique is limited to circuits with less than 30 dB of loss from the input port to the point of interest. This limitation will be demonstrated and explained Chapter III.

In this dissertation, a near-field detection system is presented that improves upon the modulated scattering techniques used by Richmond [26] and Zürcher [29]. The system can be used to simultaneously detect normal and tangential electric field intensities and the net electrical phase delay within a microwave circuit. A wideband experimental electric field imager that can be used as a tool for MMIC diagnostics is explained in detail. With these presented systems, full two dimensional electric field maps can be generated and images of a MMIC's operation with respect to small changes in frequency can be studied. Complete knowledge of the electrical phase delay of each region of the circuit with respect to any port can be determined and compared with electrical phase delays at other frequencies. The systems built for this research currently work from 500 MHz to 2.0 GHz and from 2 GHz to 18 GHz and can be extended for operation up to 60 GHz using a coaxially based system. At frequencies above 60 GHz, a modulated scattering quasi–optical system for measuring the electric fields around a MMIC that is coupled to an antenna is proposed.

TABLE 1. Comparison of present day electric field mapping techniques.

	Direct Electro-Optic Sampling	Indirect Electro-Optic Sampling	Electron Beam Sampling	Photo-Emission Sampling	Scanning Force Micro-scopy	Modulated Scattering
Domain (Frequency or Time)	Time Domain	Time Domain	Time Domain	Time Domain	Frequency Domain	Frequency Domain
Highest Estimated Measur-able Fre-quency	3 THz	3 THz	25 GHz	25 GHz	120 GHz	200 GHz
Uncorrect-ed Electric Field Reso-lution (microns)	Limited by thickness of micro-wave sub-strate. ~100 microns	Limited by thickness of probe and probe dielectric constant ~100-200 microns	Limited by electron beam spot size and electron repulsion (0.3 micron over con-ductors only)	Limited by laser spot size and electron repulsion (0.3 micron over con-ductors only)	Limited by length of tip and by interference of lever arm with circuit ~50-100 microns	Limited by size of antenna and thick-ness of sub-strate ~50-100 microns
Probe Invasive-ness	N/A	Moderately Invasive	N/A	N/A	Moderately Invasive	Moderately Invasive
Relative Cost to Implement	Very Expensive	Very Expensive	Very Expensive	Extremely Expensive	Moderately Expensive	Moderately Expensive
Bandwidth Rating	Excellent (Several Decades)	Excellent-(Several Decades)	Fair (Nar-rowband)	Fair (Nar-rowband)	Good (One Decade)	Good (One Decade)
Compatibil ity with Standard Techniques	Poor	Fair	Poor	Poor	Good	Good
Adaptabil-ity of Test-ing Tech-nique for MMIC's	Poor	Good	Good	Poor	Very Good	Very Good
Ease of Implement ation	Difficult	Difficult	Very Diffi-cult	Very Diffi-cult	Moderately Difficult	Moderately Difficult
Noise Rat-ing	Low-Noise	Low-Noise	Noisy	Noisy	Noisy	Low-Noise

TABLE 1. Comparison of present day electric field mapping techniques.

	Direct Electro-Optic Sampling	Indirect Electro-Optic Sampling	Electron Beam Sampling	Photo-Emission Sampling	Scanning Force Micro-scopy	Modulated Scattering
Microwave Circuit Compatibility	GaAs Circuits w/o lower ground plane	Any Microwave Circuit	Microwave circuit must be mounted in a vacuum chamber	Microwave circuit must be mounted in a vacuum chamber	Any Microwave Circuit	Any Microwave Circuit
Field Information : Magnitude and/or Phase	Magnitude and Phase	Magnitude and Phase	Magnitude Only	Magnitude Only	Magnitude Only	Magnitude and Phase
Measurable Electric Field Components	Tangential	Normal and Tangential	Normal	Normal	Normal	Normal and Tangential

CHAPTER II

MODULATED SCATTERING AND PROBE DESIGN

2.1 Description of Modulated Scattering Experiment

Figure 2.1 displays a simplified schematic of the RF section of the near-field modulated scattering detection experiment. The power from an RF source is first divided by a Wilkinson power divider. Part of the RF signal is sent as the local oscillator (LO) to a wideband quadrature mixer from point 5 to point 6 in Figure 2.1. The RF signal to the DUT passes first through an attenuator and through a wideband circulator before entering the DUT. A modulated scattering probe (dipole, monopole, loop, etc...) with a diode mounted or integrated with the electrically small antenna is placed in very close proximity to the DUT at a specific position. As the diode bias on the probe is modulated at a low frequency (many orders of magnitude lower than the RF) between forward and reverse bias, a small modulated RF signal is scattered toward all ports of the DUT. The amplitude of this scattered signal is proportional to the square of the electric field amplitude intercepted by the probe [27]. Because the amount of power scattered by the probe is very small (orders of magnitude less than the input power to the DUT), a quadrature homodyne mixer and a lock-in amplifier are used to detect this weakly modulated signal.

To detect the scattered signal at the input port, the reflected signal is diverted to a wideband homodyne quadrature mixer by a wideband circulator. The in-phase and quadrature voltages at the modulated frequency are then measured. Through the use of an

absorptive RF switch, both the scattered reflected and transmitted signal (magnitude and phase) can be detected by the same quadrature mixer. In the future, the transmitted signal from any number output ports can be monitored through the use of multiple absorptive RF switching networks. The scattering probes are mounted on a computer controlled submicron translational stage. By moving the probe over a region of interest in close proximity to the DUT, a complete two dimensional electric field intensity ($|E|^2$) image and phase image from the normal and tangential electric fields is collected and stored on the computer.

The general schematic for the electric field imaging system used for both the 500 MHz-2 GHz band and the 2 GHz-18 GHz band is displayed in figure 2.2. Both *RF Imager Instruments* are computer controlled with a Data Translation 2801 A/D-D/A Card. The frequency and the power of the sweep oscillator (HP 8350B with 83592A RF Plug-In) as well as the voltage readings of the lock-in amplifier are controlled via an IEEE 488 instrument bus. The Oriel X-Y translator is controlled via the RS-232 serial port.

The experiment is incapable at present of measuring the instantaneous electric fields around a microwave circuit. This would be possible by implementing a wide bandwidth amplifier directly onto each probe and by sending amplifier's output to a high frequency oscilloscope. By taking many waveforms over one cycle for each point of the circuit, the entire field magnitude and phase can be saved. The advantage of this type of active probing is that the electric field strength may be dependent on the RF path for a nonlinear DUT or the DUT may not be operating with a single frequency mode such as with an amplifier or a multiplier diode that is producing harmonics. Once the time domain waveform is collected, the S-parameters can be deconvolved. With this technique, a complex microwave circuit can be divided into its constituent elements and each element of

the circuit can be compared with the theoretical model. It is not clear if active probing can be used at high microwave frequencies since the small probe is nearly open-circuited ($R \sim \infty\ \Omega$) to the input of the amplifier, i.e., not a 50 Ω system. The RC time constant at the input of the amplifier may easily dominate the system near 1 GHz. If a 50 Ω probe is used to result in a wide bandwidth, severe loading will occur on the DUT and the probe will become very invasive to the circuit.

The coupling of the modulated scattering probe to the DUT can be studied using electrostatics. Because the diode bias is modulated at a low video frequency, the probe's impedance state is thus static over many RF cycles. The DUT area closest to the probe will couple strongly if there are electric fields of the same polarization as the probe antenna. The monopole probe interacts strongly with the electric fields normal to the DUT while the dipole probe interacts strongly with the electric fields parallel to the plane of the DUT. The input impedance of the DUT will also change slightly because the probe tip has two impedance states: shorted (forward biased: $R \sim 0\ \Omega$) or open (reversed biased: $R \sim \infty\ \Omega$). The probe should be designed so that its effect on the input impedance of the DUT is minimal. However, this is generally not a problem because the coupling of the probe to the DUT is very small. The invasiveness of the probes used will be discussed at the end of this chapter. As the impedance state of the probe tip changes from one impedance extreme to the other, the strength of the probe's coupling with the near-fields of the DUT will also change. The strength of the electric field intensity intercepted by the probe and the probes induced dipole/monopole moment determines the strength of the scattered near-field. Proximity of the dipole or monopole with the circuit and size of the dipole or monopole also determines the electric field resolution of the probe and the strength of the interaction.

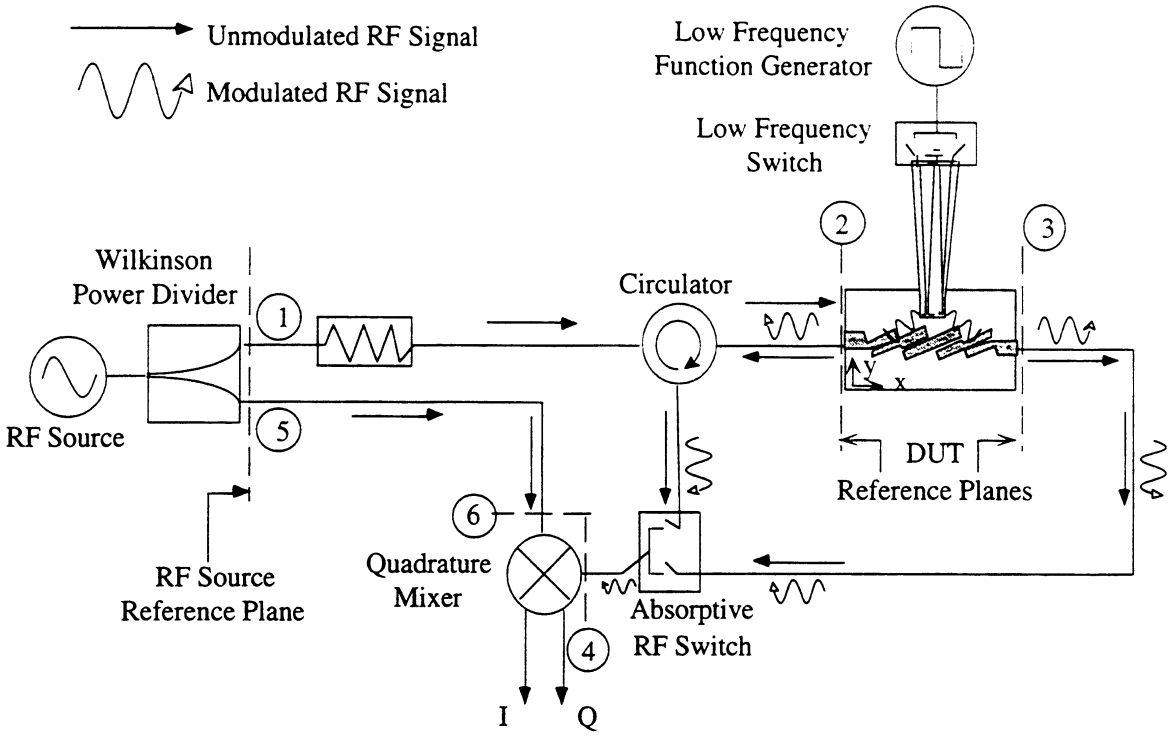

Figure 2.1: The microwave circuit electric field imaging experiment using the technique of modulated scattering.

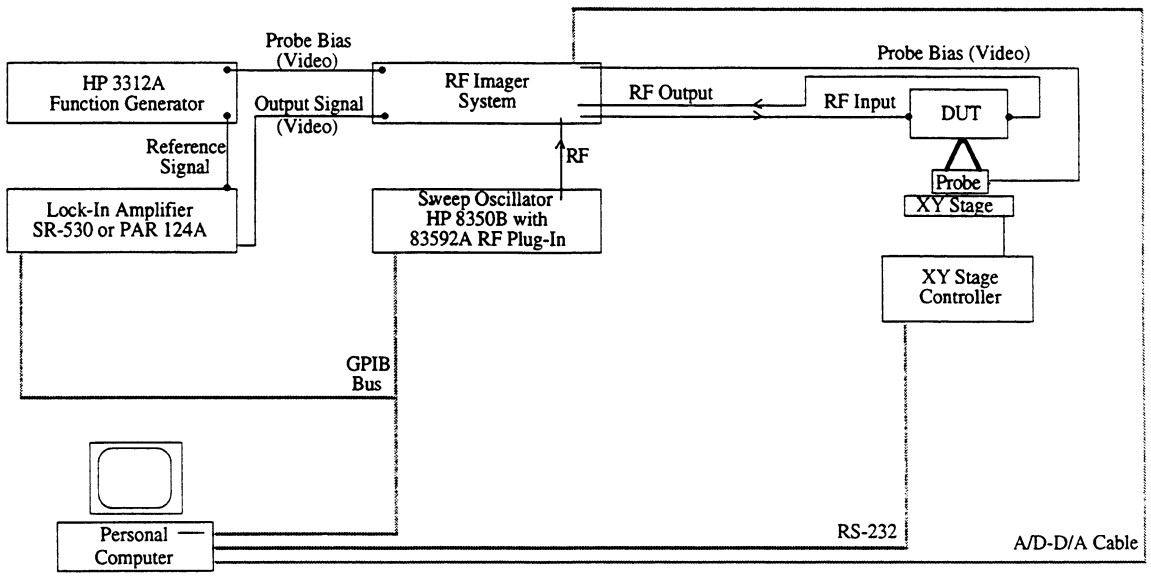

Figure 2.2: The microwave circuit electric field imaging system used in this experiment.

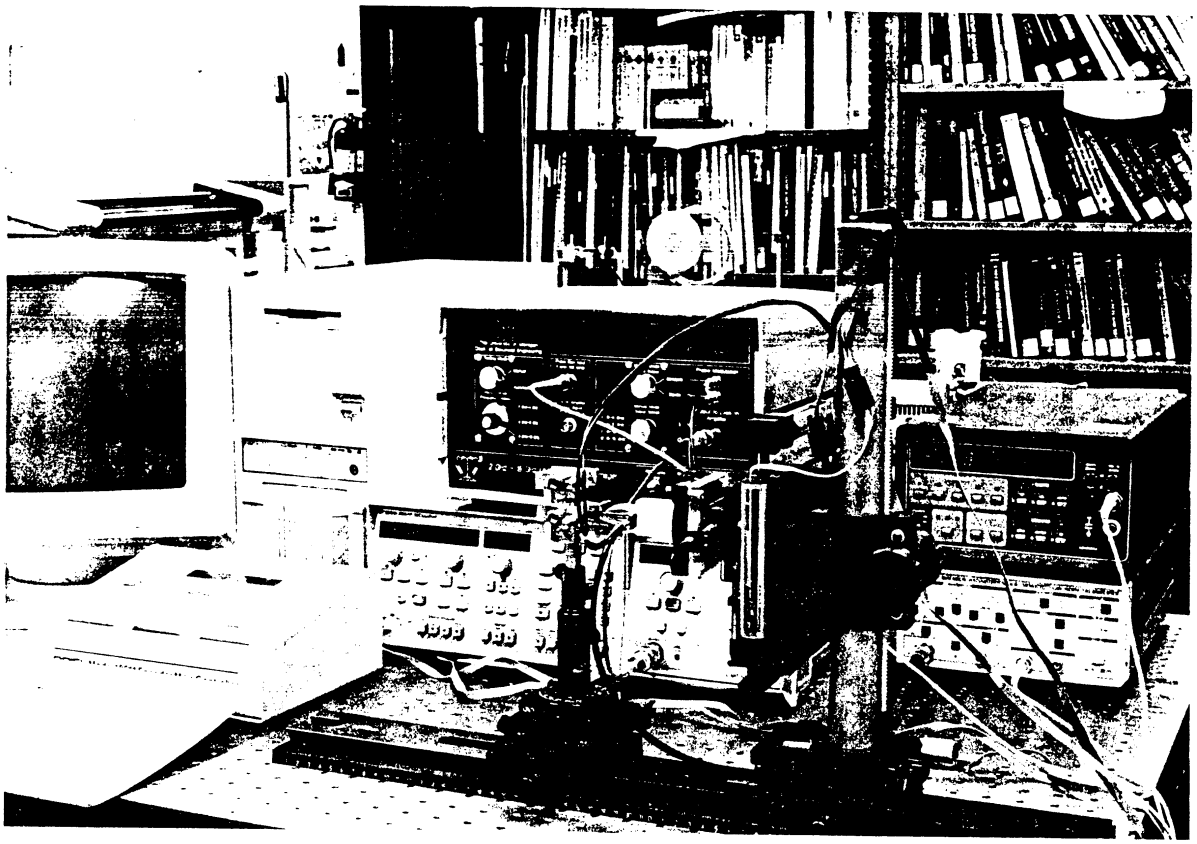

Figure 2.3: Electric field imaging experiment used in the frequency range of 2.0 GHz to 18 GHz. The entire system fits on a small laboratory bench. The probe and DUT are mounted on optical sliding rails in the foreground.

Figure 2.2 and figure 2.3 display the electric field imaging experiment used for this work. The entire system is controlled via a x386 personal computer with software written in Microsoft QuickC®. The system fits on an optical bench with optical rails and manual micrometers to align the probe with the microwave circuit. The alignment is accomplished by sequentially adjusting angle of the DUT with respect to the X-axis (horizontal axis) of the probe's movement until the probe's vertical position is within ±5 microns for each 10,000 microns of travel. First, the probe is positioned at one end of the circuit. Using a manual micrometer that positions the probe in the Z-direction (vertical) above the DUT, the probe is brought as close as possible without contacting the DUT. The vertical location of the probe above the DUT is recorded and the probe is backed away from the DUT. The probe is moved to the other end of the DUT and the vertical position of the probe is recorded. The probe is then backed off and the DUT is rotated to reduce the horizontal alignment error. The process is repeated until the horizontal alignment error is less than 10 microns for each 10,000 microns of travel. The DUT is mounted on an optical post and is assumed to be horizontally aligned along the Y-axis.

The positioning of the probe is accomplished by the use of an Oriel 16927 X-Y Translator with two Oriel 18240 Encoder Mike Drives and the Oriel 18011 Encoder Mike Controller. The range of travel of this system is limited to 1.0 inch (25.4 mm) and the positioning accuracy is better than 0.5 μm. The electric field maps are collected by moving the probe in an "*S*" shaped path over the DUT. The speed of acquisition is mostly limited by the speed at which the probe can be positioned over the DUT. The Oriel 18011 Encoder Mike Controller has the ability to move to a specific position with a single command, however, this method is extremely time consuming because the X-Y translator moves beyond the desired position and then approaches the specified position at a much slower speed. To reduce the movement time, the software that controls the X-Y translator

issues a command to move the probe at a constant velocity in a specific direction. A specific velocity is chosen depending on the stepping distance (the larger the stepping distance, the higher the velocity) and the desired positional accuracy. A command to move the stage in a specific direction at the chosen velocity is issued. The program monitors the position of the stage at the baud rate of the RS-232 port. When the stage reaches the desired position less a predetermined stopping distance, the stop command is issued and the probe coasts to a stop. When the stage has fully stopped, the true stopping distance is calculated and is used as the stopping distance for the next movement. The velocity and stopping distance are chosen experimentally so that the stage has a positioning error of less than 1 percent of the total stepping distance.

Figure 2.4 displays the actual 2-18 GHz RF Instrument used for this thesis. The instrument contains a power supply that drives the RF switches and digital computer controlled circuitry within the instrument. Due to time constraints, the 2-18 GHz instrument did not include the components necessary for measuring the electric fields from the transmitted port. Figure 2.5 displays the 500 MHz to 2.0 GHz instrument which contains the entire RF system to measure both the transmitted and reflected signals and has been completely integrated on a single printed circuit board with low cost components.

Figure 2.6 displays the conversion gain of each channel of the 2-18 GHz instrument for an RF signal at the DUT input port. This information is necessary to be able to compare the amplitude of the electric field response at one frequency with the electric field response at another frequency. The calibration factor for the electric field intensity is the conversion gain at a reference frequency divided by the conversion gain at the frequency of interest.

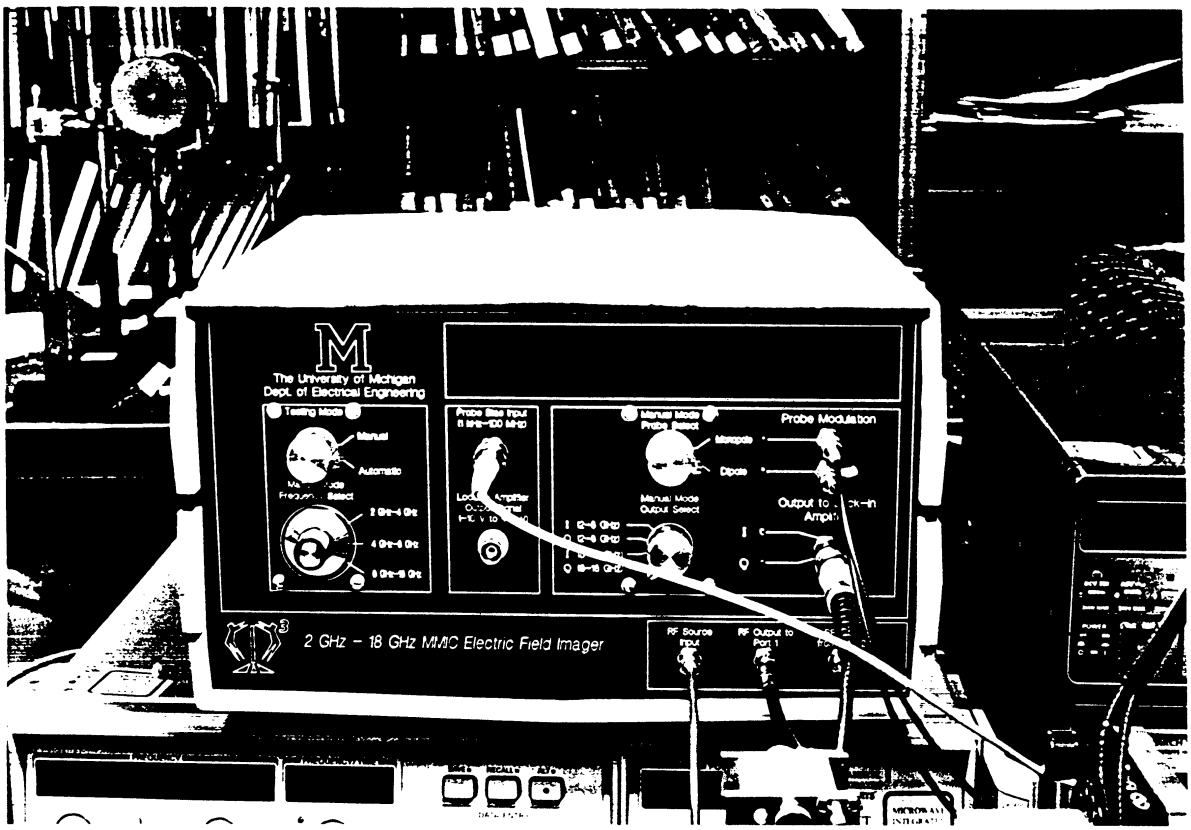

Figure 2.4: Electric field imager instrument that operates from 2 GHz to 18 GHz.

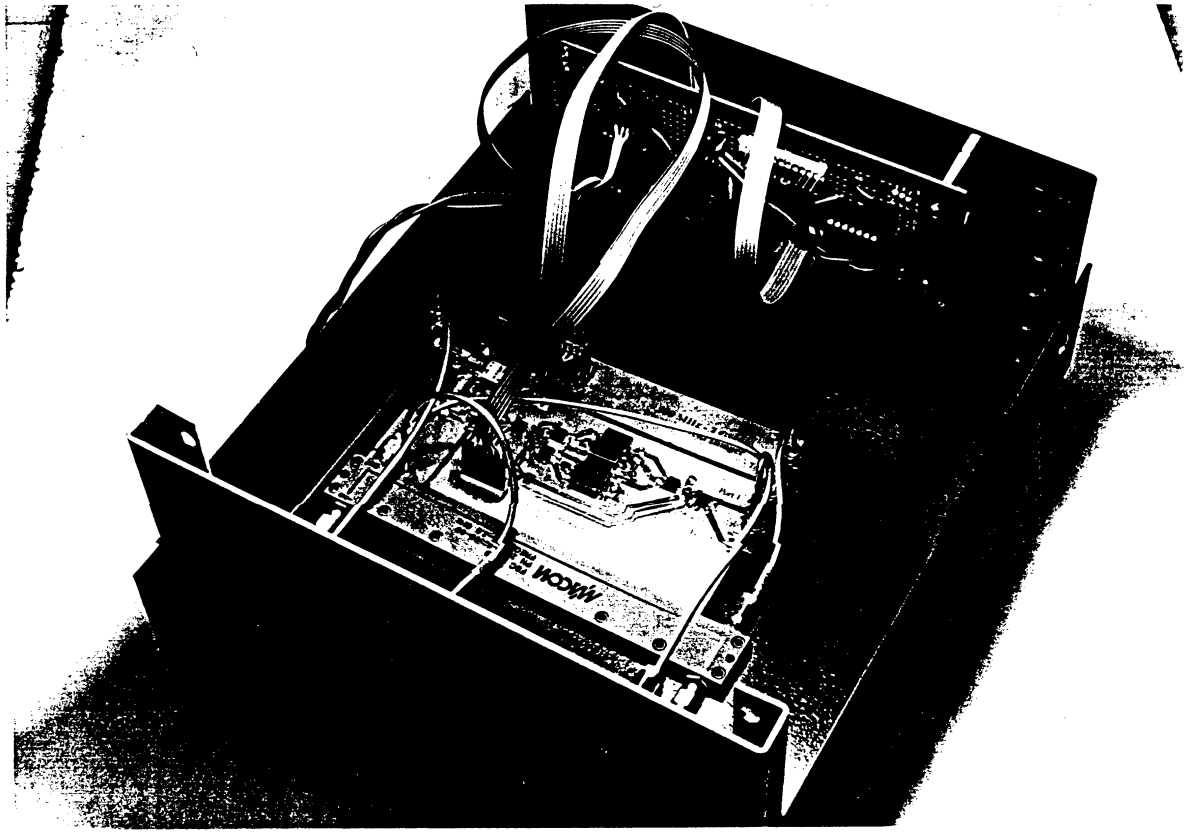

Figure 2.5: Two-port electric field imager instrument that operates from 500 MHz to 2.0 GHz

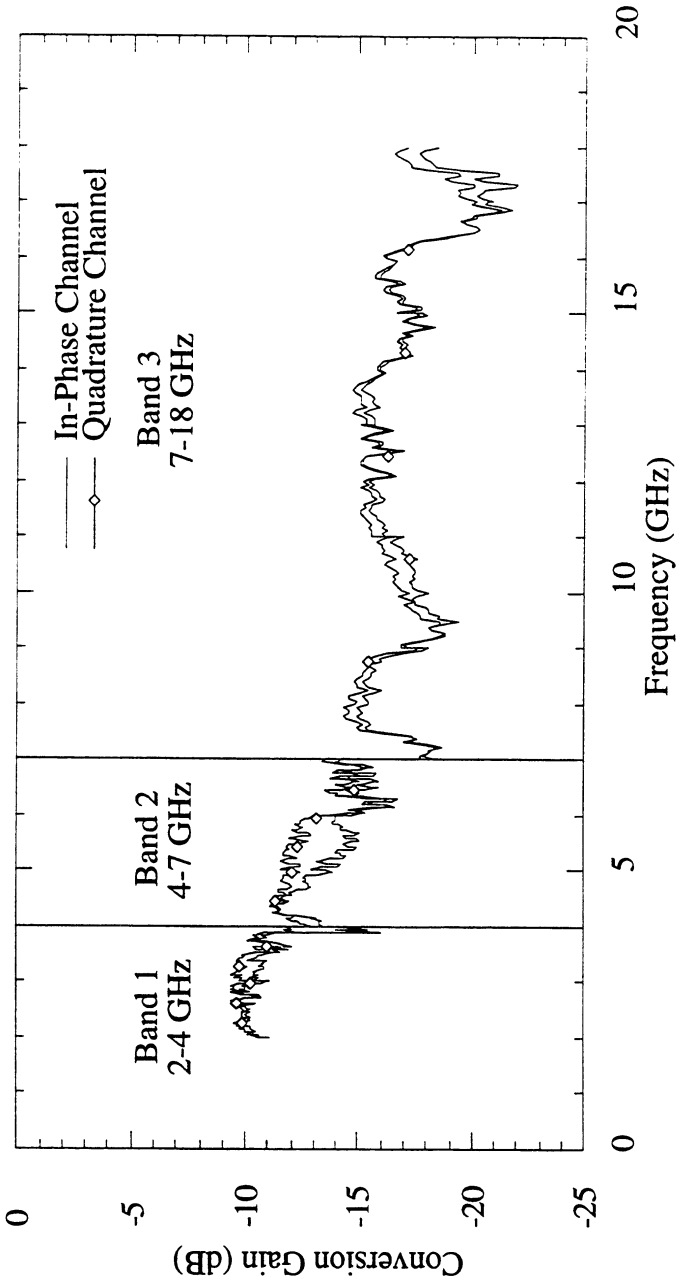

Figure 2.6: Conversion gain of the 2-18 GHz RF Instrument for a scattered reflected signal.

Another important consideration in building a modulated scattering system is the choice of which lock-in amplifier should be used. The following table summarizes the key issues in choosing which lock-in amplifier to use for detection of the magnitudes of the in-phase component and the quadrature component. Two types of lock-in amplifiers were used for this research. Initially, a Princeton Applied Research (PAR) 124A Lock-In Amplifier with a Model 190 Preamplifier was used. The PAR Lock-In Amplifier is excellent for measuring very low signal levels (1 μV) but the dynamic range for each voltage measurement is fixed to 20 dB dynamic range because the sensitivity cannot be computer controlled. Often while making measurements with the PAR Lock-In Amplifier over several different frequencies, the measured signal would be beyond the range and would saturate the lock-in amplifier. The other lock-in amplifier used for this research is a Stanford Research Systems (SRS) SR-530 Lock-In Amplifier with a Model SR-560 Preamplifier. This lock-in amplifier has less sensitivity to weak signals than the PAR lock-in amplifier, but the sensitivity of the instrument could be computer controlled and allowed greater dynamic range for the measurements. The SRS Lock-In Amplifier is used in the Magnitude-Phase mode when measuring the voltage levels from the in-phase and quadrature channels of the quadrature mixer. Because the RMS voltage levels measured are only positive, the measured phase only varies between 0° and 90° whereas with the PAR Lock-In Amplifier, the phase varies between -180° and 180°. The phase ambiguity is not significant while measuring the propagation constants of transmission lines; however, the ambiguity in the phase for differences of 180° or greater becomes significant when testing circuits such as 90° degree hybrid couplers where the phase varies rapidly over a short distance.

	PAR 124A Lock-In Amplifier w/ Model 190 Preamplifier (Gain=x10)	**SR 530 Lock-In Amplifier w/ Model SR-560 Preamlifier (Gain=x10)**
Computer Controlled Ranging	No	Yes
Measured Voltage Dynamic Range	20 dB	30 dB
Noise Figure for a 50 Ω input at 10 kHz	2 dB	8 dB
Maximum Signal Level for 10 dBm input to ckt.	5 mV	5 mV
Typical Noise Level	100 nV	1 μV
Phase Range	-180° to 180°	0° to 90°
Average # of Measure-ments per Point per Frequency	2	3.33

TABLE 2. Lock-In Amplifier Considerations

2.2 Quasi-Optical Modulated Scattering System

The modulated scattering system may also be employed in a quasi-optical system where the DUT contains a radiating element such as a log periodic antenna or a slot antenna. Instead of a waveguide magic-Tee junction as in figure 1.3, a semi-silvered beam splitter is used. A low-cost beam splitter for W-band can be made of low-loss mylar that is coated with metallic paint that is readily available from a hardware store. The reflectance of the beam splitter may be increased by spraying progressively more layers of metallic paint on the mylar sheet. As with the coaxial modulated scattering system, the quasi-optical modulated scattering system should be easy to implement for electromagnetic laboratories because only standard RF equipment is used with the system. The electric fields can be measured around the radiating elements as well as around the RF tuning circuitry and/or active devices employed by the DUT. The performance of the quasi-optical modulated scattering system is then limited by the operation of the quadrature mixer. For wideband operation at frequencies above 20 GHz, it may be necessary to mix the received modulated signal to a lower frequency (2 GHz to 6 GHz) with a single balanced mixer and then mix the IF one more time with a quadrature mixer.

2.3 Video Detector System

If phase is not important for an electric field measurement, then a probe with an integrated video detector would be able to measure the electric field intensity above the circuit if the RF signal into the DUT were modulated. The video detector probe would have the widest bandwidth and is fully compatible with the electric field imaging system described in this dissertation. Due to time constraints and the inherent simplicity of this method, this technique was not studied in this dissertation. The technique, however, does represent a very low cost solution for debugging problem microwave circuits and systems

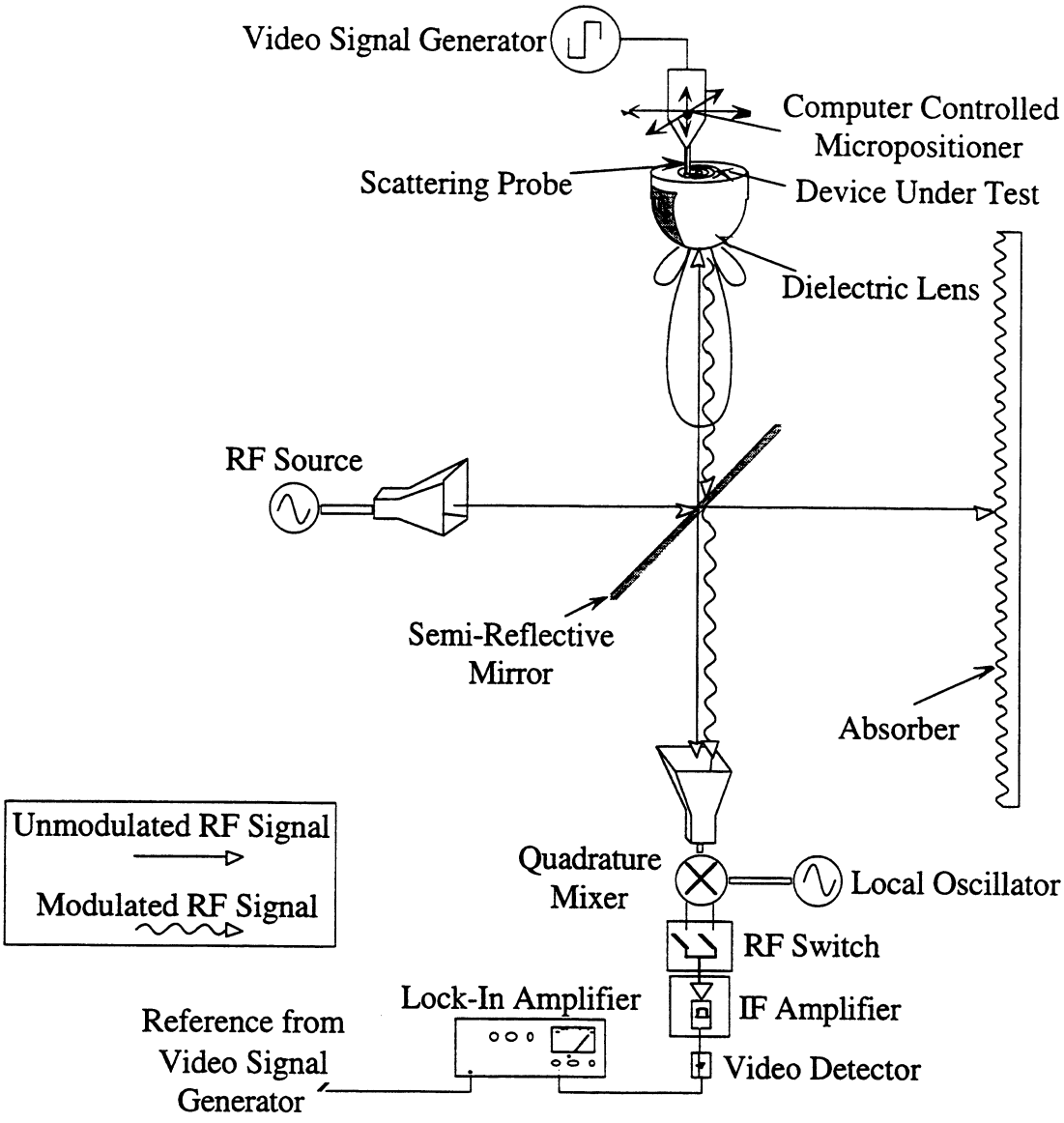

Figure 2.7: Quasi-optical modulated scattering experiment for radiating microwave circuits mounted on a dielectric hyperhemispherical lens.

where phase is not important for the measurements and where a dynamic range of less than 20 dB is sufficient for diagnostic purposes.

2.4 Hybrid Probe Design

The design of a probe is critical to the operation of any electric field mapping system. In this thesis, two types of probes are presented that were used to map the electric fields over microwave circuits: hybrid probes and integrated probes. This section describes the design of the hybrid probes. A good probe should be as small as possible on a very thin substrate. The dipole or monopole antenna should be electrically small (λ_o/ 100 - λ_o/1000) and as close to the end of the probe tip as possible. The use of an electrically short dipole provides a nearly flat transfer function over many decades of bandwidth [37]-[39]. Kanda found that the transfer function of a 15 cm long FET-loaded dipole was flat from 2 kHz to 400 MHz (within ±3 dB) [37]. Beyond 400 MHz, the dipole was driven into its first resonance. Using free-space dipoles with a length of 1.5 mm or less will extend the useful operating range up to 40 GHz. The diodes used for modulation up to 20 GHz should be low series resistance ($R_S < 15\ \Omega$), low junction capacitance diode ($C_j < 3.0$ pF) and the bias lines should be lossy so that they couple minimally to the DUT.

The radiation resistance of a short dipole is given by:

$$R = 20\pi^2 \left(\frac{L}{\lambda}\right)^2 \tag{2.1}$$

where L is the total dipole length and λ is the operating wavelength. For example, for a 150 μm long dipole in free-space, the radiation resistance at 2 GHz is $2.0 \times 10^{-4}\ \Omega$ and at 20 GHz the radiation resistance is $2.0 \times 10^{-2}\ \Omega$. Thus, a very small dipole will couple poorly to any circuit and will not load the circuit. The radiation resistance of a monopole

over a ground plane is half of the radiation resistance of a dipole of the same length. Similarly, a low capacitance (less than 2 pF), low resistance (less than 15 Ω) modulating diode will also couple poorly to a microwave circuit.

The capacitive component of the self impedance of a very short dipole of length L and of width w is given by [38]:

$$C = \frac{\pi \varepsilon_0 \varepsilon_{eff} \left(\frac{L}{2}\right)}{\left(ln\left(\frac{2L}{w}\right) - 1\right)} \tag{2.2}$$

This approximation for a strip dipole of width w is equivalent to a cylindrical dipole of radius a where $a=w/4$ [40]. For a dipole of length 150 μm and of width 15 μm, the capacitance from equation 2.2 gives (1.0 fF)*ε_{eff}. If the substrate is thinned to a thickness that is less than $\lambda_d/20$, the effective dielectric constant will be less than the average of the relative dielectric constant of the substrate and of free space: (1+εr)/2. The low resistance and high capacitance of a short dipole gives a very flat frequency response until the dipole approaches its first resonance at half a wavelength (2 THz for a 150 μm long dipole in free space).

Figure 2.8 displays the design of the hybrid probes used initially for electric field mapping. A dipole and a monopole of approximately 250 μm long (1/100th of the smallest operating RF wavelength of the microwave circuit under test) are used as modulating scatterers. The probes are fabricated on 125 μm thick low loss quartz substrate (Dynasil 4000 from Accumet) and are fabricated using standard photolithographic techniques with 1.0 μm thick gold and a thin underlying layer of chrome to promote gold adhesion. In the hybrid probes, beam lead Metelics Corporation low barrier Schottky diodes (component #MSS30-154 B10 and B20) are used and the diode bias current is modulated between

0 mA and 1 mA. These diodes feature a low series resistance (Rs ~ 3 Ω) and a low junction capacitance (Cjo ~ 0.22 pF). The commercially available low-cost diode is placed between the arms for the dipole probe and two diodes are placed between the CPW ground planes and the CPW center conductor for the monopole probe. High resistance chrome lines (200 Ω/square) absorb any RF signal that travels beyond the modulating diode, provide lines for biasing the diode and also serve as current limiters (Rs ~ 1 KΩ). The electrically small but physically large (250 μm by 250 μm) commercially available diode is placed as close as possible to the probe antenna. We expect that these diodes with this type of probe structure can be used up to 40-60 GHz without encountering any problems with diode parasitics. A more limiting factor for high frequency operation is the size of the scattering antenna and the manual placement of the hybrid diodes on the probe tip. In a commercial environment, manual placement of diodes on the probe tips is very time consuming, expensive and unreliable in large quantities. For these reasons we proceeded to develop monolithically integrated probes with integrated antennas, diodes and bias lines.

2.5 Monolithic Integrated Probe Fabrication

Integrated probes were fabricated on a high resistivity silicon substrate using a monolithically integrated Schottky diode as the modulating element. The following process was modeled on SUPREME which is a two dimensional silicon process simulator. The dopant dose and energy were chosen to have a highly doped Schottky diode (n^+ = $2x10^{17}/cm^3$) and the ohmic contact dose was chosen to have a high shallow doping concentration of $10^{20}/cm^3$. To simplify processing, aluminum was used as the Schottky metal as well as the ohmic metal. The ohmic contact relies upon tunneling as the transport mechanism. The current-voltage curves of these diodes is presented in section 2.6.

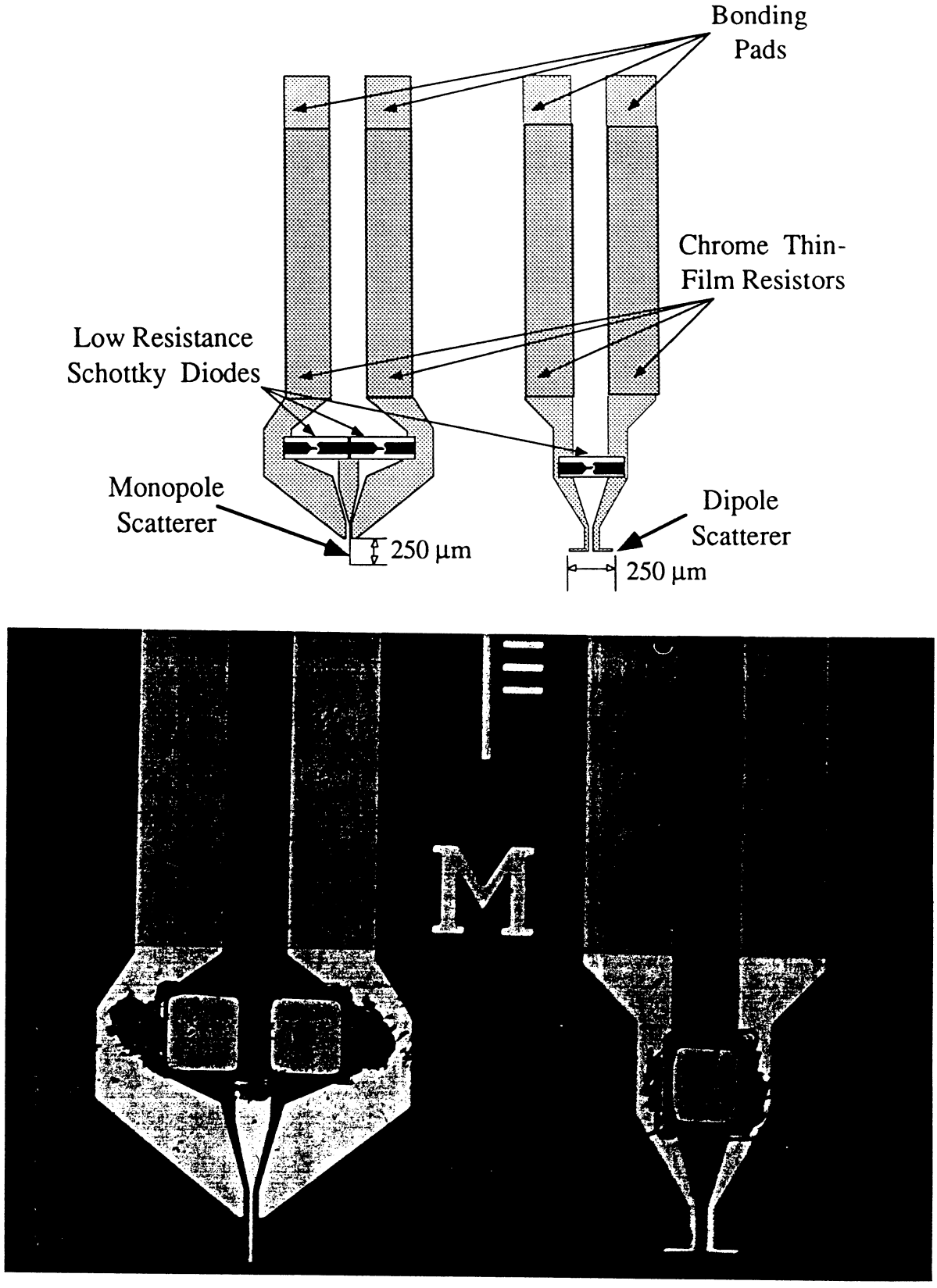

Figure 2.8: The hybrid near field scattering probes. The dipole probe is used for scattering the tangential electric field, and the monopole probe is used for scattering the electric field normal to the DUT (note: drawing is to scale).

Figure 2.9 a)-k) displays the fabrication procedure for making silicon Schottky diodes. First, a 0.63 μm layer of oxide is thermally grown on the silicon wafers using a dry-wet-dry oxide process at 1050°C for 10-90-10 minutes (a). Next, the n-doped regions are patterned and the masking oxide is etched in buffered hydroflouric acid (BHF) (b). The wafer (still covered with a patterned 1 μm layer of photoresist) is then ion implanted with phosphorus with a dose of $1.2x10^{14}/cm^2$ at 60 KeV. The photoresist is removed by a 15 minute oxygen plasma etch at 100 Watts and the wafer implantation is driven-in at a temperature of 1100°C for 100 minutes (c). After drive-in, the ohmic contact regions are patterned with a 2 μm thick layer of photoresist (d). Again, the wafer is ion implanted with phosphorus with a dose of $7.0x10^{15}/cm^2$ at 60 KeV. Next, the photoresist is removed with an oxygen plasma etch and the wafers are thermally annealed at a temperature of 950°C for 30 minutes (e). The metal layer is patterned with AZ 5214E photoresist in image-reversal mode and a 5,000 Å-thick layer of aluminum with a 2% silicon content is sputtered onto the wafer. A thicker layer of metal is necessary to have the probes thicker than one skin depth, but the sputtering machine used allows at most 5000 Å of metal to be sputtered at one time. The ohmic contacts are then rapidly annealed at 570°C for 120 seconds in an argon atmosphere. A final metal layer is patterned with AZ 5214E photoresist and a 10,000 Å-thick layer of aluminum is thermally evaporated onto the wafer. The Schottky contact area is approximately 10 μm by 25 μm and the distance between the anode and cathode is 15 μm.

For the ideal probe, the dipole or monopole should be mounted on a wafer that is much thinner than the smallest antenna fabricated. Figure 2.10 displays the step by step process for chemical thinning of the four inch diameter (500 μm thick) wafer. After the diodes are fabricated, a 50 μm-deep groove is cut with a dicing saw between each die to help determine when the chemical thinning process should be stopped (a). Next, the wafer

is mounted (patterned side down) on a metal carrier with clear wax (b). The wafer is chemically etched from back in a solution of HF-Nitric Acid-Acetic Acid with a concentration of (50 ml:500 ml:5 ml). The wafer is etched for 45 minutes until the grooves appear and is then etched sligthly longer until the wafer is estimated to be 40 μm thick (c). The wafer is rinsed and removed from the acid solution. The wafer holder is heated until the wax is melted. The die are lifted from the melted wax and placed in a solution of TCE to dissolve the wax from the die (d). The probes are diced, mounted and wire-bonded to a probe carrier that is presented later.

Figure 2.11 displays the layout of the integrated probes. The dipole probes are fabricated with antenna arms that are of various lengths (L = 150 μm, 250 μm and 350 μm long). The monopole probes are fabricated with arms of 50 μm, 100 μm, 200 μm and 400 μm long. Individual probes have an overall length of 5 mm and a width of 0.5 mm and paired probes have an overall length of 5 mm and a width of 0.9 mm. Figure 2.12 displays the completed integrated probes with a 150 μm long dipole in a) and a 100 μm long monopole in b). The feeding transmission lines are chosen to have a characteristic impedance of 120 Ω by using the design equations from Waddell [43] which are presented in Appendix B.

Figure 2.13 displays a completed integrated probe and holder. The probe is mounted on an anisotropically etched low resistivity silicon wafer probe holder. A rectangular groove is anisotropically etched on the holder wafer in a solution of potassium hydroxide (KOH) and water in a ratio of 300 gm to 600 ml at 60 C until an etched depth of 80 μm is reached. Gold bias lines are then patterned on the etched wafer before dicing the probe holders. To mount a probe, 5-15 sec. INSTA-CURE™ cyanoacrylate glue is placed

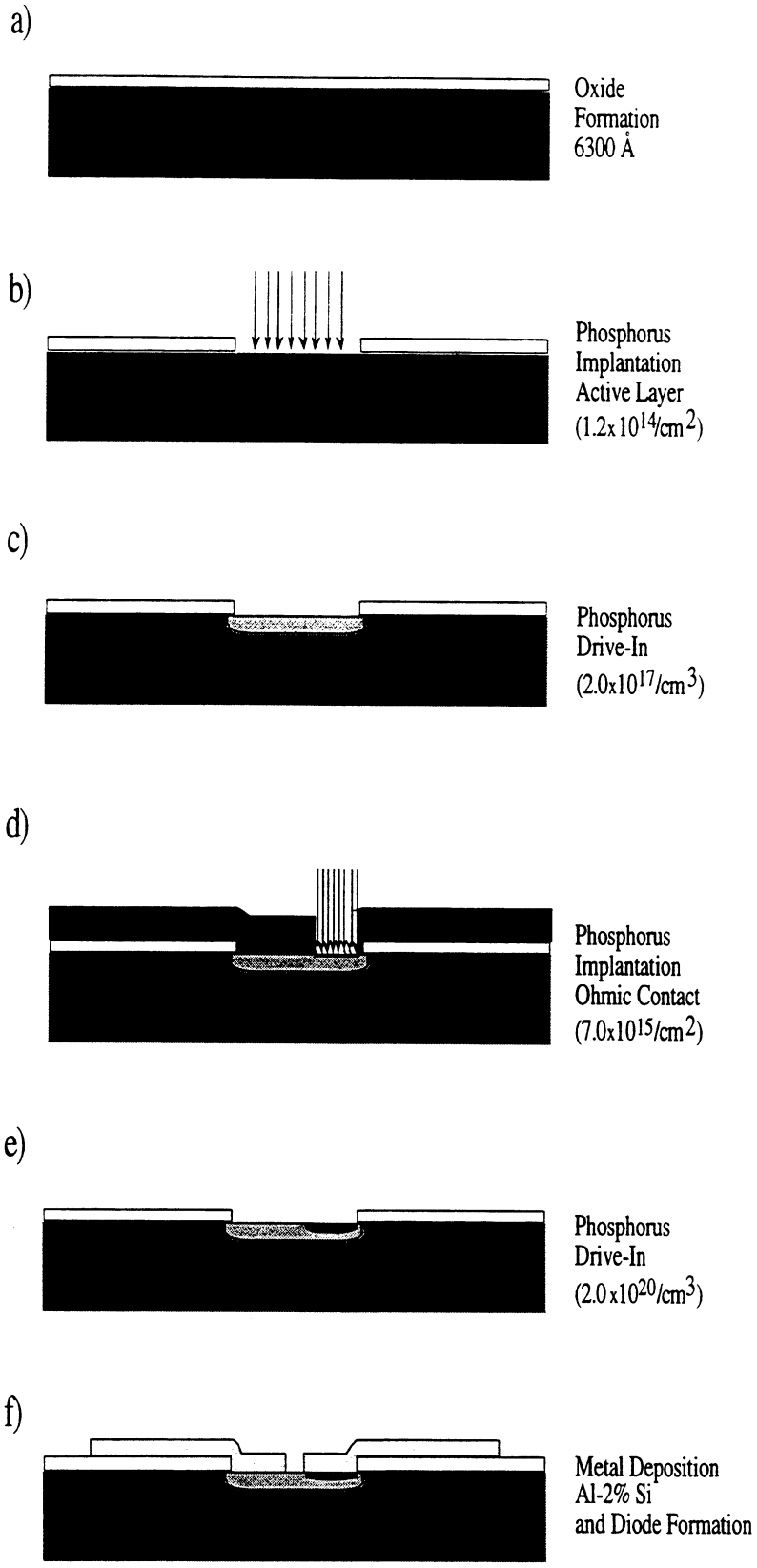

Figure 2.9: Step by step fabrication procedure used for making integrated Schottky diode probes.

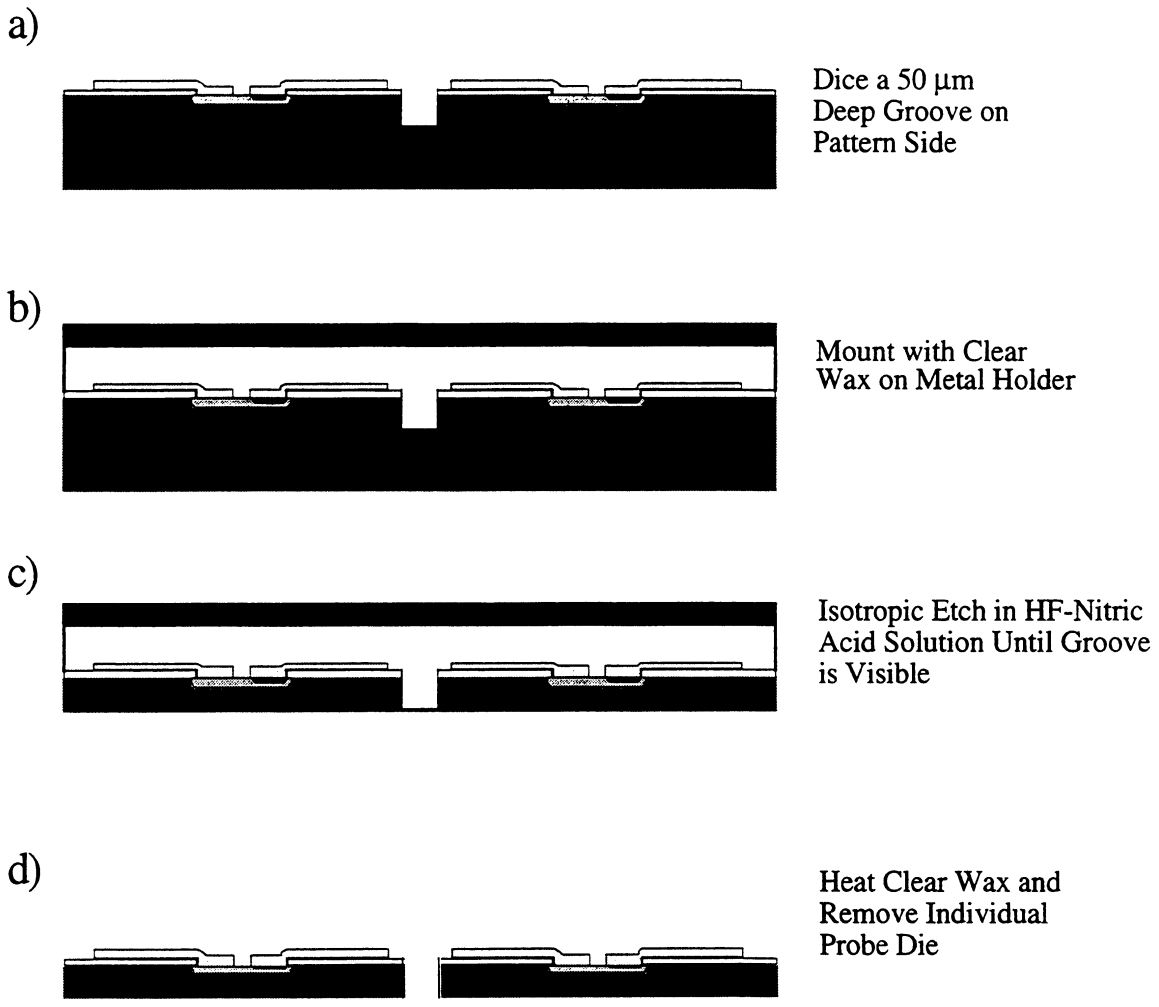

Figure 2.10: Step by step chemical thinning process used with integrated probes.

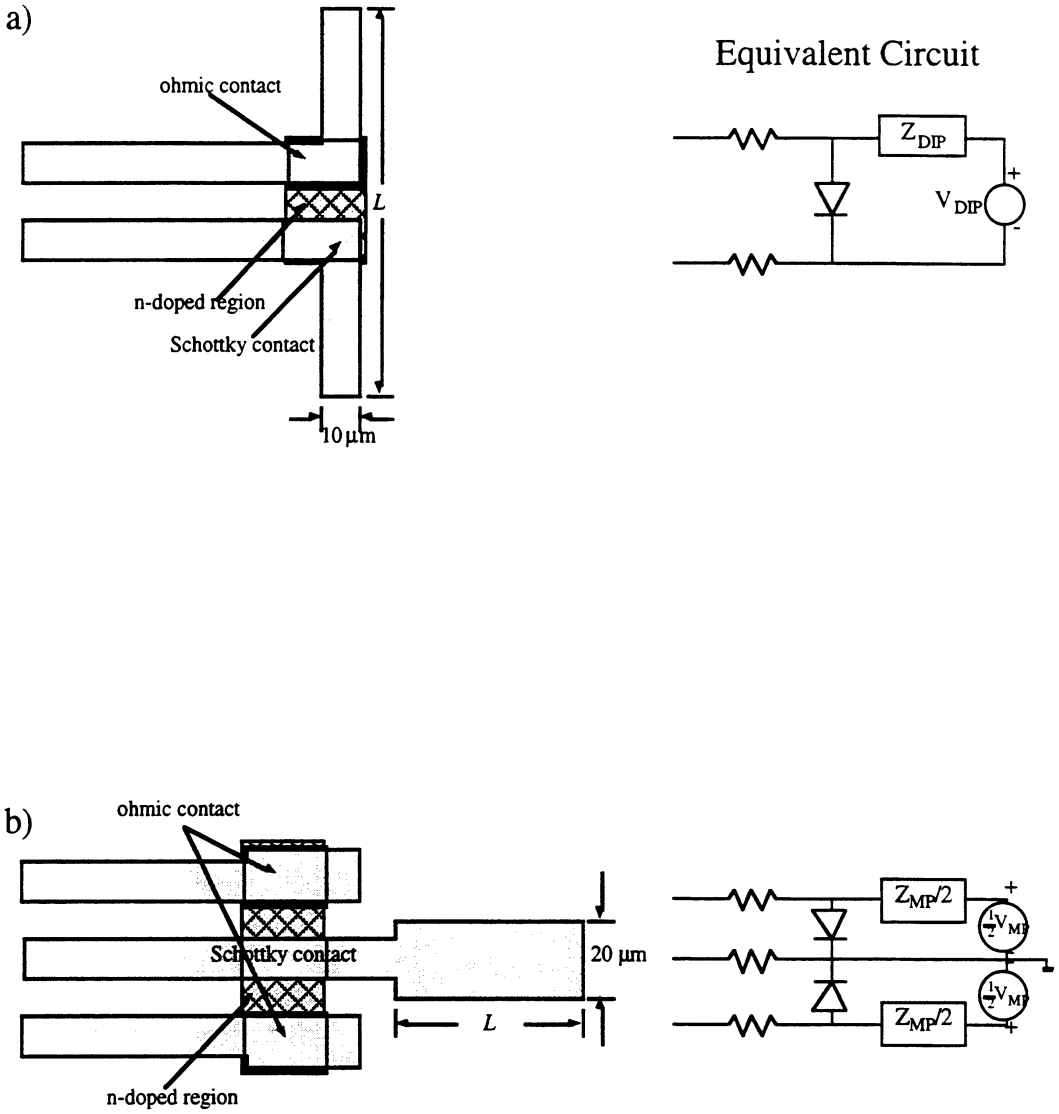

Figure 2.11: a) Integrated dipole probe and b) integrated monopole probe that are fabricated on high resistivity silicon.

a)

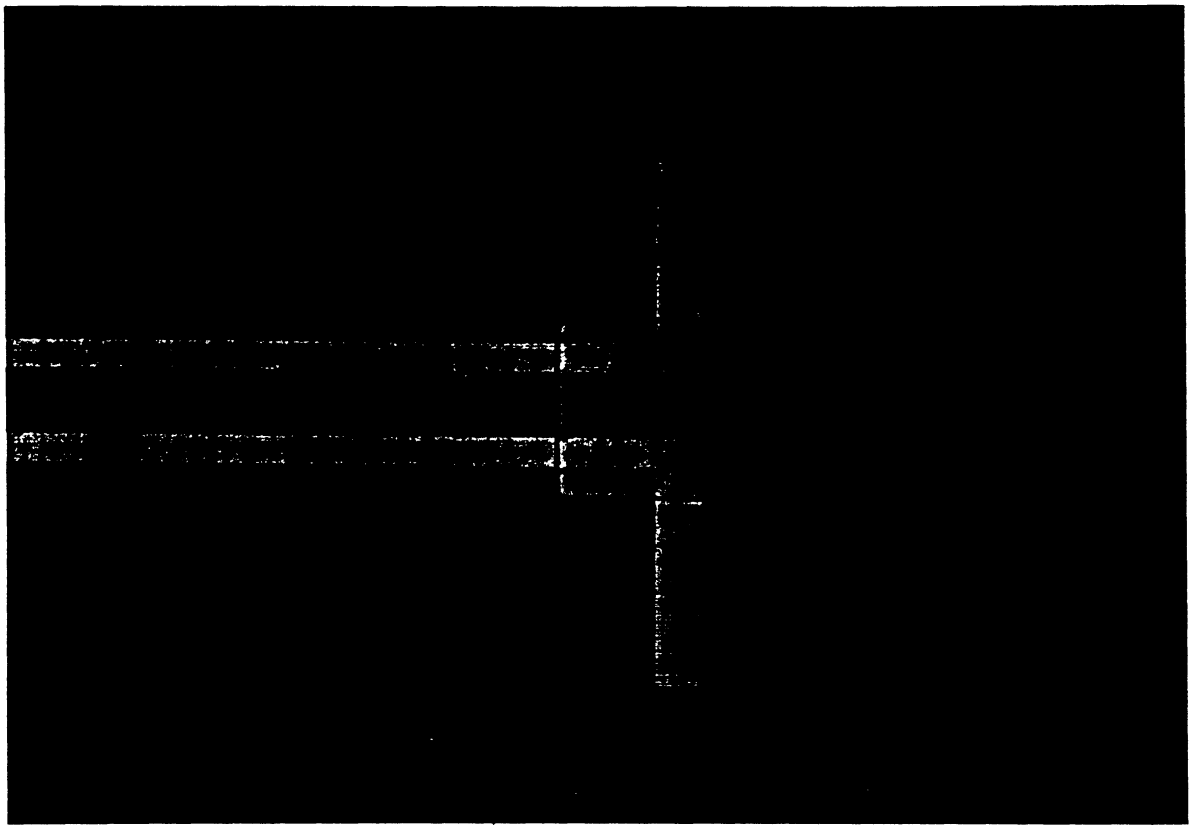

b)

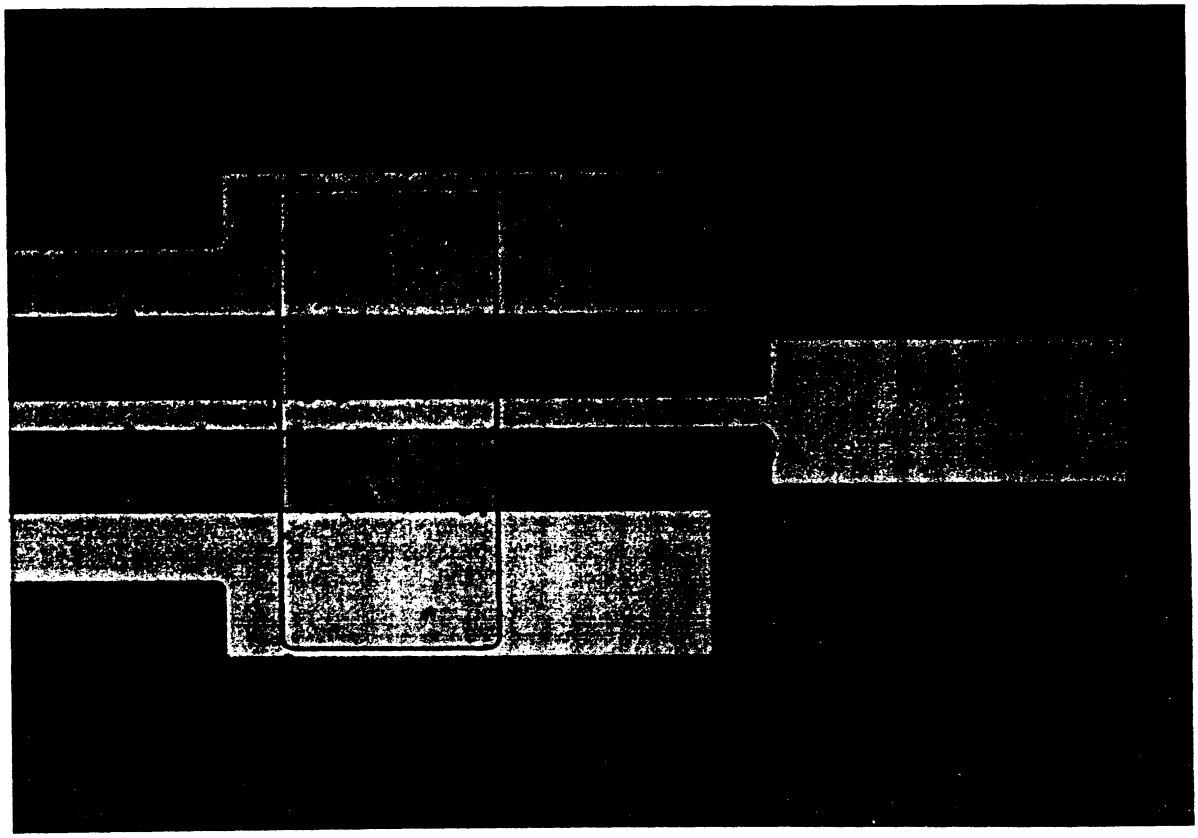

Figure 2.12: Photograph of an integrated probe with a) a 150 μm long dipole and b) a 100 μm long monopole.

in the etched groove and the probe is placed inside the groove. The groove aids in alignment of the probe and prevents the probe from moving as the thin film of glue spreads between the probe holder and the probe tip. The probes are then wire bonded with 0.7 mil wide gold ribbon and the ribbons are silver epoxied at the contacts to insure a strong bond. After good electrical contact between the probe holder bias lines and the probe tip is achieved, a low frequency connector is mechanically glued and then silver epoxied to the probe holder. After baking, the probe is mechanically glued to an acrylic holder with mounting screw holes so that it may be attached to the micropositioner. The entire mounting procedure takes four hours for each probe in a research oriented laboratory.

2.6 Monolithically Integrated Diode Characteristics

The Schottky diodes are designed to be low resistance, low capacitance diodes that are able to pass up to 10 mA under forward bias. The geometry of the diode is chosen to fit the 10 μm wide bias lines for both the monopole and the dipole. Because the silicon Schottky diodes need only to work up to 20 GHz, only one type of diode is fabricated and used for the integrated probes. Figure 2.13 displays the current versus voltage (I-V) characteristics of the diode used with the dipole while figure 2.14 displays the I-V characteristic of the diode used with the monopole. Both diodes turn on at approximately 0.5 V. The series resistance of a single diode is measured to be 12 Ω. The combination of the junction and parasitic capacitance of the dipole diode is measured to be 2.0 pF which gives a cutoff frequency around 40 GHz.

The bias lines are designed to be resistive so that any RF power that travels along the transmission lines will be attenuated. This attenuation will strongly reduce any RF electromagnetic coupling of the long bias lines with the DUT. The resistance of a single bias line is 35 Ω±5 Ω. Because the diode need only act as an RF switch, no further study

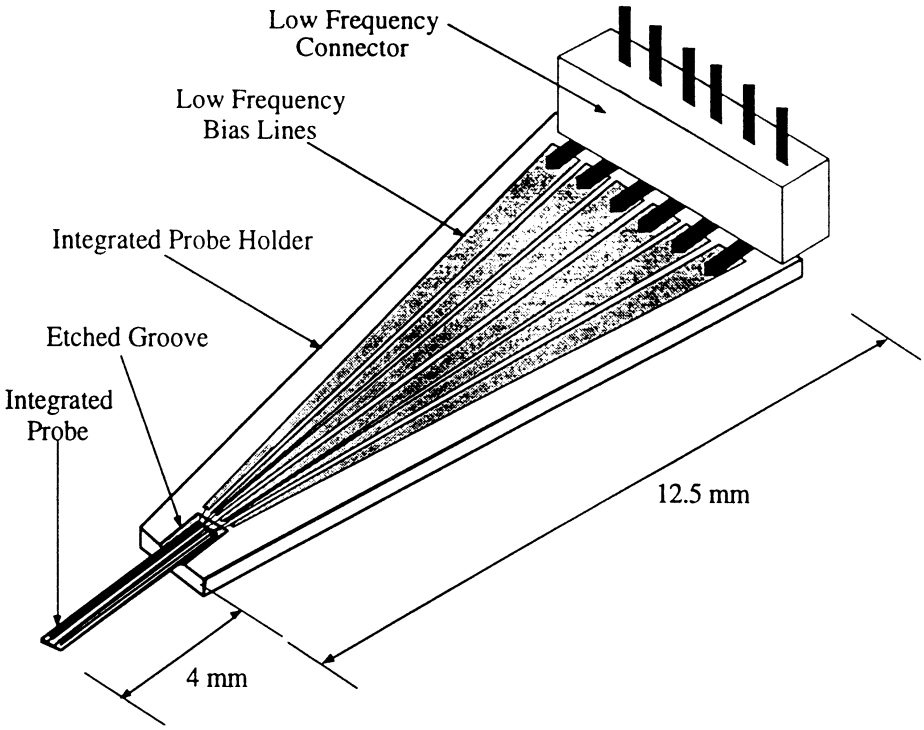

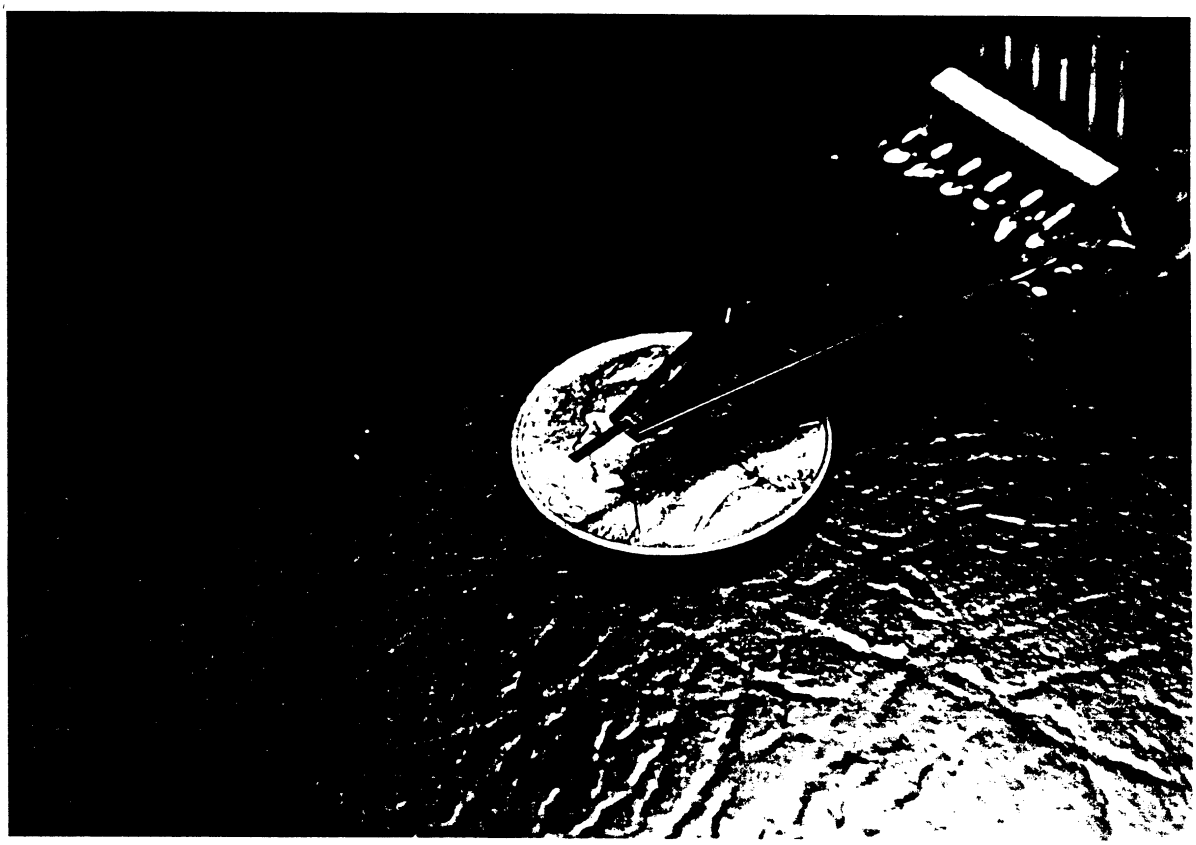

Figure 2.13: Integrated probe on 40 μm thick silicon mounted on a low resistivity 500 μm thick silicon wafer with silver epoxied low frequency connector on right.

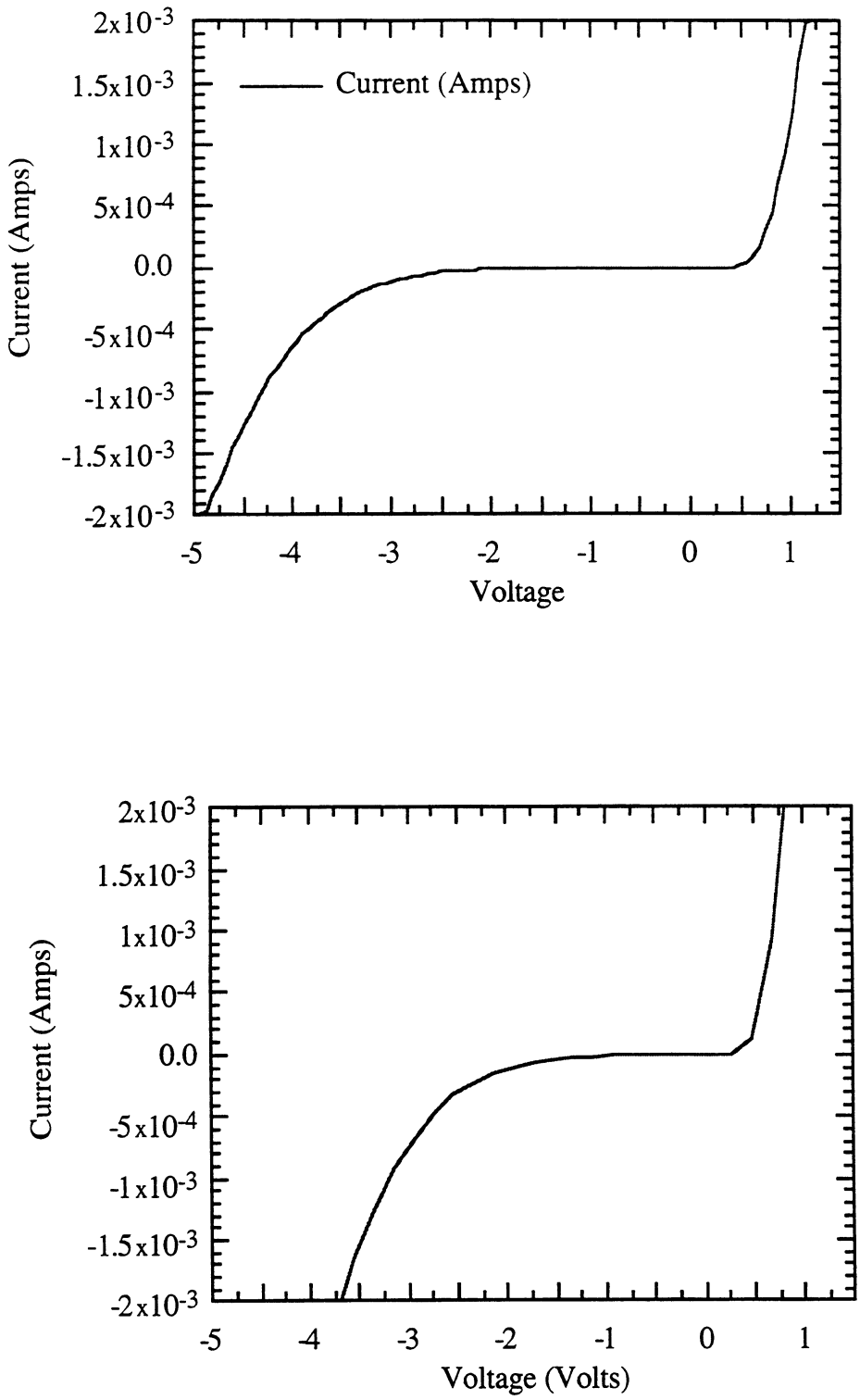

Figure 2.14: Current versus voltage curve of the dipole (top) and monopole (bottom) diode.

of the characteristics of the diode was performed. Due to the high doping of the diodes, the reverse breakdown voltage is fairly low (~ -3 Volts). This does not present a problem since the diode will be biased between -1 V and +1.25 V and will not intercept electric fields strong enough to force operation in reverse breakdown mode.

2.7 Probe Invasiveness

A simple test of a probe's invasive nature is to test the probe with a circuit that is known to have very strong electric field components above the circuit such as a low dielectric constant microstrip transmission line. To measure the invasiveness of the integrated probe, a 50 Ω microstrip line on ε_r=2.2 RT/Duroid (h=380 μm) is connected to a network analyzer. The reflection coefficient is measured from the transmission line alone and with worst case of the probe in contact with the transmission line. Figure 2.15 displays the reflection coefficient (S_{11}) of the microstrip line with and without three different types of probes in contact with the microstrip: an integrated probe on 40 μm thick silicon, a hybrid probe on 125 μm thick quartz, and an electro-optic probe on 500 μm thick $LiTaO_3$. Notice in figure 2.15 how there is little to no change in the operating point of the microstrip and that all of the deep nulls in the reflection coefficient remain in the same position even when the probe is present.

Typically, a probe's perturbation on the reflection coefficient is a maximum when the reflection coefficient of the circuit is a minimum. When the reflection coefficient of the circuit is between -35 dB and -12 dB, all probes change the reflection coefficient by at most 3 dB. The ratio becomes exaggerated when the reflection coefficient becomes less than -40 dB. Because this invasiveness test is very close to the worst possible case (air as the dielectric and the probe in contact with circuit), perturbations of circuits with higher dielectric constants and with the probes at greater distances can only reduce the invasive-

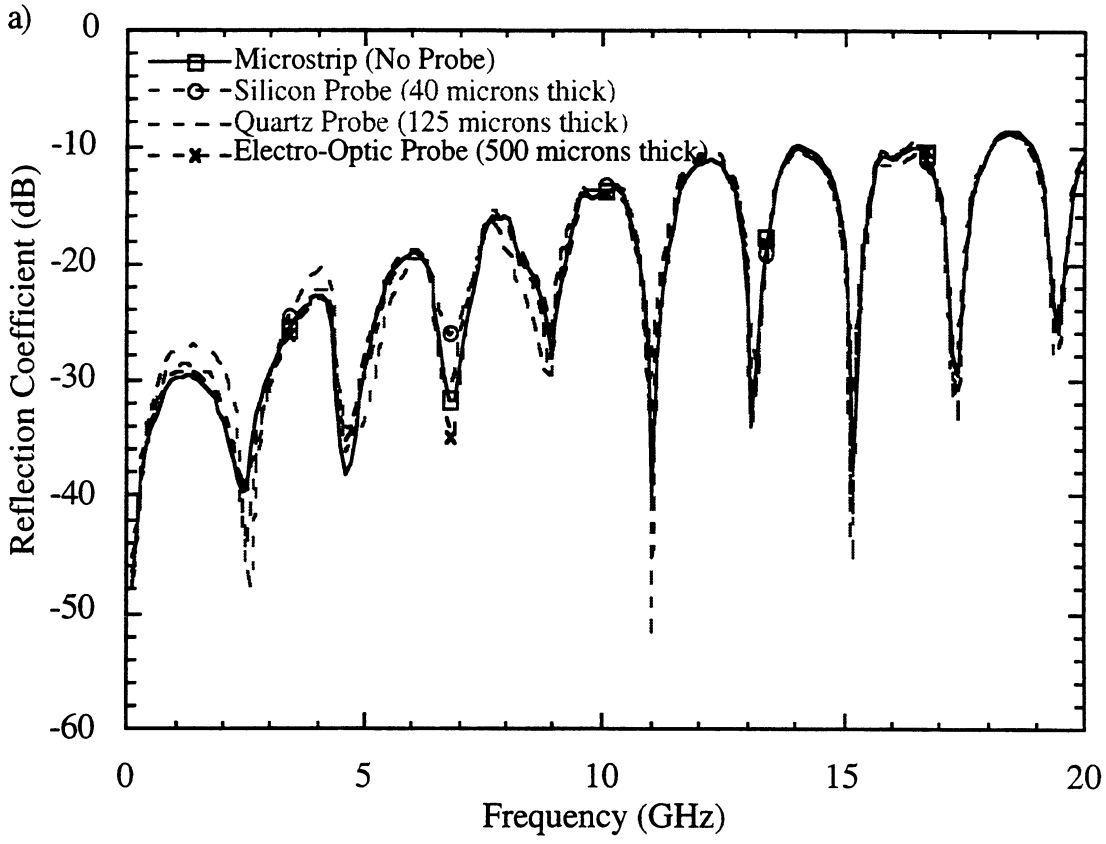

Figure 2.15: Reflection coefficient of a 50 Ω microstrip line on ε_r=2.2 RT/Duroid in the presence of three different types of probes in direct contact with the line.

ness because more of the fields will be contained within the dielectric.

2.8 Probe Resolution

The expected spatial electric field resolution of the probes is not studied in great detail in this dissertation. The expected resolution of a dipole of length, $L < \lambda/10$, is slightly less than the physical length of the dipole because the current distribution on this dipole is believed to vary in a triangular fashion [41]. However, as the length of the dipole decreases, other bulk effects due to the finite size of the diode, biasing lines and substrate thickness need to be taken into account. Also, the amount of power that will be scattered from the dipole will decay as the square of the length of the dipole and the finest resolution will ultimately be noise limited. The spatial electric field resolution of the monopole is also expected to be slightly less than the size of the monopole for similar reasons.

2.9 Conclusions

In this chapter, the modulated scattering experiment used in this thesis is described. The automated hardware is described as well as the RF system used in this work. Two types of probes, hybrid and integrated, are presented and characterized. The monolithic probes are the best type of probe to use for high electric field resolution near planar microwave circuits because physical size of the diode is greatly reduced compared with commercially available hybrid diodes. The fabrication procedure of the integrated probes is presented as well as the DC characteristics of the fabricated silicon Schottky diodes. The diodes have a cutoff frequency around 40 GHz and should work well as RF switches up to 20 GHz. Finally, the invasiveness of several types of probes are studied. The scattering parameter results are presented for three probes (integrated probe on 40 μm thick silicon, hybrid probe on 125 μm thick quartz and a 500 μm thick $LiTaO_3$ electro-

optic probe) in contact with a 50 Ω microstrip transmission line on a low dielectric constant substrate (ε_r=2.2). The results show that the probes do not change the scattering parameters of the 50 Ω microstrip line on a low dielectric constant substrate and are therefore noninvasive.

CHAPTER III

THEORY OF OPERATION

3.1 Introduction

The modulated scattering theory applied to a pyramidal horn antenna with a small scattering dipole is well known and was developed in 1955 by Cullen and Parr [27]. Figure 3.1 displays the experiment. Let A be defined as a forward travelling voltage wave and B as a backward travelling voltage wave at a reference point within the waveguide. The electric field at the position of the small dipole antenna will be directly proportional to the forward travelling wave complex amplitude, A, and a *normalized* electric field distribution, $\boldsymbol{F}(x, y, z)$. $\boldsymbol{F}(x, y, z)$ is unitless and does not depend on the input power into the system. This electric field at the dipole position, (x, y, z), is given by [27]:

$$\boldsymbol{E}(x, y, z) = A\boldsymbol{F}(x, y, z) \tag{3.1}$$

By using the reciprocity theorem, the backward travelling wave within the waveguide is derived to be [27]:

$$B = \left(j\omega\frac{Z_o}{ab}\right)\boldsymbol{M} \bullet \boldsymbol{F}(x, y, z) \tag{3.2}$$

where Z_o is the characteristic impedance of the waveguide, a and b are the waveguide dimensions, ω is the operating frequency and $\boldsymbol{M}$ is the dipole moment produced by the action of the electric field $\boldsymbol{E}(x, y, z)$ on a linearly polarizable thin dipole according to the equation [27]:

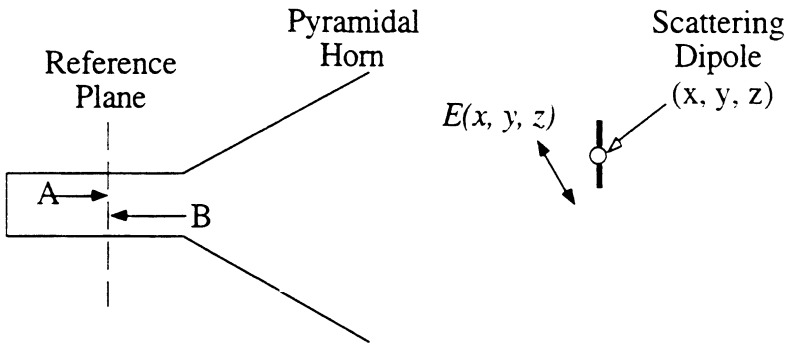

Figure 3.1: Modulated scattering system for a pyramidal horn and a small dipole scatterer.

$$\boldsymbol{M} = A\alpha\,(\boldsymbol{u} \bullet \boldsymbol{F}\,(x, y, z))\,\boldsymbol{u} \tag{3.3}$$

where α is the polarizability of the dipole and $\boldsymbol{u}$ is the unit vector in the direction of the dipole. After substituting equation (3.3) and (3.1) into equation (3.2), the backward wave is given by:

$$B = A\left(\frac{j\omega\alpha Z_o}{ab}\right)(\boldsymbol{u} \bullet \boldsymbol{F}\,(x, y, z))^2 \tag{3.4}$$

From equation (3.4), the voltage of the backward travelling wave is proportional to the square of the normalized electric field at the location of the dipole. To quote [27], "This is the fundamental formula on which the method depends."

The same argument can be applied to any reciprocal scattering process regardless of the scattering path or multi-path effects as outlined for the case of two dipoles by Hygate and Nye [33]. The scattered voltage that is detected by a linear detector is:

$$B = kE^2 \tag{3.5}$$

In this dissertation, the square of the electric field ($|E|^2$) is referred to as the electric field intensity.

As a scattering probe moves near a microwave circuit, the probe will couple to an area of the circuit directly below its location. An electric field will be scattered into the DUT that is proportional to the electric field strength around the probe induced by the DUT and the probe's coupling efficiency to the DUT. The probe's coupling efficiency is proportional to the dipole moment of the probe which, by reciprocity, is proportional to the electric field at the probe position [27]. Thus, the scattered wave electric field amplitude is proportional to the square of the electric field at the probe position. The scattered electric field will be reflected toward the input port and transmitted toward the output port. By changing the probe's scattering state between being open (reverse biased) and loaded (forward biased) at a fixed frequency, the reflected and transmitted scattered wave electric field amplitude from the region affected by the probe will thus be modulated. As this modulated signal reaches the input/output port it picks up an electrical phase delay which corresponds to the exact electrical position within the microwave circuit of the area directly beneath the probe. Through the use of modulated scattering and a quadrature homodyne mixer, the intensity ($|E|^2$) and phase delay of the scattered field can be determined.

3.2 First Order Theory

For completeness, the RF signal through the circuit will be traced using point 1 in figure 2.1 as a zero phase reference plane. All numerical subscripts in this section refer to points labeled in figure 2.1. The signal at point 1 is given by:

$$V_1 = V_o \sin(\omega t) \tag{3.6}$$

where V_o is the voltage amplitude at the output of the Wilkinson power divider at point 1 and ω is the frequency of operation. This signal will suffer a loss and a phase shift in going from point 1 to point 2. The signal that enters the DUT at point 2 is given by:

$$V_2 = V_o L_{21} \sin(\omega t - \phi_{21}) \tag{3.7}$$

where L_{21} is the loss and ϕ_{21} is the phase shift encountered by the RF signal in travelling from point 1 to point 2. The DUT is chosen to lie in the x-y plane at a height of z=0. If the scattering probe is at a position (x,y) over the DUT, the RF signal will experience an input loss, $L_i(x,y)$, and a net input phase shift $\alpha_i(x,y)$ to reach the point (x,y). If the height of the probe above the DUT is much smaller than a free space wavelength, then the phase shift dependence on z can be neglected. In addition, if the height of the probe is constant across the circuit, the phase delay's dependence on z is constant over the entire circuit. The electric field amplitude of the RF signal at the scattering point (x,y) at a height z above the circuit is given by:

$$\boldsymbol{E}(x, y, z) = A\boldsymbol{F}(x, y, z) L_{21} \sin(\omega t - \phi_{21} - \alpha_i(x, y)) \tag{3.8}$$

where $A(x, y, z)$ is the time independent electric field amplitude at the scattering point above the DUT. The input loss, $L_i(x, y)$, is included in the term $\boldsymbol{F}(x, y, z)$. If the DUT is operating with a single mode, the phase delay is the product of the propagation constant of the operating mode, β, and the electrical path length, $l(x,y,z)$, to the point (x,y,z) from the input reference plane. For example:

$$\alpha_i(x, y) = \beta l(x, y, z) \tag{3.9}$$

If there are many discontinuities in the DUT, higher order modes may be produced with each mode having a different propagation constant. The phase delay of the signal then becomes a net phase delay of all the higher order modes and is more difficult to deembed from the measurements.

A small modulated RF signal will be scattered proportional to the electric field amplitude intercepted by the scatterer and the dipole or monopole moment of the scatterer.

The moment has been shown to be proportional to the electric field intercepted by the scatterer [27]. The monopole scatters a signal proportional to the square of the normal electric field amplitude and the dipole scatters a signal proportional to square of the tangential electric field amplitude. Because the scattered signals from either the dipole or the monopole have the same mathematical form, the equations developed do not distinguish between scattering from the dipole or the monopole. As outlined by Cullen and Parr [27] and Hygate and Nye [33], the scattered voltage at the homodyne mixer will be related to the electric field amplitude at the scatterer by, $V_s = k|E(x,y,z)|^2$. The form of the modulated reflected signal that exits at the input reference plane (point 2) is:

$$V_{2m(r)} = L_{21} k_r |E(x,y,z)|^2 \sin(\omega t - \phi_{21} - \alpha_i(x,y) - \alpha_r(x,y) - \alpha_s) \quad (3.10)$$

The form of the transmitted scattered signal that exits at the output reference plane (point 3) is:

$$V_{3m(r)} = L_{21} k_t |E(x,y,z)|^2 \sin(\omega t - \phi_{21} - \alpha_i(x,y) - \alpha_t(x,y) - \alpha_s) \quad (3.11)$$

where $\alpha_r(x,y)$ and $\alpha_t(x,y)$ are the reflected and transmitted net phase delay in reaching the input and output ports, respectively, and have similar forms as equation (3.7). The constant phase shift of the signal caused by the scatterer is independent of position and is given by the term α_s. The proportionality constants, k_r and k_t, relate the reflected and transmitted voltages at the homodyne mixer to the square of the electric field at the probe position.

The form of the reflected modulated voltage incident on the quadrature mixer is:

$$V_{4m(r)} = L_{21} L_{42} (k_r |E(x,y,z)|^2) \sin(\omega t - \phi_{21} - \phi_{42} - \alpha_i(x,y) - \alpha_r(x,y) - \alpha_s) \quad (3.12)$$

where L_{42} is the loss of the signal and ϕ_{42} is the phase shift the wave encounters in traveling from point 2 to point 4. The transmitted modulated signal incident on the quadrature mixer is given by:

$$V_{4m(t)} = L_{21}L_{43}(k_t|E(x,y,z)|^2)\sin(\omega t - \phi_{21} - \phi_{43} - \alpha_i(x,y) - \alpha_t(x,y) - \alpha_s) \quad (3.13)$$

This signal is mixed with the LO signal which has the form:

$$V_6 = V_{LO}\sin(\omega t - \phi_{65}) \quad (3.14)$$

For a quadrature mixer with conversion loss, L_M, the mixer output voltage for the reflected signal is then:

$$\begin{aligned} I_r &= L_{21}L_{42}L_M(k_r|E(x,y,z)|^2)\sin(\phi_{65}-\phi_{21}-\phi_{42}-\alpha_i(x,y) - \alpha_r(x,y) - \alpha_s) \\ Q_r &= L_{21}L_{42}L_M(k_r|E(x,y,z)|^2)\cos(\phi_{65}-\phi_{21}-\phi_{42}-\alpha_i(x,y) - \alpha_r(x,y) - \alpha_s) \end{aligned} \quad (3.15)$$

where we have ignored any constant phase offset introduced by the mixer. The form of the output of the quadrature mixer for the transmitted signal is:

$$\begin{aligned} I_t &= L_{21}L_{43}L_M(k_t|E(x,y,z)|^2)\sin(\phi_{65}-\phi_{21}-\phi_{43}-\alpha_i(x,y) - \alpha_t(x,y) - \alpha_s) \\ Q_t &= L_{21}L_{43}L_M(k_t|E(x,y,z)|^2)\cos(\phi_{65}-\phi_{21}-\phi_{43}-\alpha_i(x,y) - \alpha_t(x,y) - \alpha_s) \end{aligned} \quad (3.16)$$

Because all loss terms which are not due to the DUT (L_{21}, L_{43}, etc...) and the mixer conversion loss are frequency dependent, they must be calibrated from the measurements before an electric field magnitude at one frequency can be related to the electric field magnitude at another frequency. This is achieved through S-parameter measurements of the system to determine the products $L_{21}L_{43}$ and $L_{21}L_{42}$ and through mixer conversion loss measurements versus frequency. After a calibration with respect to frequency, the loss terms between all test points and the mixer conversion loss can be factored out from the measurements. This allows field amplitude and phase images at different fre-

quencies of operation to be calibrated and compared. The form of the reflected signal after amplitude calibration is:

$$\begin{aligned} I_r &= (|E(x,y,z)|^2) \sin(\phi_{65}-\phi_{21}-\phi_{42}-\alpha_i(x,y) - \alpha_r(x,y) - \alpha_s) \\ Q_r &= (|E(x,y,z)|^2) \cos(\phi_{65}-\phi_{21}-\phi_{42}-\alpha_i(x,y) - \alpha_r(x,y) - \alpha_s) \end{aligned} \tag{3.17}$$

and the form of the transmitted signal after the same calibration is:

$$\begin{aligned} I_t &= (|E(x,y,z)|^2) \sin(\phi_{65}-\phi_{21}-\phi_{43}-\alpha_i(x,y) - \alpha_t(x,y) - \alpha_s) \\ Q_t &= (|E(x,y,z)|^2) \cos(\phi_{65}-\phi_{21}-\phi_{43}-\alpha_i(x,y) - \alpha_t(x,y) - \alpha_s) \end{aligned} \tag{3.18}$$

The magnitude of the square of the electric field in the direction of the probe can then be determined by:

$$|E(x,y,z)|^2 \propto \sqrt{I^2+Q^2} \tag{3.19}$$

Next, the net electrical phase delay at point (x,y) on the device under test can be determined. By taking the inverse tangent of the I and Q channels, the argument of the reflected and transmitted signal can be determined. If a single moded region of constant phase is chosen as a reference point such as a cross section along a 50 Ω microstrip line or coplanar waveguide transmission line at the input or output of the device under test, the phase delays due to the rest of the experiment can be subtracted from the argument of the signal. After such a calibration, the electrical phase delay for the reflected signal becomes:

$$\alpha_i(x,y) + \alpha_r(x,y) \tag{3.20}$$

and for the transmitted signal:

$$\alpha_i(x,y) + \alpha_t(x,y) \tag{3.21}$$

If the device under test is linear and reciprocal then $\alpha_i(x,y)=\alpha_r(x,y)$. The net phase delay from the scatterer to the output port, $\alpha_t(x,y)$, can be determined directly. If the device is nonreciprocal then the measured net electrical phase delay of the reflected and transmitted signal may be of little use for the circuit designer. From the intensity ($|E|^2$) and net electrical phase delay information for a single frequency and single mode of operation for a DUT, the time domain signal can be generated through the use of an inverse Fourier transform.

3.3 Calibration

The calibration of the electric field imaging system must be divided into several types. The first type will facilitate relating an electric field intensity map of a microwave circuit using a specific probe at one frequency with the electric field intensity map at another frequency in both magnitude and phase. For this type of frequency calibration, all the losses within the system including cable losses, insertion losses of microwave components, conversion losses of the mixers must be measured at the frequencies of interest. This type of "loss accounting" will help calibrate the electric field magnitudes but will not help with correlating the electric field phases. Figure 2.6 displays the overall conversion loss of the 2-18 GHz RF system which includes the losses in the cables, RF switches, circulators and mixer conversion loss. The system was not optimized for a flat frequency response due to time limitations.

To calibrate the electric field phases from one frequency to the next, a microstrip transmission line of low dielectric constant (around ε_r=2.2) is used as a calibration standard. The specific probe to be used is scanned across the microstrip line and an electric field cross section is taken at all frequencies of interest. Since the cross section of a single

mode microstrip line has constant phase, the measured phase at this reference position is stored and subtracted as an offset from the phase map.

Another type of calibration that is necessary is to relate the scattering amplitude of the monopole probe with the dipole probe in order to be able to create a complete vectorial electric field map above the circuit of interest. Both the dipole and the monopole scatter the near electric fields with differing efficiencies and add a small phase offset to the scattered microwave signal. The phase offset need not be taken into account because it will be calibrated out of the measurement from the frequency response calibration. The relative scattering efficiencies of the dipole and monopole probes need to be determined via an alternative approach. One possible calibration technique would be to compare the measured electric fields over a transmission line whose electric fields are very well known through Method of Moments (MOM) or Finite Difference Time Domain (FDTD) simulations. By comparing the electric field amplitudes from measurements and simulations over the same regions above a transmission line, the true ratios of the simulated normal and tangential electric fields can be determined, and a calibration factor that relates the measured tangential electric field amplitude with the measured normal electric field amplitude can be calculated. The calibration factor is a ratio of the measured normal and tangential field times the ratio of the simulated tangential and normal electric field at the same positions. Ideally, the calibration factor should not vary greatly over a simple transmission line if the monopole and the dipole probe are integrated on the same probe tip.

3.4 Verification of Electric Field Measurement

In order to verify that the measured voltage from the in-phase and quadrature components of the quadrature mixer are truly proportional to the square of the electric field amplitude, a measurement of the electric field at various heights and positions over a 50 Ω

microstrip transmission line is performed. The results are fitted to a first order model of the electric field decay of a line of charge and compared with theoretical calculations. The 50 Ω microstrip line is fabricated on Roger's Corporation RT/Duroid™ with a dielectric constant of ε_r=6.15 and a substrate thickness of h=0.38 mm. The experiment is performed at 10.0 GHz with a 150 μm long dipole on a 40 μm thick silicon substrate with a Schottky diode integrated at the tip of the dipole.

Figure 3.2 displays the measured transverse electric field intensity which is normalized to the peak signal at a reference height of 0 μm above the microstrip line. Because the plot is symmetric with respect to transverse position, the plot origin is centered with the microstrip center. As expected, the measured tangential electric field is at its lowest value at the center of the microstrip transmission line (at the origin).

Figure 3.3 displays the measured peak transverse electric field intensity versus height above the microstrip line. The measured values were fit to a first order electrostatic approximation of the electric field intensity near a line of uniform charge density. The tangential electric field intensity near the edge of the microstrip should decay as a function of $(1/h)^2$ where h is the height above the microstrip line. This model is valid to first order until a height is reached that is nearly the width of the microstrip line where the effects of the other side of the microstrip electric field need to be included in the approximation. From figure 3.3, it is apparent that the first order approximation is excellent when the height is smaller than the width of the microstrip line. After this point the measured signal begins to become deviates from the approximated signal.

The function used to fit the measured and calculated peak tangential electric field intensity contained two degrees of freedom, a variable amplitude (m2) and a positional

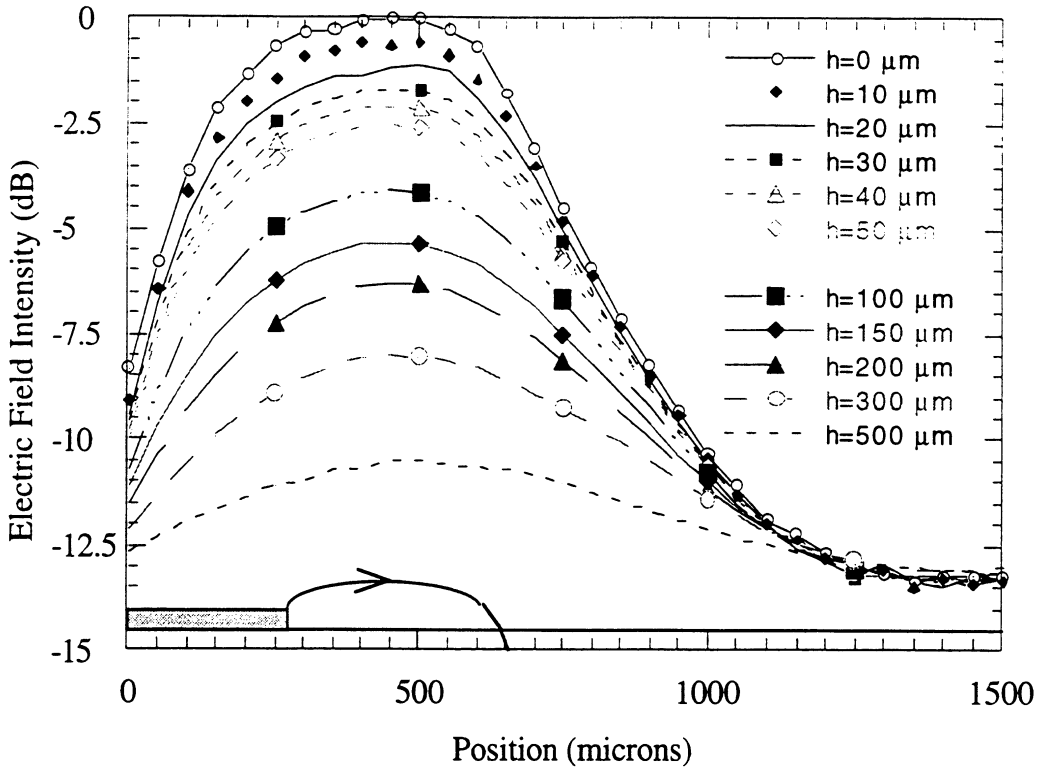

Figure 3.2: Measured tangential electric field intensity ($|E|^2$) with a 150 μm long integrated dipole versus transverse position at selected heights above a 50 Ω microstrip transmission line on Roger's Corporation RT/Duroid™ (ε_r=6.15, h=0.38 mm, w=0.56 mm). The microstrip line is centered at the origin.

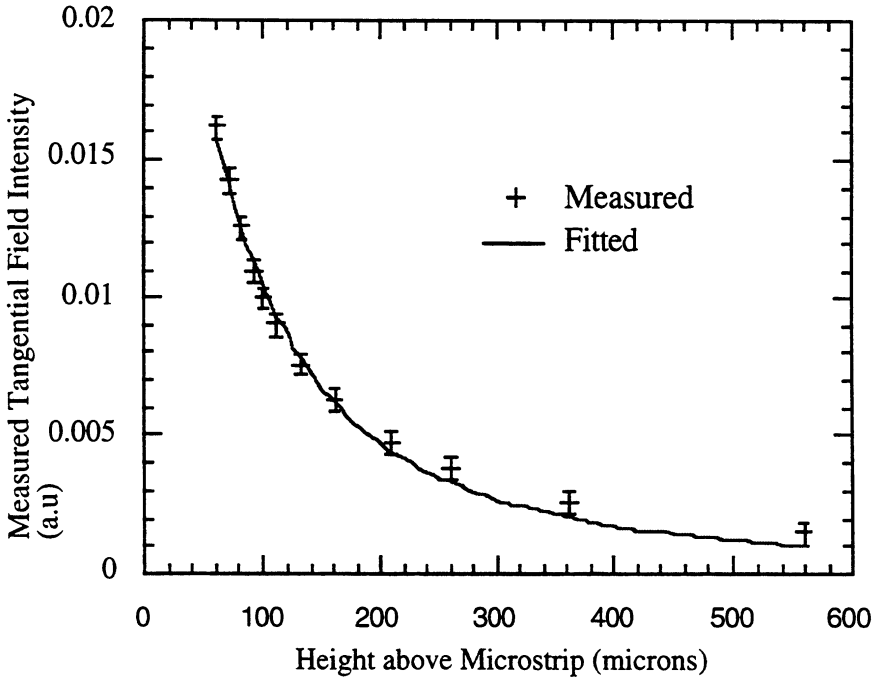

Figure 3.3: Peak tangential electric field intensity (E^2) versus height over a 50 Ω microstrip transmission line.

offset (m1 in microns). Equation 3.22 displays the form of the function used for the fit:

$$E^2(h) = m2\,(m1 + h)^{-2} \tag{3.22}$$

The correlation coefficient with the fitted curve is 0.997 and the peak intensity and offset coefficient are m2=448 and m3=107 μm. The variable m2 is an arbitrary scaling factor whereas the offset height m3 can be interpretted as the distance from the surface of the substrate (into the substrate) of the center of rotation for the curving electric field lines. Because the microstrip line substrate thickness is 380 μm, the offset height for the curve fit is a physically reasonable value.

3.5 Conclusions

In this chapter, a simplified theory for the modulated scattering system has been presented. The key issues are the necessity for measuring the in-phase and quadrature voltages of the scattered signal in order to be able to detect the electric field intensity and electrical phase delay. For linear reciprocal circuits, the reflected scattered signal provides a round trip electric phase delay and the transmitted scattered signal yields contours of constant phase along the signal path. The measured reflected and transmitted signals differ in the following way. The reflected signal magnitude contains the electric field amplitude at the position of the probe factored with the microwave signal path loss in traveling from the probe position to the input port. The transmitted signal contains the electric field amplitude factored with the signal loss in traveling from the probe position to the output port. If the circuits being tested are low loss (less than 2 dB insertion loss) and operating in a single mode (quasi-TEM) without higher-order harmonics, the electric field imaging system employing the modulated scattering technique accurately measures the electric field intensity in the direction of the monopole/dipole being used. The modulated scatter-

ing technique works for non-reciprocal microwave circuits; however, it is necessary to measure both the transmitted and reflected components.

CHAPTER IV

MEASUREMENTS

This chapter contains electric field measurements of various microwave transmission lines, circuits and planar antennas. The results are followed by a brief interpretation.

4.1 50 Ohm Microstrip Transmission Line

At first, the validity of the experimental measurements are verified using a 5 cm long straight section of 50 Ω microstrip on RT/Duroid™ 5880 (ε_r=2.2, h=380 μm, w=1190 μm). A hybrid monopole probe of length 250 μm is scanned over the microstrip line with three different SMA terminations at 9 GHz (open, short, 50 Ω load). Figures 4.1a) and 4.1b) display the raw data (voltages) collected from the in-phase signal and the quadrature signal of the 50 Ω microstrip line with a matched load termination. Note how the peaks of the quadrature voltage are spaced every 6,100 μm. This corresponds exactly to a spacing of $\lambda_{eff}/4$ at 9 GHz where $\lambda_{eff}/4$ is calculated using the equation [46]:

$$\varepsilon_{eff} = \frac{\varepsilon_r + 1}{2} + \frac{\varepsilon_r - 1}{2}\left(\frac{1}{\sqrt{1 + 12\frac{d}{w}}}\right) \tag{4.1}$$

where where d is the dielectric thickness and W is the width of the microstrip. If the microstrip line is lossless and reciprocal, and if the probe moves along a line parallel to the microstrip line, then $\alpha_i = \alpha_r$.. The forms of the in-phase and quadrature signals from equation (3.15) reduce to:

$$I_r = B(x,y,z)\sin(\phi_o - 2\alpha_i(x,y)) = B(x,y,z)\sin\left(\phi_o - 2\left(\frac{2\pi l}{\lambda_{eff}}\right)\right)$$
$$Q_r = B(x,y,z)\cos(\phi_o - 2\alpha_i(x,y)) = B(x,y,z)\cos\left(\phi_o - 2\left(\frac{2\pi l}{\lambda_{eff}}\right)\right) \quad (4.2)$$

where the positionally invariant phases have been combined into the term ϕ_O, the positionally invariant losses and positionally varying reflected signal have been combined into the term $B(x,y,z)$, and the positionally varying phase term $(\alpha_i+\alpha_r)=2(2\pi l/\lambda_{eff})$. The equations predict that the maxima and minima along a transmission line for the in-phase and quadrature signals are separated by a distance of $\lambda_{eff}/4$ as can be clearly seen in figures 4.1a and 4.1b.

The next step to validate the operation of the electric field imaging system is to combine the two signals (in-phase and quadrature) and examine the intensity of the normal electric field over the microstrip (Fig. 4.1c). It is seen that the intensities are nearly constant along contours parallel to the microstrip line. An intensity ripple of 1 dB is present along the line which may be due to the non-ideal match of the termination or the non-ideal connections made with the SMA connectors at the input and output of the device.

The final validation is to check the phase variation of the signals along the microstrip line. The phase for a transmission line with a matched load will vary linearly with position and this is clearly seen from the measurements (Fig. 4.1d). The measured phase cycles by 2π every 13,000 μm which is $\lambda_{eff}/2$ as is predicted from equation 4.1 because the roundtrip phase delay is measured. The slight tilt in the phase contours with respect to the microstip line cross section is possibly due to a variation in the height of the probe across the microstrip line.

Figure 4.2a) displays the data collected from the same microstrip line with an open

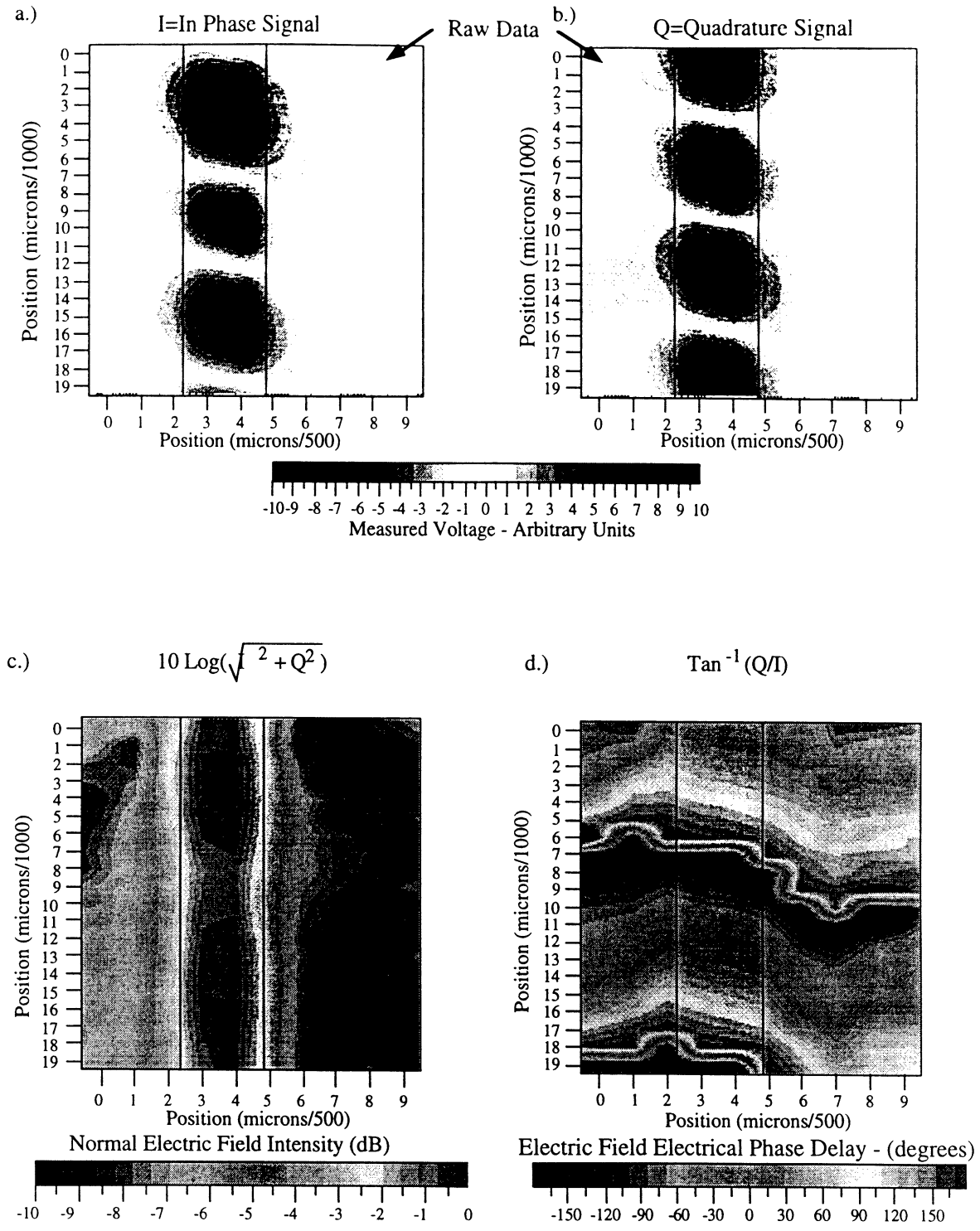

Figure 4.1: a) and b) Raw data from normal electric field measurements with a 250 μm long hybrid monopole directly above a 50 Ω microstrip line fabricated on Roger's Corp. RT/Duroid (ε_r=2.2, w=1190 μm, h=380 μm) at 9 GHz terminated with a 50 Ω load. c) Normal electric field intensity. d) Normal electric field phase delay.

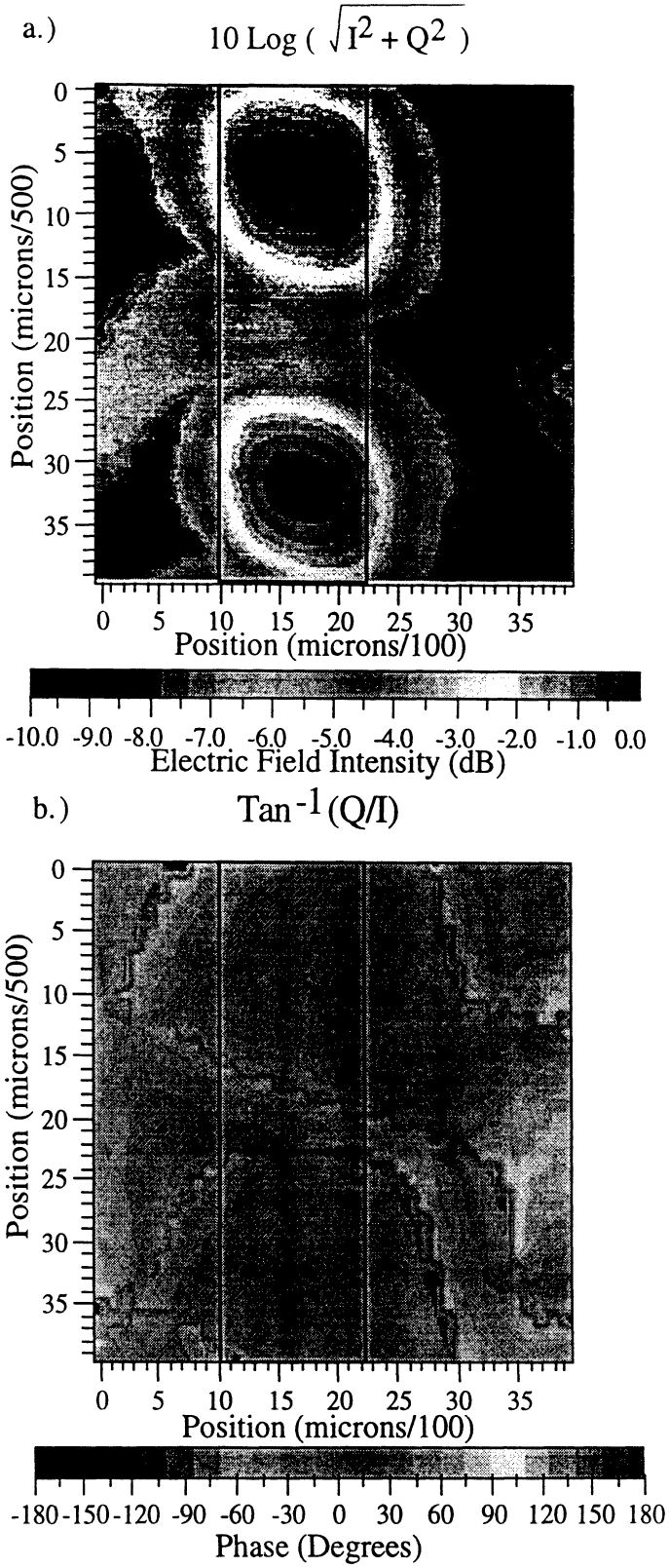

Figure 4.2: a) and b) Normal electric field images (intensity ($|E|^2$) and phase delay) measured with a 250 μm long hybrid monopole from a 50 Ω microstrip line fabricated on Roger's Corporation RT/Duroid (ε_r=2.2, width=1190 μm, and substrate height=380 μm) at 9 GHz terminated with an open.

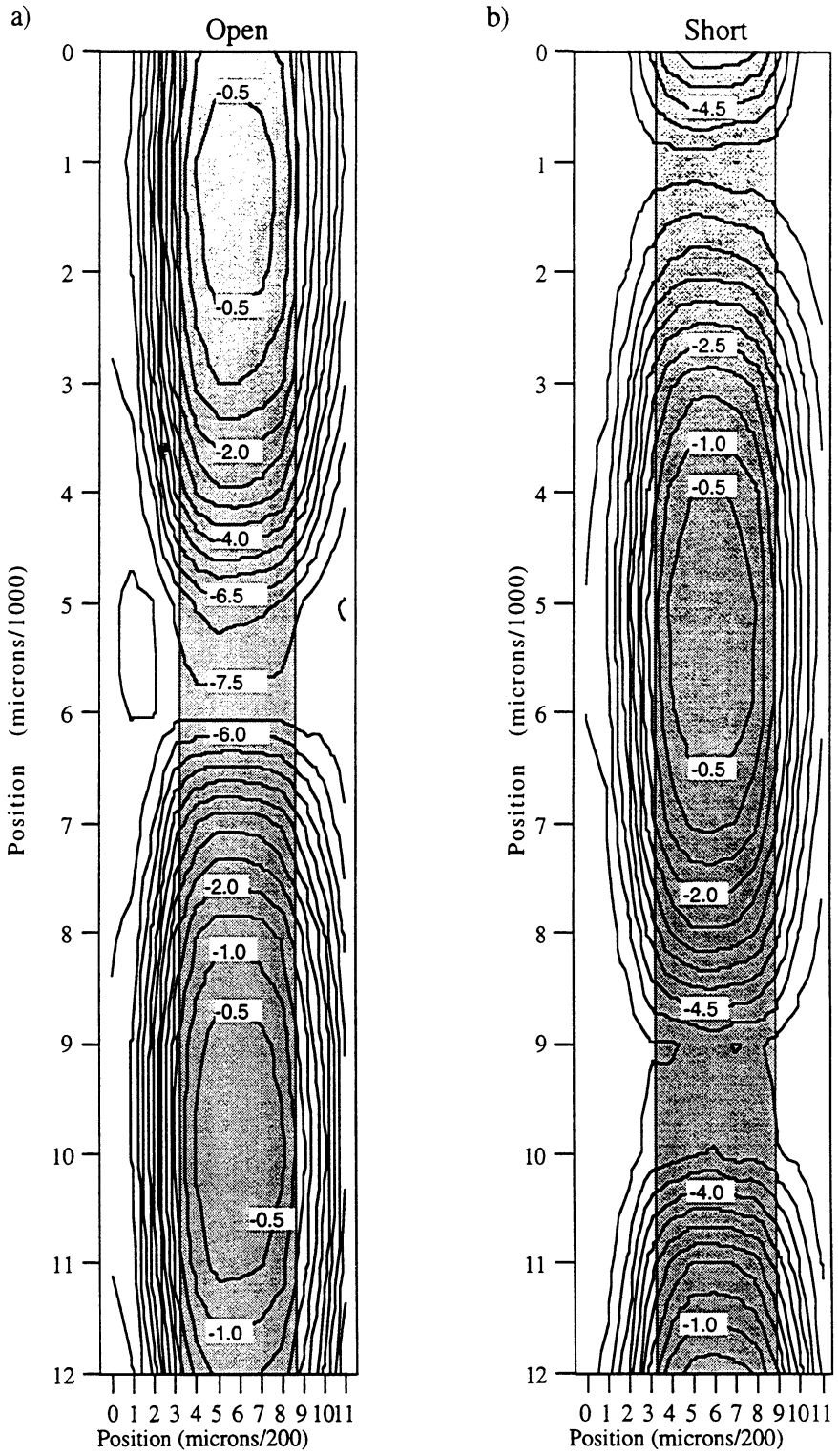

Figure 4.3: Normal electric field intensity ($|E|^2$) of the microstrip line from figure 4.1 at 9 GHz measured with a 100 μm long integrated monopole probe. The fields were tested at a height of 20 μm above the microstrip a) with an SMA open and b) with an SMA short.

at the end of the SMA connection at 9 GHz. The normal electric field intensity image in figure 4.2a) displays standing waves with a -8 dB null in the center. Due to the spatial averaging of the monopole combined with the rapid decay of the normal electric fields from this transmission line, the dynamic range of the system for this measurement is only 10 dB. Typically, the signal to noise ratio for the monopoles is much lower than for dipoles of the same size. The separation of the peaks is again 13,000 μm which is $\lambda_{eff}/2$. Figure 4.2b) displays the electrical phase delay of each point over the microstrip line and gives a zero phase response everywhere due to the presence of the standing waves. Normal electric field intensity images of the microstrip line with both open and shorted SMA terminations were compared over the same area in figure 4.3 with the use of a 100 μm long integrated monopole probe. As predicted by transmission line theory, the nulls in the shorted microstrip line occur in the same position as the peaks of the open microstrip line and vice versa.

4.2 55 Ohm Coplanar Waveguide Transmission Line

A 55 Ω coplanar waveguide (CPW) transmission line is fabricated and tested using Rogers Corporation RT/Duroid®, ε_r=10.8, and a dielectric thickness of 2,500 μm. The S-parameters were measured and modeled with HP-EESof's LIBRA and the line impedance is found to be 55 Ω. The slot width is 255 μm and the center conductor width is 560 μm. Figure 4.4 displays a combined plot of the measured normal (100 μm long integrated monopole) and tangential (150 μm long integrated dipole) electric field intensity along a cross section of the CPW line. The normal fields peak at the center conductor and are minimum across the slot and the tangential electric fields peak across the slot and are minimum over the center of the CPW line as expected from simple electrostatic theory. Due to the finite size of the dipole and spatial averaging effects, the null in the tangential electric field never completely goes to zero. The values from each electric field component are

normalized to their own peak value and could not be related to each other due to variations in diode quality, probe bias and probe position.

Figure 4.5a-c) displays three images of the measured normal electric field intensity over the coplanar waveguide line under different terminations (50 Ω load, open and short) at 2.3 GHz (λ_{eff}=53.7 mm). In figure 4.5a (load termination) the normal electric field is nearly constant over contours parallel to the CPW line. Figure 4.5b shows the normal electric fields when the CPW line is terminated with an open. The presence of standing waves can clearly be seen with the nulls of the fields occurring at the top and bottom of the image. As was seen in the case of the microstrip line, the peak of the open CPW line (Fig. 4.5b) occurs in the same position as the null of the shorted CPW (Fig. 4.5c).

Figure 4.6a-c) displays the tangential electric field intensity of the same CPW line as in figure 4.5a-c) with the same terminations (50 Ω load, open, and short). As expected, the tangential electric field is a minimum over the center conductor and is a maximum over the gaps of the CPW. In this specific case, a hybrid probe is used which contained both a monopole and a dipole scatterer with hybridly mounted diodes. The asymmetry in the measurement is most likely due to the interference of the hybrid monopole probe with the signal of the hybrid dipole probe. The hybrid monopole probe should be separated farther than 1 mm to minimize the interference with the dipole probe. It is expected that when the monopole and dipole probes are simultaneously in regions of strong normal and tangential electric fields that the coupling between the probes will yield undesirable results. This effect did not occur with the normal electric field images because the dipole was aligned parallel to the CPW line so that there were no strong tangential electric fields in the same direction as the center conductor line.

Another important measurement is the phase of the electric field across the gaps of the coplanar waveguide. If the CPW line is operating in the odd mode, the measured

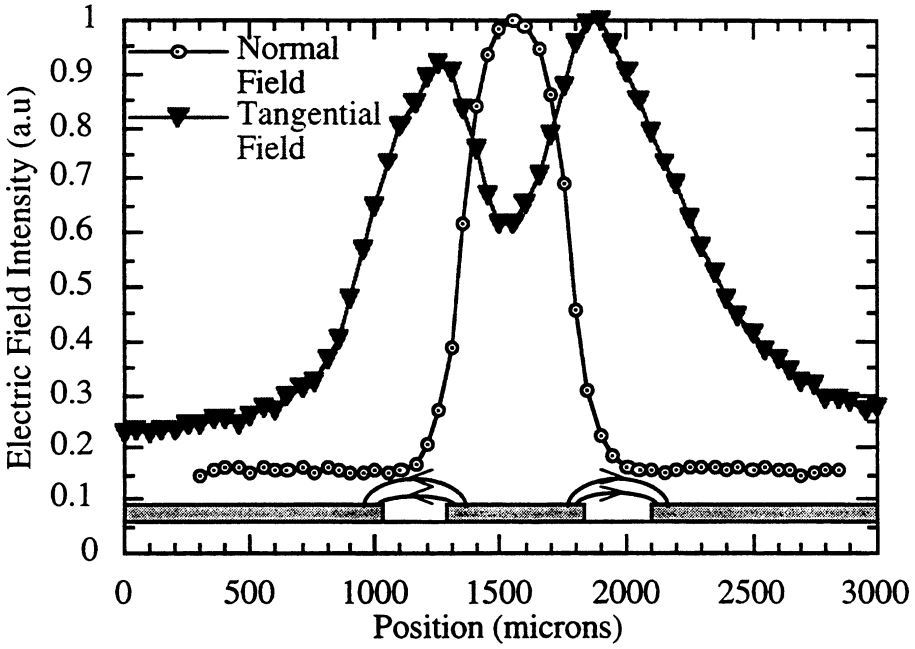

Figure 4.4: Normal and tangential electric field intensity ($|E|^2$) cross section over the CPW line measured with a 150 μm integrated dipole and a 100 μm long integrated monopole. Each field component has been normalized to itself.

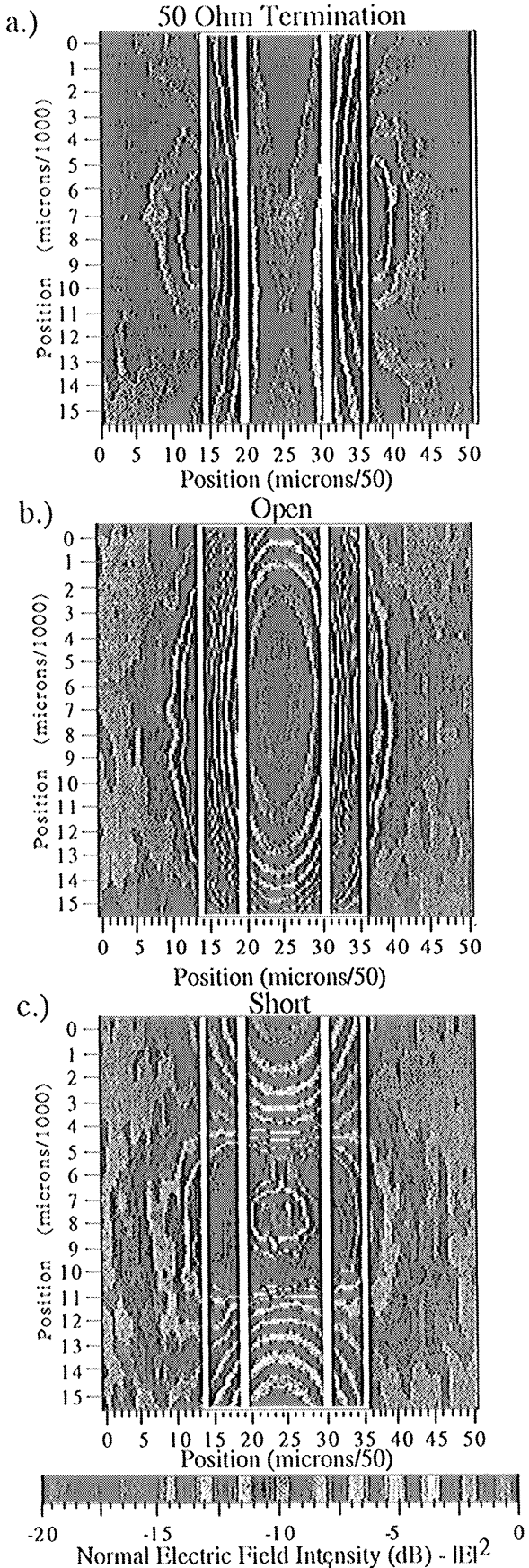

Figure 4.5: Normal electric field intensity ($|E|^2$) over a 55 Ω CPW line terminated a) with a 50 Ω SMA load, b) with an open and c) with an SMA short.

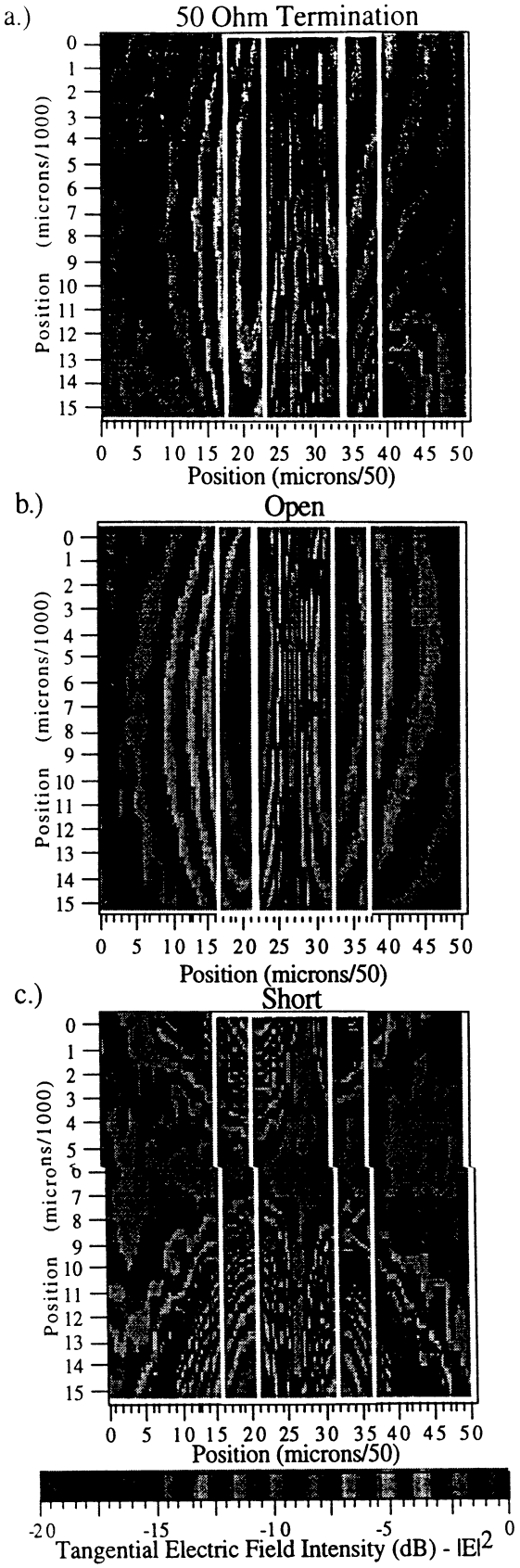

Figure 4.6: Tangential electric field intensity over a CPW line at 2.3 GHz. The line is terminated a) with a 50 Ω SMA load, b) with an open and c) with an SMA short.

phase of the electric field across one gap should be 180° out of phase with the measured electric field phase across the opposite gap. Figure 4.7 displays the tangential electric field phase measured from the coplanar waveguide line at 2.5 GHz with the 150 μm dipole with the integrated diode at the tip. As in the case of the 50 Ω microstrip line that is terminated with an open/short, there is no phase variation along the length of the line due to the presence of standing waves, but there is an oppositely directed electric field on one side of the gap of the CPW line compared to the other side of the gap. When the CPW line was measured with a 50 Ω termination at these frequencies, the phase varied linearly along the length of the transmission line but at each cross section, the phase is 180° opposite across one gap when compared to the other gap.

Similar tests were performed at 12 GHz where the CPW line is not performing well (high losses and not operating in a single mode). There are no air bridges across the CPW line to equalize the ground plane and therefore the ground planes do not locally remain at the same potential. Thus, at the higher frequencies, there is phase variation across the gaps of the CPW line and higher order modes may be propagating along the CPW line. The measured VSWR on the line at 12 GHz is 2.15 and it is observed that with a 50 Ω termination, the standing waves are visible on the line from the electric field intensity image in figure 4.8.

Figure 4.9 displays the same coplanar waveguide line but with open and shorted terminations. From the images it is clear that the CPW line is not operating in a single mode because the tangential electric field intensity across each gap is not symmetric and the ground plane appears to have a nonzero tangential electric field component above it. The electric field intensity peaks of the open CPW line also line up with the nulls of the shorted CPW line as expected.

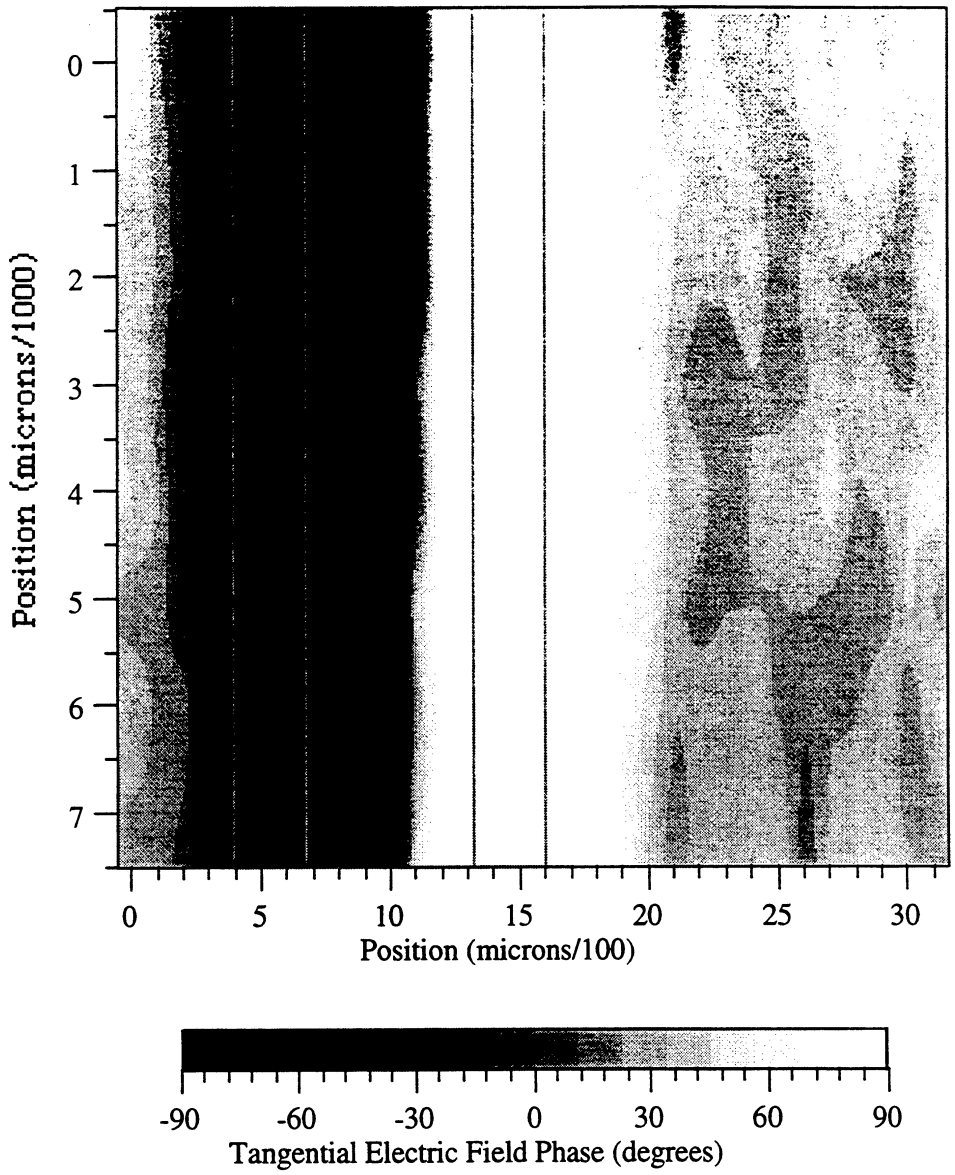

Figure 4.7: Tangential electric field phase at 2.5 GHz of a coplanar waveguide transmission line terminated with an open that is measured with a 150 μm long integrated dipole probe. The phase difference across each gap is 180°.

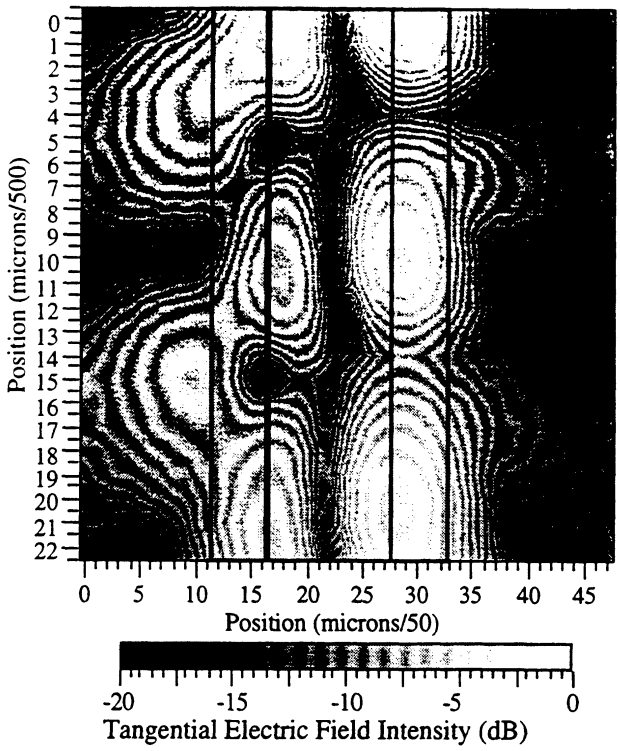

Figure 4.8: Tangential electric field intensity ($|E|^2$) of a coplanar waveguide transmission line with a 50 Ω SMA termination at 12 GHz measured with a 150 μm long dipole with an integrated Schottky diode at the antenna.

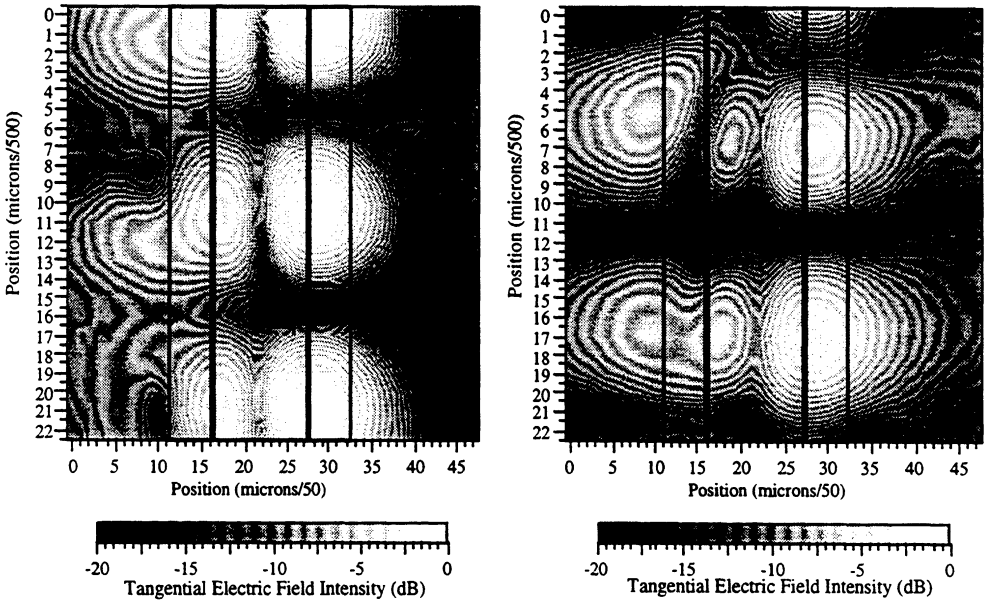

Figure 4.9: Tangential electric field intensity ($|E|^2$) of an open (left) and shorted (right) coplanar waveguide line at 12 GHz measured with a 150 μm long integrated dipole.

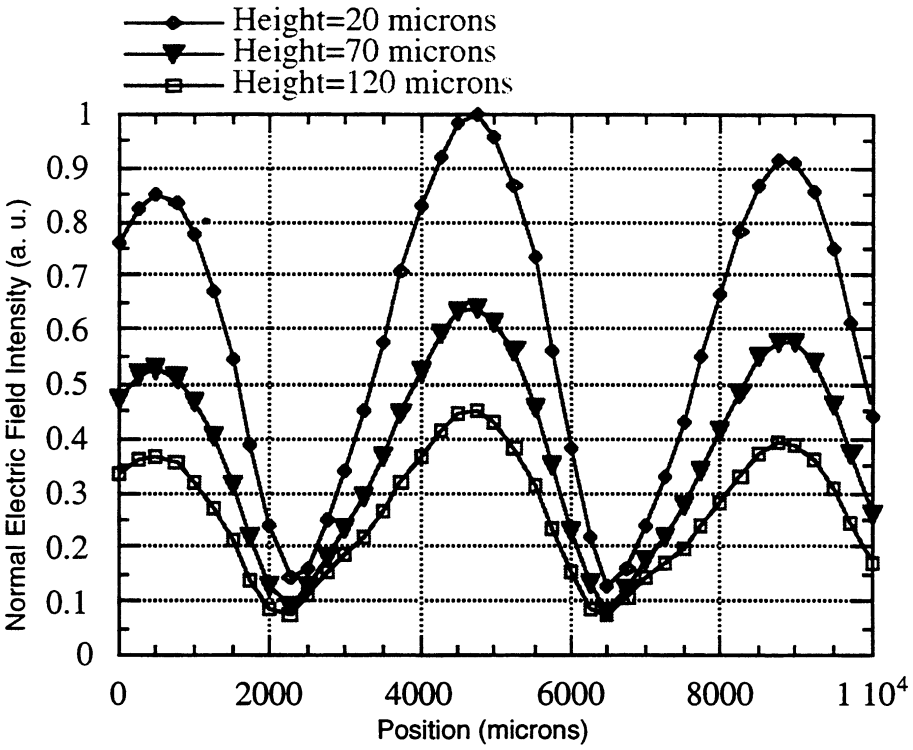

Figure 4.10: Normal electric field intensity ($|E|^2$) along CPW center conductor at various heights measured with a 100 μm long integrated monopole probe at 15 GHz.

Figure 4.10 displays the normal electric field intensity along the center conductor of the CPW line at 15 GHz at three separate heights: 20 μm, 70 μm and 120 μm. From this figure it is easy to measure the propagation constant of the CPW line. The propagation constant from a sinusoidal fit gives a period of 4180 μm ($\lambda_{eff}/2$) which corresponds well with the calculated (LineCalc™) half-guided wavelength of 4115 μm. This figure also displays how the shape of the electric field measurement is maintained and decays as the height of the probe increases.

4.3 Meander Line

A three turn meander line is fabricated and studied by Harokopus [47]. The meander line is built on a 635 μm thick Rogers Corporation RT/duroid® with a dielectric constant of 9.88. Figure 4.11 displays the meander line geometry and figure 4.12 displays the measured scattering parameters of the meander line. The meander line behaves as a low pass filter until the path length of the meandered lines becomes long enough that the closest lines destructively interfere with each other. The maximum rejection occurs at a frequency of 13.4 GHz.

The tangential electric field intensities in the direction of the input and output microstrip lines were measured with a 150 μm long dipole on 40 μm thick silicon with an integrated Schottky diode at the dipole. Three frequencies were measured: 8.8 GHz (passband), 11.7 GHz (end of passband), and 13.4 GHz (rejection band). Figure 4.13 displays the tangential electric field intensities at a height of 30 μm above the meander line. At 8.8 GHz the tangential electric field intensity appears to be very uniformly distributed across the gaps of the meander line whereas at the edge of the passband at 11.7 GHz the tangential electric field becomes asymmetric and nonuniform. In the rejection band, the tangential

electric fields across the middle gap are reduced by 15 dB from the peak field value. The fields are further reduced by more than 20 dB at the gap closest to the output port.

The tangential electric field phase plots in figure 4.14 display a slowly varying phase component along the gap of the meander line for part a) at 8.8 GHz, a rapidly varying phase component for part b) at 11.7 GHz and little phase information along the gap for the rejection band in part c) at 13.4 GHz. The measured phase cycles between 0° and 90° and differs from previous measurements in the following manner. The lock-in amplifier used for the meander line measurements was a Stanford Research Systems SR-530 Lock-In Amplifier in the Magnitude-Phase mode (R-Ø mode). Because only the magnitude was measured for the in-phase signal and the quadrature signal, the phase can only change over a 90° range. The benefit of using the SR-530 is that the signal voltage range can be controlled over the IEEE-488 Instrument Bus. Previous measurements were performed with the Princeton Applied Research (PAR) Model 124A Lock-In Amplifier where automated ranging is not possible.

4.4 Directional Coupler

A single stage microstrip coupled-line directional coupler is fabricated on 380 μm thick high resistivity silicon. Figure 4.15 displays the layout of the directional coupler used for this experiment. The device is tested at 10 GHz where the input reflection coefficient ($|S11|^2$) was measured with a network analyzer to be -14 dB, the transmission to the directed port ($|S21|^2$) was -3 dB, the coupling ($|S31|^2$) was -15 dB and the isolation ($|S41|^2$) was not measured because the isolated port was terminated with a 50 Ω thin film resistor. It is expected that each SMA connector contributes 0.3 dB of loss at 10 GHz and that the 1 cm long microstrip line to the coupler contributes 0.8 dB of loss as well. After taking these initial losses into account, the directional coupler is expected to have -12 dB

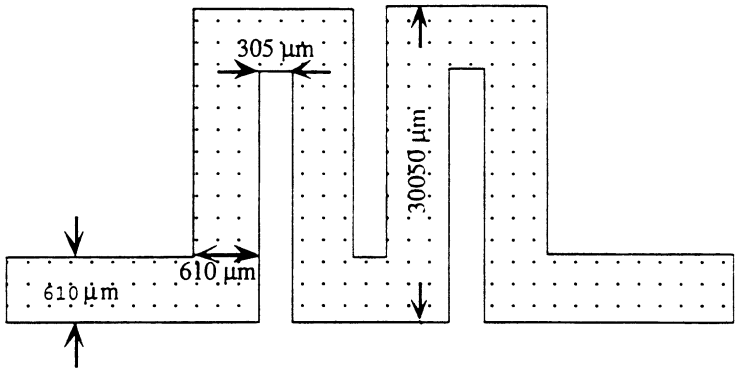

Figure 4.11: Geometry of the three turn microstrip meander line used for measurements.

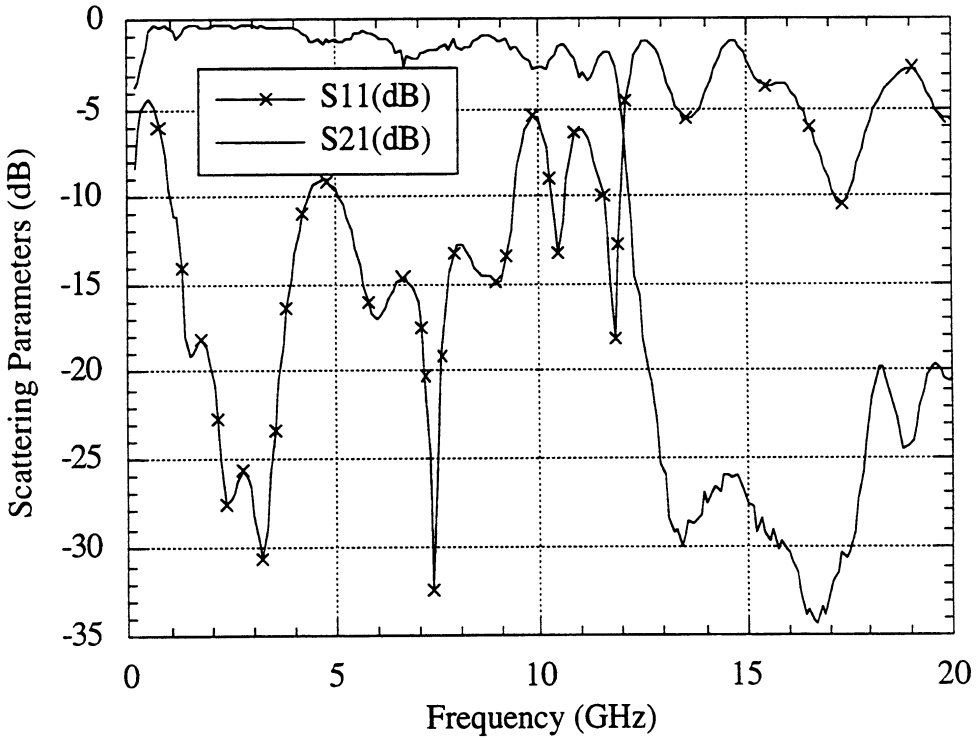

Figure 4.12: Measured scattering parameters of a three turn meander line.

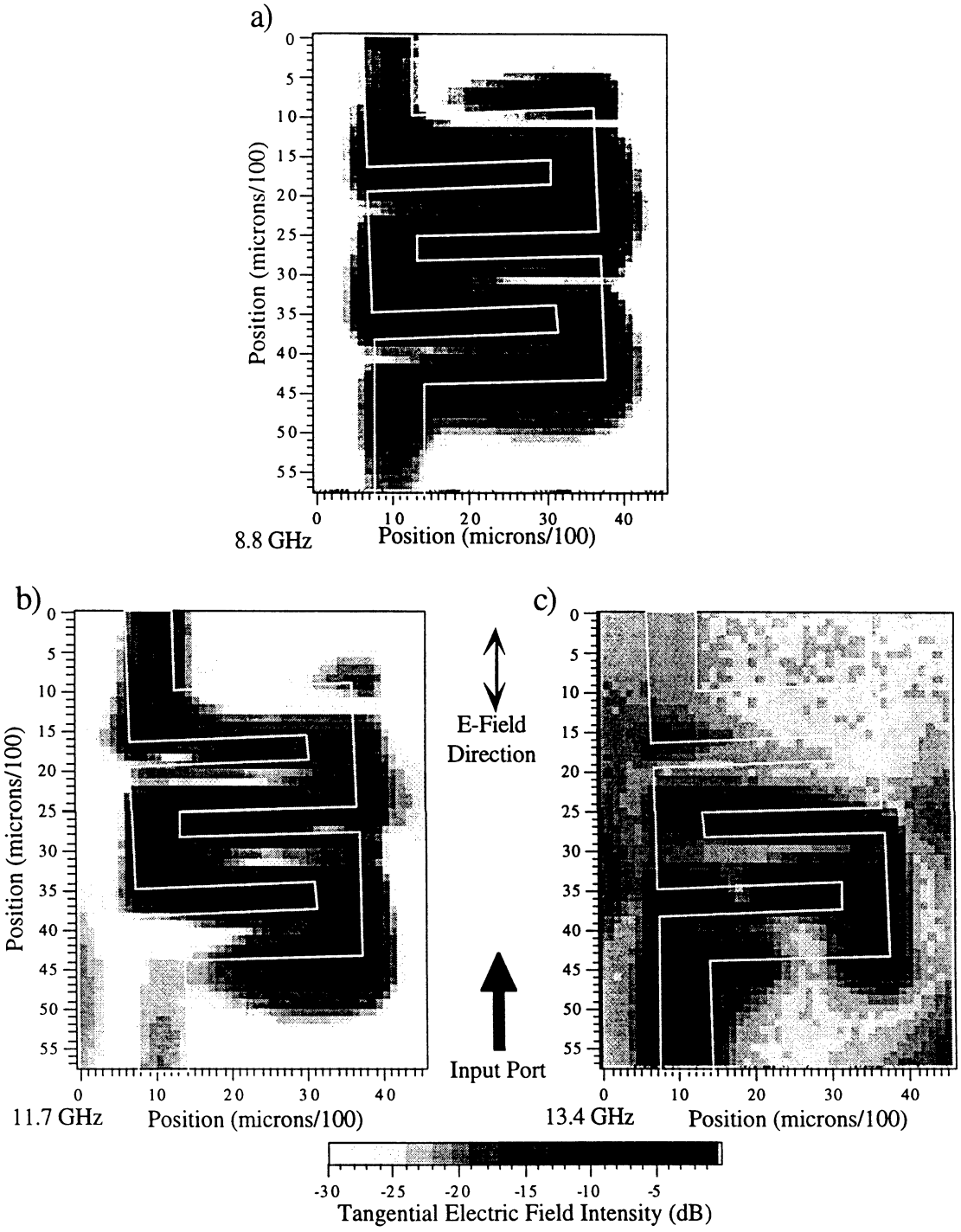

Figure 4.13: Meander line measured tangential electric field intensity ($|E|^2$) with a 150 μm long integrated dipole at a) 8.8 GHz (passband), b) 11.7 GHz (edge of passband) and c) 13.4 GHz (rejection band).

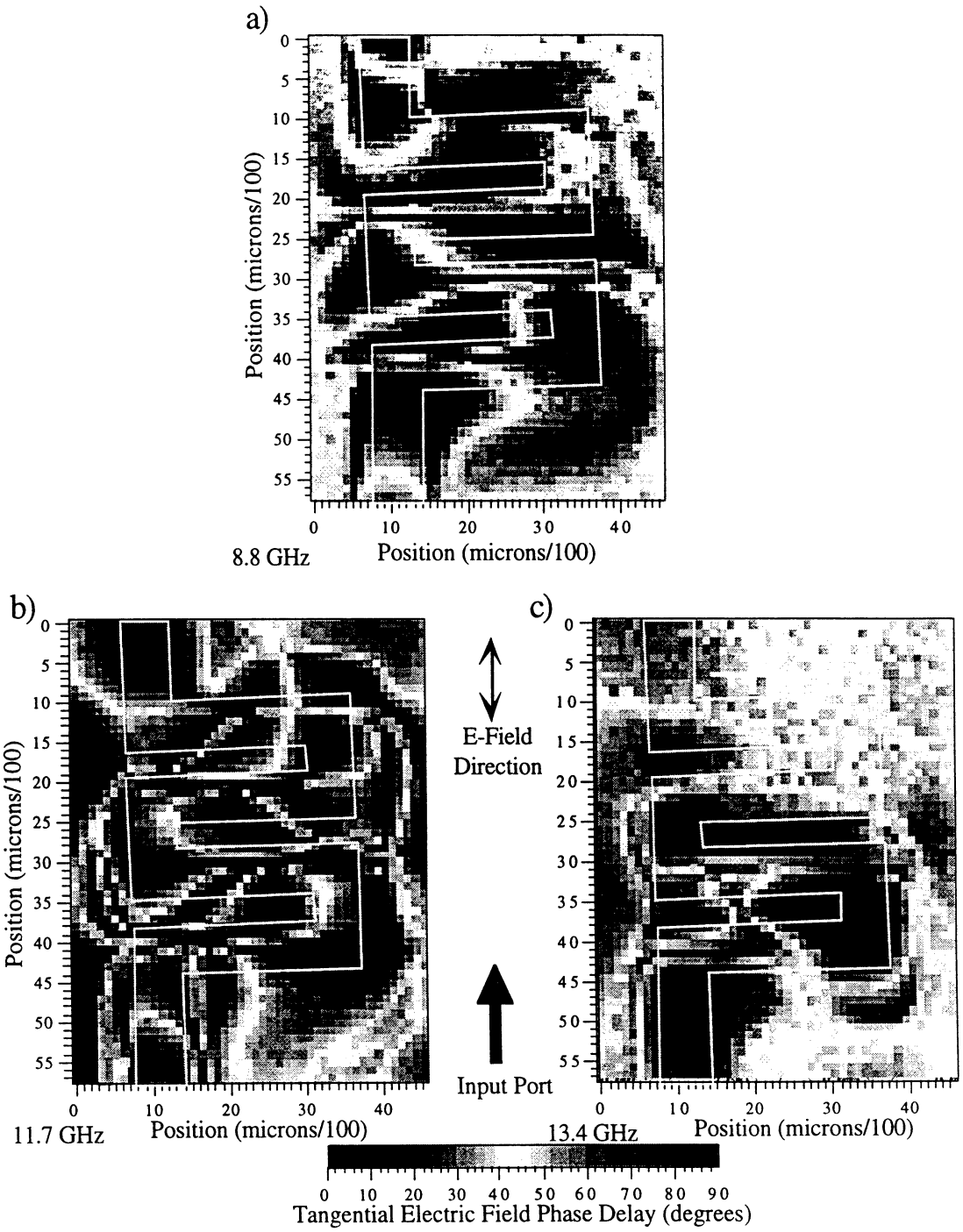

Figure 4.14: Meander line electrical phase delay of the measured tangential electric field with a 150 μm long integrated dipole at a) 8.8 GHz (passband), b) 11.7 GHz (edge of passband) and c) 13.4 GHz (rejection band).

of coupling ($|S31|^2$) at 10 GHz.

Figure 4.16 displays contours of the normal electric field intensity at 10 GHz that are measured with a 100 μm long integrated monopole and figure 4.17 displays the same data in three-dimensional form. The important features of these figures are that the normal electric field is nearly constant between the input and directed port microstrip line and that the isolated port does not appear to have a normal electric field intensity ($|E|^2$) within the range of the measurements. The coupled port has a normal electric field intensity component which is -12 dB compared to the peak normal electric field intensity over the input microstrip line. This value agrees with the measured coupling value of -12 dB and again demonstrates the basic theory developed for modulated scattering in Chapter III. Due to the presence of standing waves at the input and directed port, it is very difficult to choose specific locations to make this type of comparison, especially because the measurement region is very close to the coupling section. A better way to make this comparison would be to test the microstrip lines far from the directional coupler and compare the average measured intensities over at least half a guided wavelength.

Without taking dielectric losses into account, simulations predict that S21 should be -1 dB. Modulated scattering theory predicts that the normal electric field intensity measured at the directed port should be -1 dB lower than the measured normal electric field intensity at the input port. By comparing the normal electric fields over the input microstrip line and the directed port microstrip line, it is seen that the levels are within this difference. The normal fields over the directed port decay slightly more rapidly in intensity than the input port electric field intensity as predicted by modulated scattering theory and at symmetric locations at the input and directed port, the measured normal electric field intensity levels appear to differ by 1 dB. This type of comparison may not always be

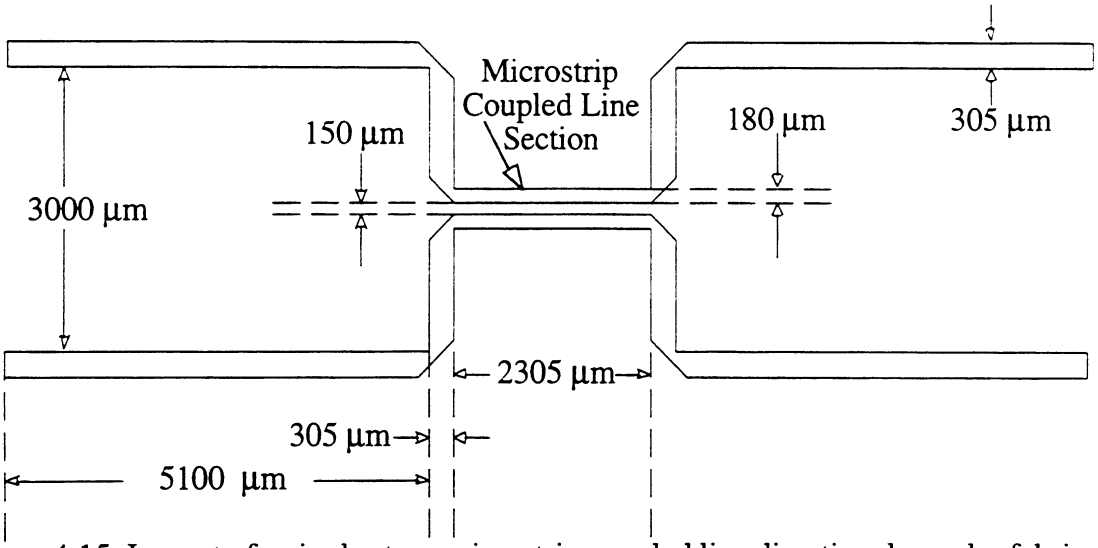

Figure 4.15: Layout of a single stage microstrip coupled line directional coupler fabricated on 380 µm thick silicon.

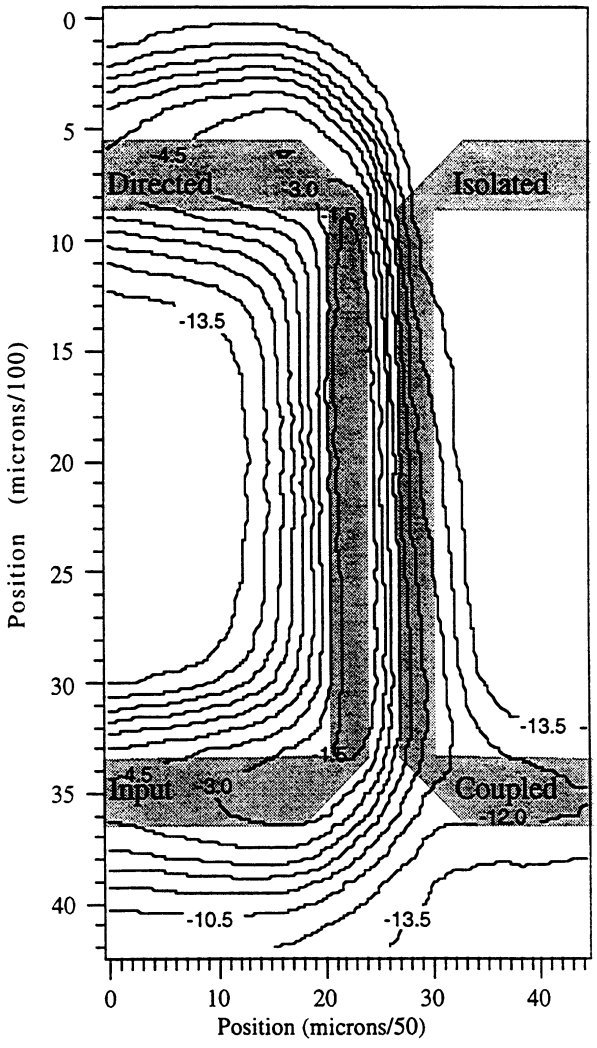

Figure 4.16: Contour plot of the normal electric field intensity measured with a 100 µm long integrated monopole at 10 GHz.

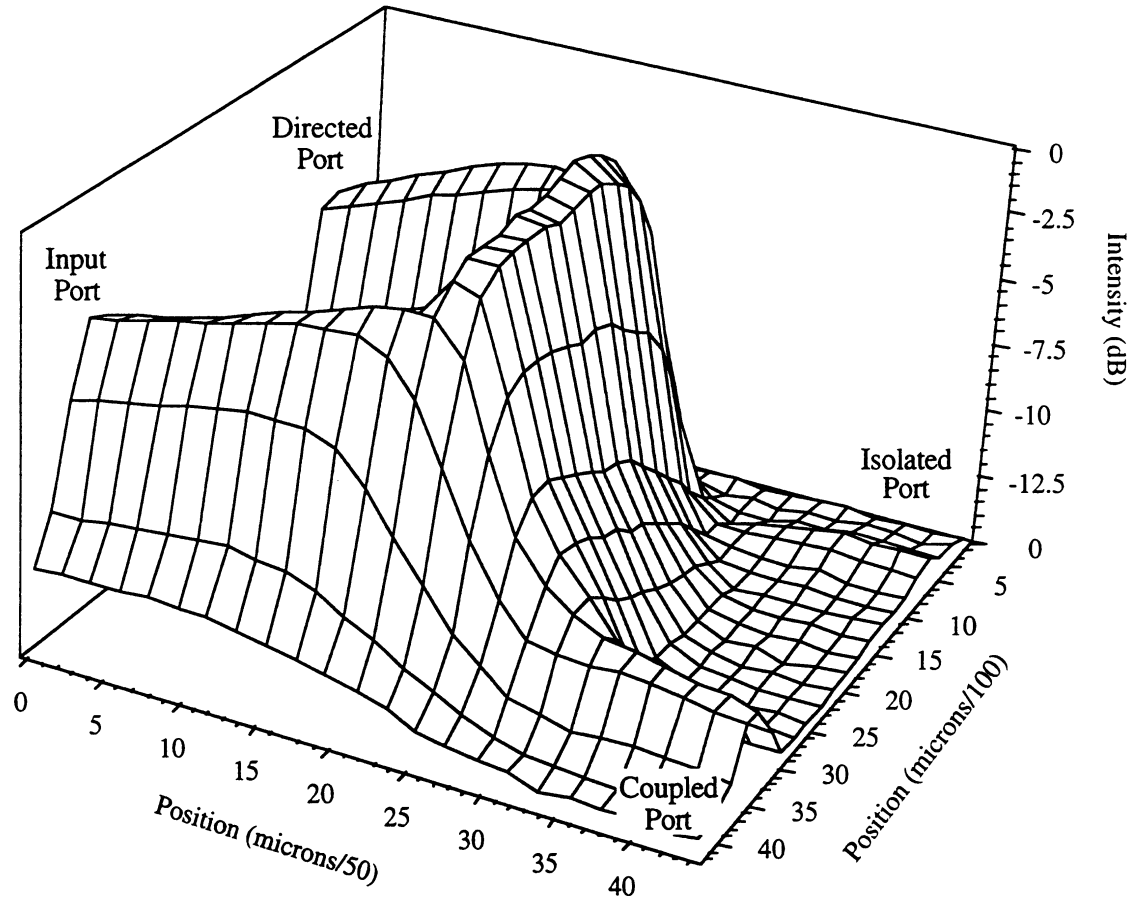

Figure 4.17: Surface plot of the normal electric field intensity ($|E|^2$) measured with a 100 μm long integrated monopole at 10 GHz.

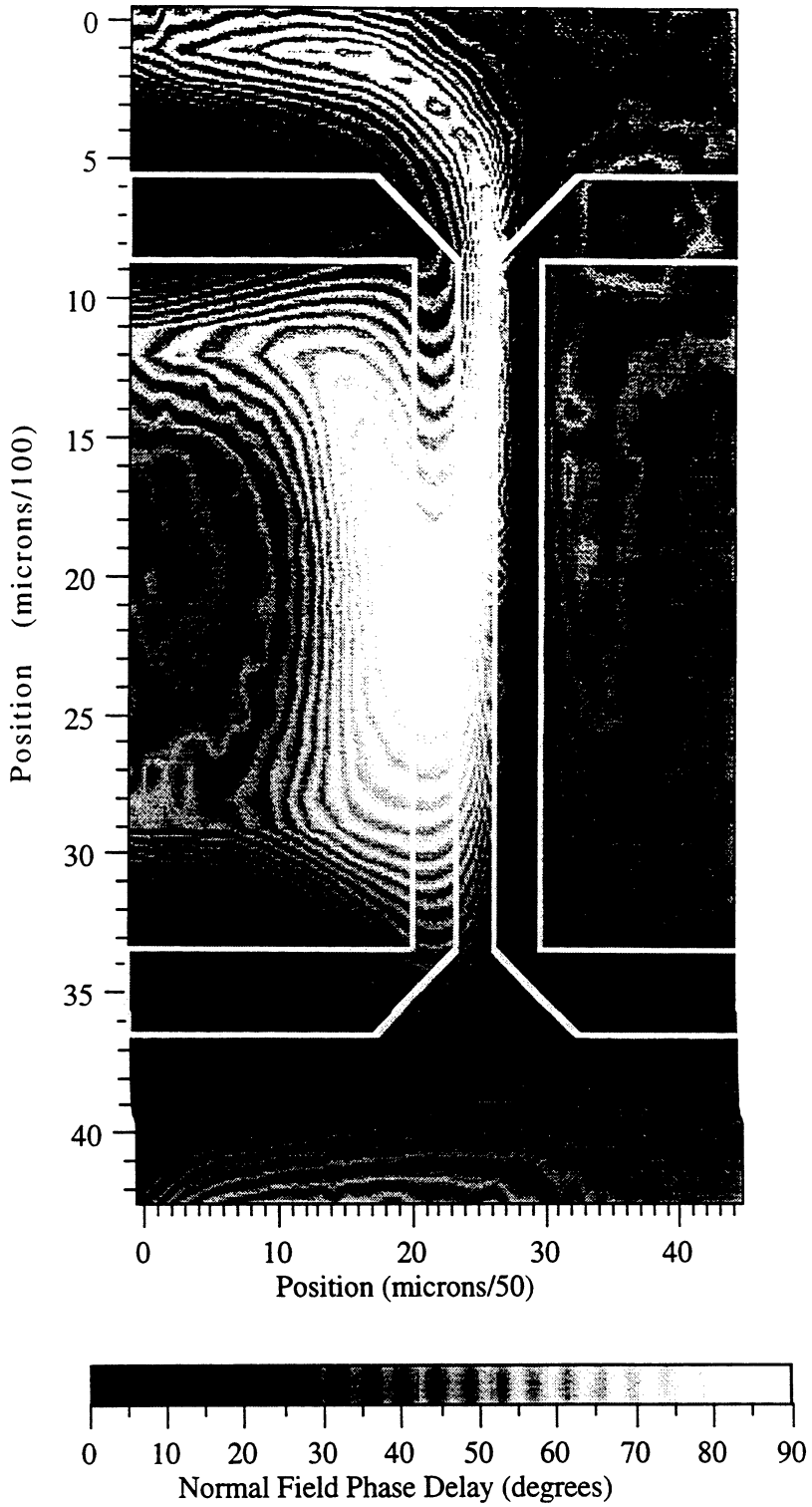

Figure 4.18: Normal electric field phase delay at 10 GHz measured with a 100 μm long integrated monopole. The input port is the lower left microstrip line.

valid when there are standing waves over the input port that would make comparing the normal electric fields from symmetric locations impossible.

Figure 4.18 displays the round trip normal electric field phase delay over the same region as in figure 4.16. The phase delay varies linearly along the length of the input and output microstrip lines and changes rapidly from 90° at the input side of the center section to 0° in the coupled side of the center section. The measured phase difference from the S-parameters between the directed port and the coupled port is around 96°. Modulated scattering theory predicts that an electrical phase delay of twice this value (192°) will be observed in the measurements. As with the meander line measurements, the SRS 530 Lock-In Amplifier is used and introduces a phase ambiguity that makes differences greater than 90° difficult to distinguish.

4.5 Microstrip Patch Antenna

A microstrip patch antenna is fabricated on Roger's Corporation RT/Duroid™ (εr=2.2, h=0.635 mm) and tested at the first resonance frequency of 12.85 GHz. The patchantenna's width is 9120 μm, length is 7410 μm and the input microstrip line width is 1960 μm. Figure 4.19 displays a schematic of the expected electric fields near a patch antenna operating in the fundamental mode. The edges that are perpendicular to the microstrip input line are the radiating edges of the patch antenna. By using the modulated scattering system with hybrid probes (250 μm long dipole and a 200 μm long monopole), all electric field component intensities and phases were measured.

Figure 4.20 displays the measured electric field intensities that were collected with a spacing of 1000 μm in each direction. Because the electric fields around the patch antenna do not change very rapidly with position, this spacing is adequate to display the

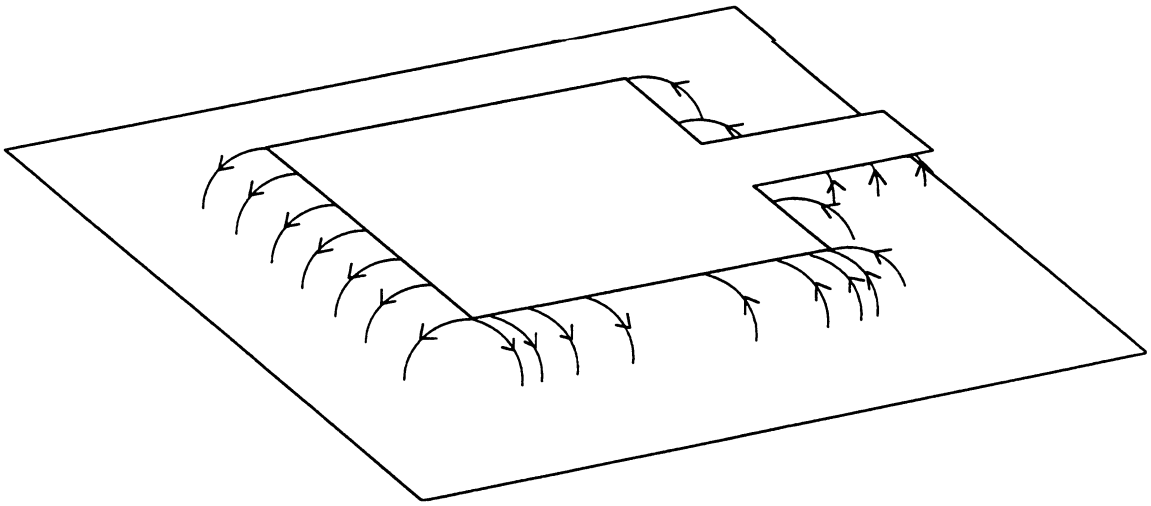

Figure 4.19: Schematic of the electric fields around the edges of a patch antenna operating in the fundamental mode.

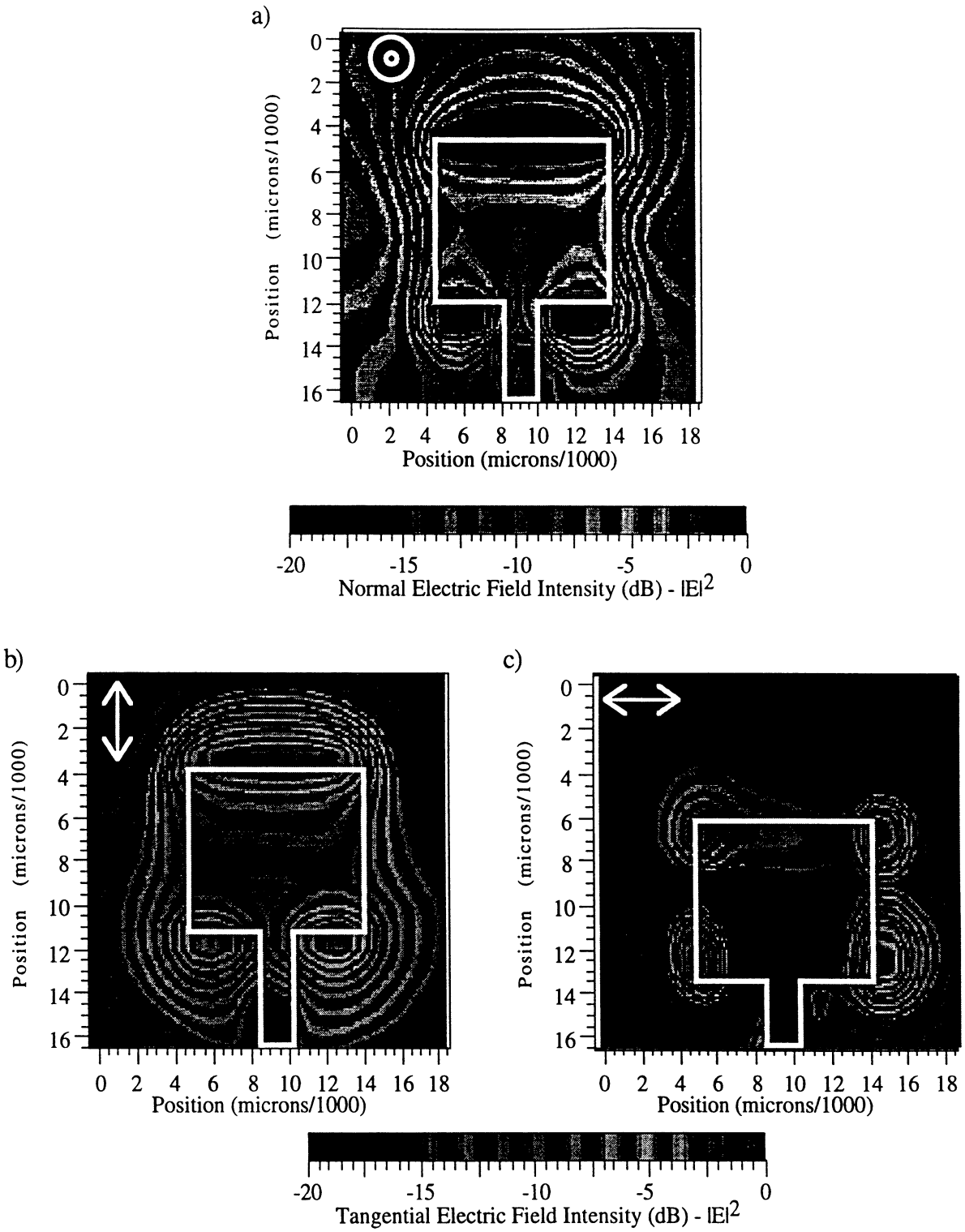

Figure 4.20: Measured electric field intensities above a patch antenna at 12.85 GHz. A 200 μm long hybrid monopole and a 250 μm long hybrid dipole were used to measure the a) normal b) tangential (vertical) and c) tangential (horizontal) electric field intensities.

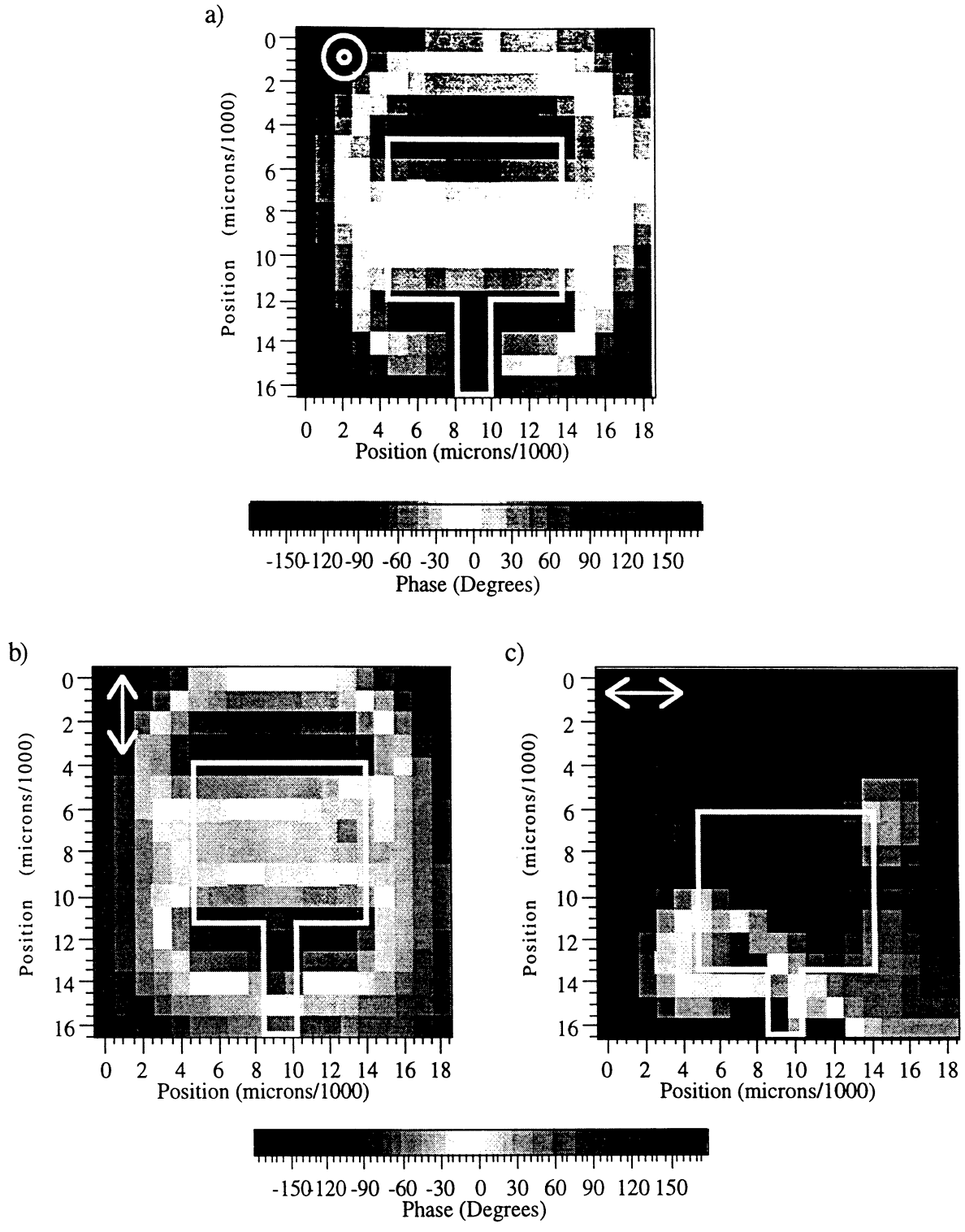

Figure 4.21: Measured round trip electrical phase delay of the a) normal electric field, b) tangential (vertical) electric field and c) tangential (horizontal) electric field.

radiating characteristics of this type of antenna. As predicted from the electric field schematic, the radiating edges of the patch have the strongest electric field components in the normal (a) and tangential (vertical) (b) directions. The nonradiating electric field component in the horizontal direction (c) has a much lower intensity than the vertical electric field component (b) and has nulls at the center of each edge of the patch antenna. Another interesting feature is that the fields are very strong in the substrate beyond the edge of the patch antenna in (a) and (b). By using the modulated scattering system, the near electric fields of planar antennas may be mapped at any distance away from the surface. Figure 4.21 displays the round trip electrical phase delay from the input port to the probe's position above the patch antenna at 12.85 GHz. As expected, the normal field phase delay (a) and the tangential (vertical) field phase delay are constant across the radiating edges of the patch antenna and the nonradiating tangential (horizontal) field phase delay is 180° out of phase with respect to each corner of the patch antenna.

4.6 Conclusions

In this chapter, the utility of the modulated scattering technique is demonstrated by measuring the electric field intensity and phase over microstrip line, coplanar waveguide, microstrip meander line, microstrip coupled line directional coupler and a microstrip patch antenna. The transmission line measurements verify that the system is capable of measuring electric fields as well as propagation constants and the locations of local minima and maxima at a specific frequency of operation. The tests over the microstrip meander line display how the modulated scattering technique can be used in conjunction with standard network analyzer measurements to aid in the understanding of rejection effects that may not have been anticipated in the initial design stages of a particular micostrip meander line. The microstrip coupled line directional coupler tests display the capability of the

modulated scattering technique to directly measure coupling coefficients. Finally, the measurements from the microstrip patch antenna display how the radiating characteristics of this and other planar antennas can be determined from measurements of the electric field intensity and phase.

CHAPTER V

AN EXPERIMENTAL AND THEORETICAL COMPARISON OF THE ELECTRIC FIELDS ABOVE A COUPLED LINE BANDPASS FILTER

5.1 Introduction

An experimental and theoretical comparison of the tangential electric fields within the range of 20 μm to 100 μm above a three stage coupled line bandpass filter (8.0 GHz-10.5 GHz) is presented. Using the experimental technique of modulated scattering, complete electric field intensity images of the normal and tangential electric field components are displayed and compared with the calculated electric fields obtained through the finite difference time domain (FDTD) method in both the passband (10 GHz) and the rejection band of the filter (12 GHz).

5.2 Three Stage Coupled Line Bandpass Filter

Figure 5.1 displays the geometry of a three stage coupled line filter fabricated on Rogers Corporation RT/Duroid® (ε_r=10.8, h=635 μm). The layout of the microstrip lines are moved from their optimal positions so that they would be aligned with a grid that would facilitate computer simulations of the filter. The bandpass filter has a measured insertion loss of 2.0 dB in the passband from 8.0 GHz to 10.5 GHz and provides better than -25 dB rejection at 12 GHz. Figure 5.2 displays the measured and FDTD calculated S-parameters of this filter. The S-parameters show that good agreement is achieved between measurements and FDTD calculations. The calculated and measured transmis-

sion coefficient match very well down to -40 dB, but the reflection coefficients deviate from each other in the passband. This deviation is most likely due to imperfect SMA to microstrip transitions at the input and output of the filter beyond 10 GHz.

5.3 Application of the FDTD Method

For a theoretical analysis of the coupled line filter, the FDTD method [48] is employed. The first step is to define a problem space of reasonable dimensions for computation. For this case, the space increments of the Yee's mesh are chosen to be 52.9 μm for the vertical direction, 100 μm for the propagation direction and 25 μm for the direction normal to propagation. The time step is chosen to be 73 fsec to satisfy the Courant stability criterion [32].

These choices result in a structure with 140x234x448 cells. The first-order Mur's absorbing boundary condition [49] is applied to the boundaries of the problem space with superabsorbers [50] at the input and output planes.

For wideband S-parameter extraction, a Gaussian pulse of 100 psec is used as the source microstrip excitation. Two simulations of pulse propagation along the microstrip line are made: one simulation for the filter and a second simulation for a 50 Ω microstrip through-line. For the filter simulation, the sum of the incident and reflected waveforms is calculated and for the through-line, the incident waveform is calculated. The reflected waveform at the input port is found by subtracting the incident waveform of the throughline from the total waveform of the filter. The reflection coefficient, S_{11}, is given by the ratio of the Fourier transforms of the reflected and the incident waveforms. The transmission coefficient, S_{21}, is given by the ratio of the Fourier transforms of the transmitted

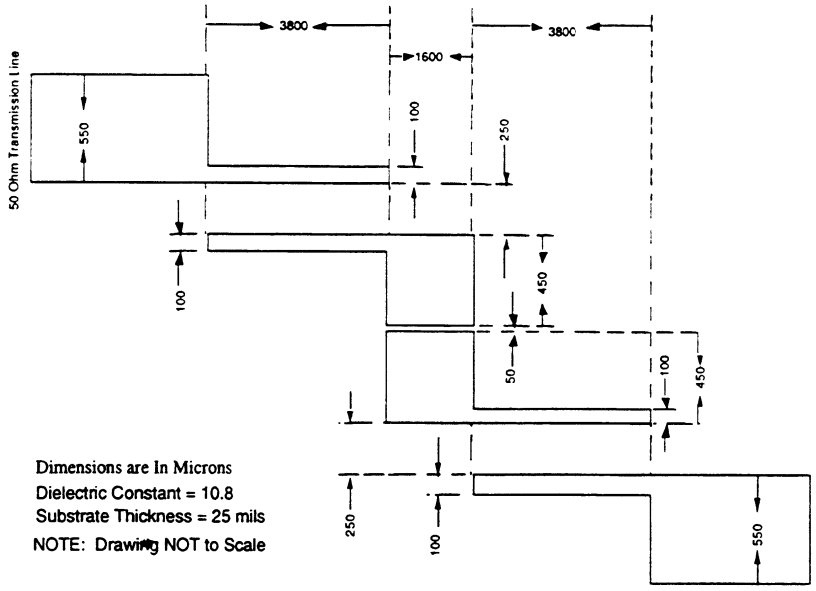

Figure 5.1: The geometry of the three stage coupled line bandpass filter used in this study.

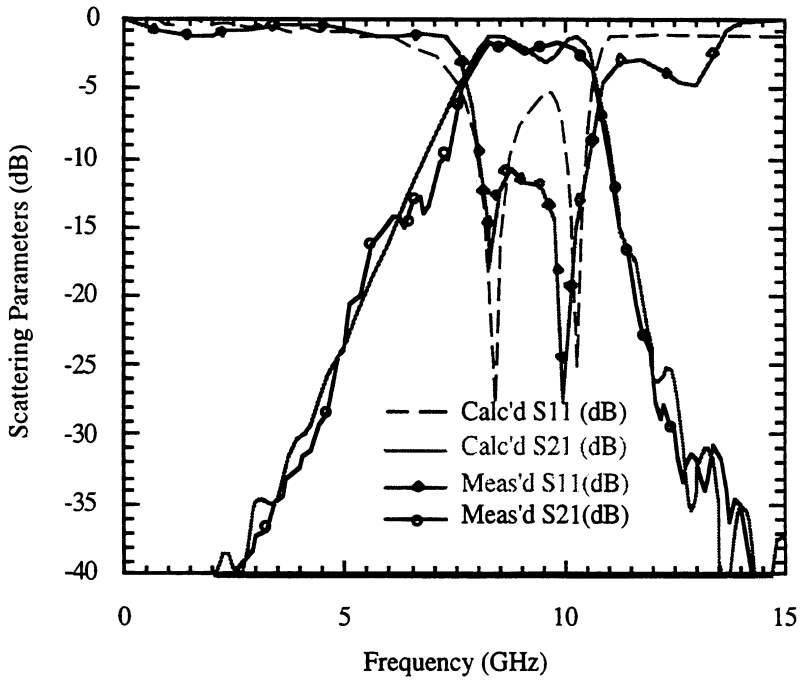

Figure 5.2: The measured and calculated (FDTD) scattering parameters for the three stage coupled line bandpass filter. The passband is from 8.0 GHz to 10.5 GHz with an insertion loss of 2.0 dB.

and the incident waveforms. The waveforms are probed at distances far enough from the filter discontinuities to eliminate the effects of evanescent waves [32].

For the electric field calculation, sinusoidal waves of 10 GHz for the passband and 12 GHz for the rejection band calculations are used as microstrip excitations. The excitations are vertical and are matched to the feedline (total impedance of the source region equal to the characteristic impedance of the feedline - 50 Ω). The source is applied 5 meshes inside the feedline in the propagation direction and the values of the electric fields are calculated during the 6th period of the sinusoidal waveform, to avoid the transition-period effect [32].

5.4 Measurements

Figure 5.3 displays tangential electric field intensity images obtained from modulated scattering measurements (fig. 5.3a.) and FDTD calculations (fig. 5.3b) in the passband at 10 GHz. A 250 μm long hybrid dipole probe is scanned across an area of 12750 μm by 3750 μm over the filter with the dipole oriented in the propagation direction. Over this very large scan area, the height of the probe above the filter varies from 50 μm to 100 μm due to bowing of the substrate and alignment errors. From studies of the decay of the electric field intensity with height, the error introduced by a height misalignment of 50 μm within this range can be at most 3 dB in electric field intensity. Tighter alignment is possible with planar semiconductor substrates and with tests over smaller areas.

The calculated electric field intensities presented in figures 5.3b and 5.4b are smoothed over a 400 μm by 200 μm area centered around the dipole where the smaller dimension is in the direction of the dipole arms. It was empirically determined that the

250 μm long hybrid dipole coupled to this area by comparing results from different smoothing operations over larger and smaller areas. This spatial averaging is the expected response for a dipole of finite length and finite height above the filter. Later tests with integrated probes showed that little spatial averaging was necessary and that the electric field data nearly matched the true electric field at a height of 100 μm above the coupled line filter.

In figures 5.3a) and 5.3b) the input and output levels of the electric field intensity around the microstrip feed lines are both -10 dB of the peak tangential electric field intensity within the filter. Both figures also predict a tangential electric field null halfway along each stage of the coupled line filter and display null regions of the tangential electric field within the substrate. The calculated electric field image predicts some small side peaks at the input, output and at the center which were not seen in the modulated scattering measurements. One possibility for this discrepancy may be due to the effects of metal loss and finite metal thickness which were not taken into account in the theoretical model and the 250 μm long dipole spatially averages the electric field over the scanned region. This would tend to reduce the peaks and spread them over areas where there is weak coupling.

Figures 5.4a) and 5.4b) display the electric field intensities over the same region but in the rejection band of the filter at 12 GHz (S_{21}=-25 dB). The electric field maps have similar features but differ mainly for two reasons. Because the FDTD calculations do not include the effects of finite conductivity of the copper, we expect larger peaks in the calculated electric field image than with the measured image. Also, because the modulated scattered signal must travel from the point of interest back to the input port, there is an additional loss of the RF signal for points nearer the output port when compared with points closer to the input port. Therefore, areas of the circuit furthest away from the input

port with the modulated scattering experiment will appear much less intense than areas closest to the input port. As mentioned earlier, the technique of modulated scattering fails to give an accurate measurement of the electric field when the losses in a circuit exceed 20 dB from the input port to the location of the probe.

The filter was also tested at 10 GHz with a 150 μm long integrated dipole probe aligned transverse to the direction of propagation. Figure 5.5 displays the tranverse tangential electric field intensity of the FDTD calculations (fig. 5.5a) and modulated scattering measurements (fig. 5.5b). The calculated field in this case was not spatially averaged over an area since the size of the dipole used is only three times the sample spacing. The measured electric field appears to have slightly broader peaks due to the dipole's finite size, but the measurements accurately reproduce the calculated electric field map. One feature that the measurements show that the calculations do not predict is an asymmetric tangential field distribution along a cross section of the input and output microstrip. This unexpected effect at 10 GHz does not appear in the tangential electric field measurement at 9 GHz (figure 5.7), at 11 GHz (figure 5.13) or at 12 GHz (figure 5.16) and therefore is definitely a real effect of the circuit.

To demonstrate the effectiveness of the modulated scattering technique, the normal, transverse tangential and longitudinal tangential electric field intensities of the coupled line bandpass filter were measured at 9 GHz, 10 GHz, 11 GHz and 12 GHz. These electric field intensity maps are displayed in figures 5.6 through 5.17 and are self normalized to the peak value of each plot. The normal electric fields were measured with a 100 μm long integrated monopole and the tangential electric fields were measured with a 150 μm long integrated dipole. The spacing of the monopole measurements was 75 μm per point in the transverse direction and 250 μm per point in the longitudinal direction.

(Note: Due to manual circuit mounting alignment error, the microstrip lines are not perfectly aligned with the probe's positioning axes. Thus, the superimposed filter layout is slightly rotated with respect to the probe's axes.) The spacing of the dipole measurements was 50 μm per point along the transverse axis and 250 μm per point along the longitudinal axis for the transverse electric field. The spacing of the dipole measurements was 100 μm per point along the transverse axis and 500 μm per point along the longitudinal axis for the longitudinal electric field. All of the electric field maps are plotted to the same scale so that the distances correspond truly to each other from measurement to measurement.

One important comparison to be made is between the transverse and normal electric field intensity maps. In a transverse cross section, the peaks in the normal electric field intensity maps occur in the same locations as the nulls in the transverse electric field intensity maps. In the normal electric field intensity map at 9 GHz (figure 5.6), the input and output microstrip lines have peak normal electric field intensities in the center of the microstrip line; however, the transverse electric field intensity map at 9 GHz (figure 5.7) shows nulls in the center of the microstrip line at the same locations. Similar comparisons can be made with the electric fields within the coupled line filter at this frequency as well as at other frequencies.

Figure 5.18 a)-d) displays the same transverse tangential electric field intensity measurements as in figures 5.7, 5.10, 5.13 and 5.16 but displays without a banded gray-scale legend. The figure demonstrates the potential for viewing the electric maps of a circuit in the frequency domain on a frame by frame basis.

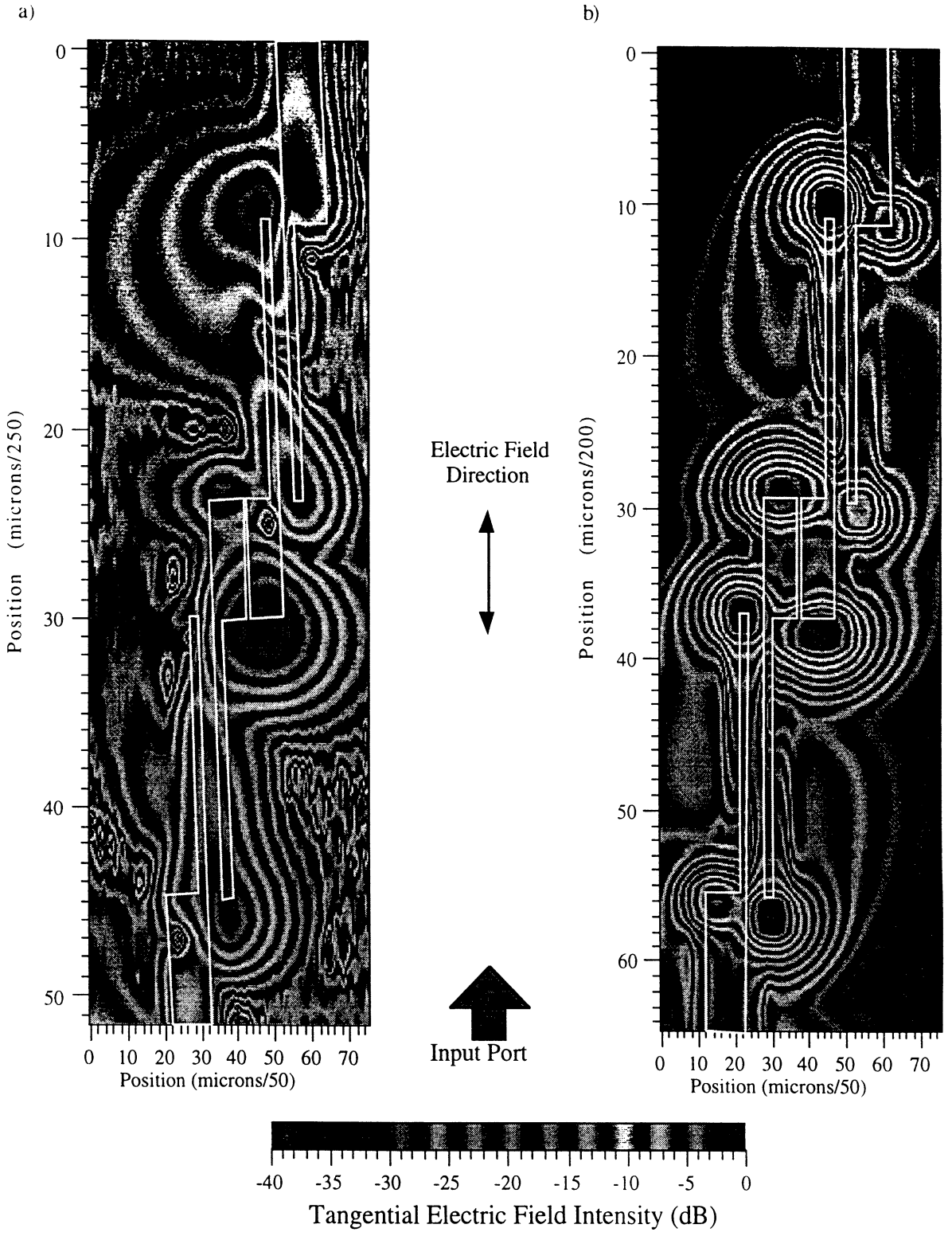

Figure 5.3: Tangential electric field intensity ($|E|^2$) images above a three stage coupled line filter in the passband at 10 GHz (S_{21} = -2 dB) along the longitudinal direction. a) Experimentally measured with a 250 μm hybrid dipole probe using the modulated scattering technique and b) theoretically calculated with the FDTD technique.

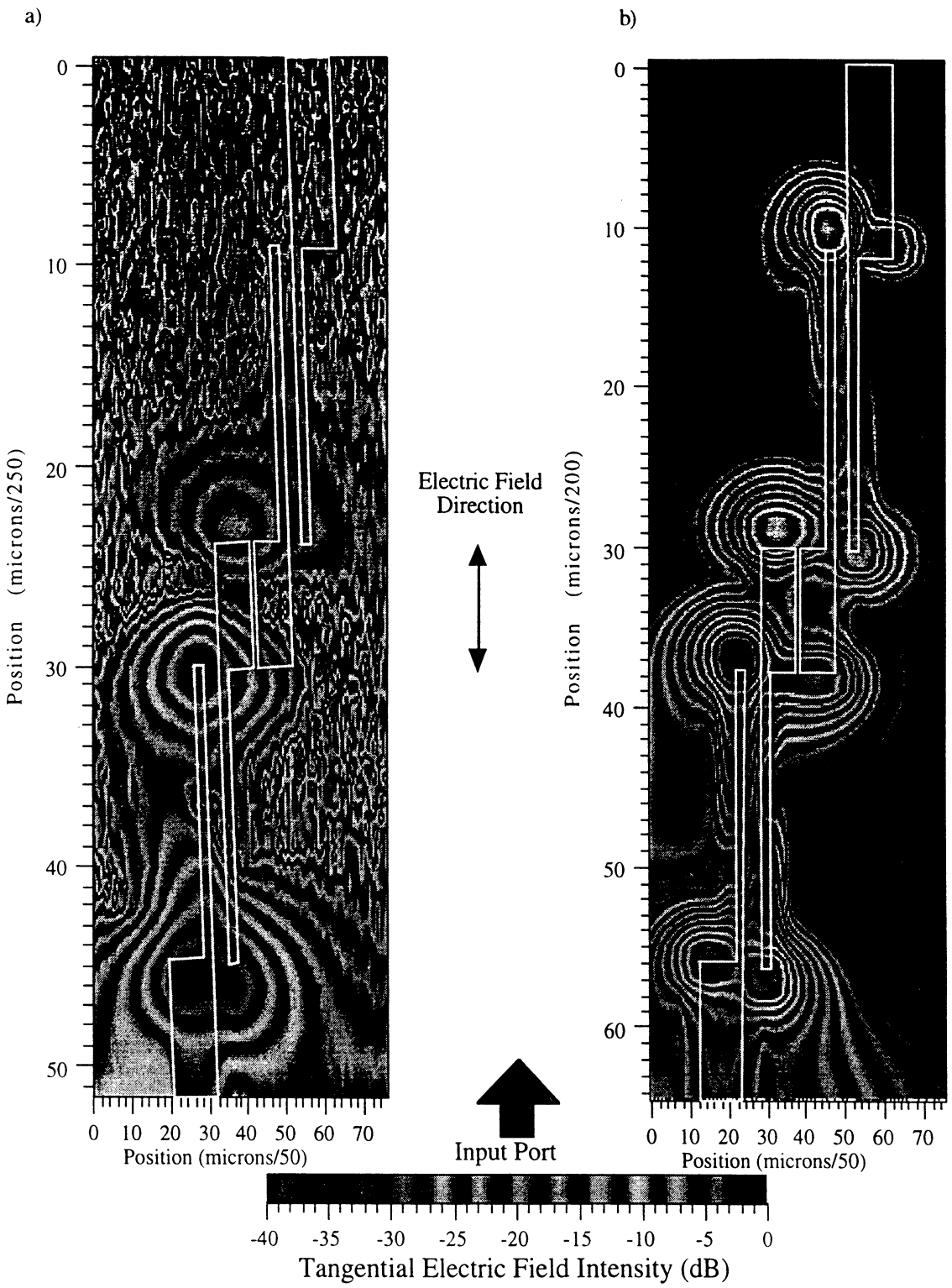

Figure 5.4: Tangential electric field intensity ($|E|^2$) images above a three stage coupled line filter in the rejection band at 12 GHz (S_{21} = -25 dB) along the longitudinal direction. a) Experimentally measured with modulated scattering and b) theoretically calculated with the FDTD technique.

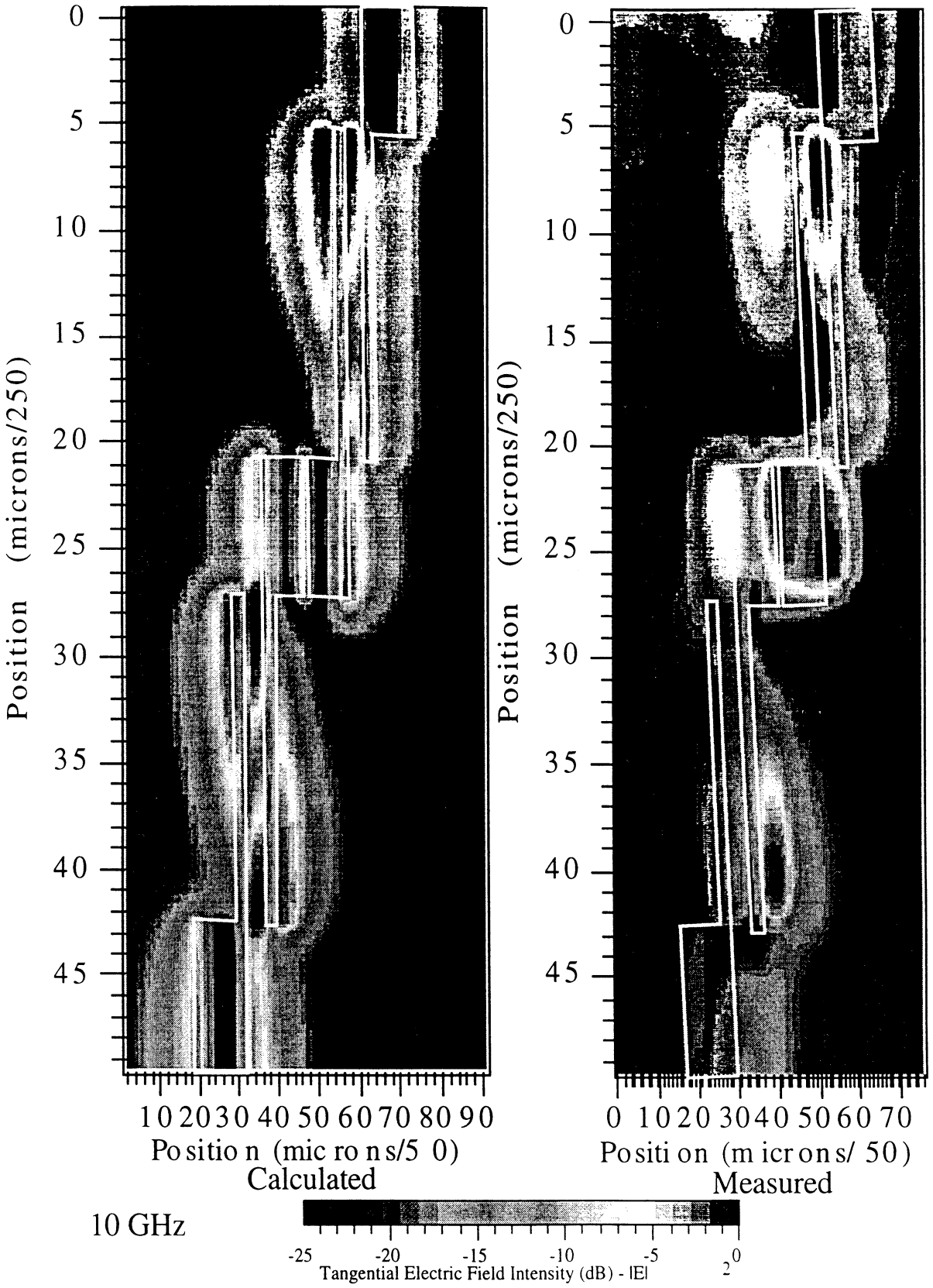

Figure 5.5: Measured tangential electric field intensity ($|E|^2$) in the transverse direction above a three stage coupled line filter in the passband at 10 GHz (S_{21} = -2 dB) with a 150 μm long integrated dipole b) compared with the FDTD calculated electric field intensity a).

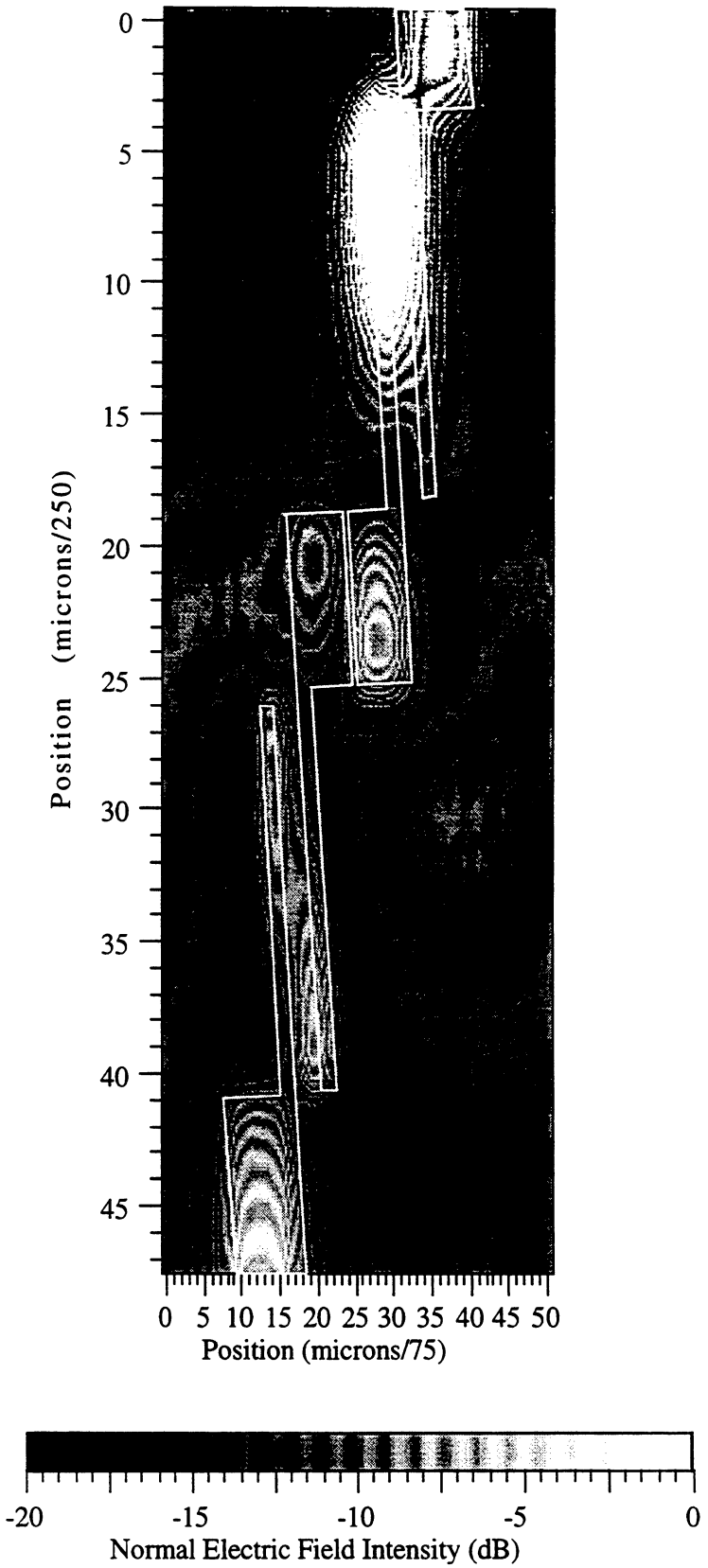

Figure 5.6: Measured normal electric field intensity ($|E|^2$) at 9 GHz (S_{21} = -2 dB) with a 100 μm long integrated monopole.

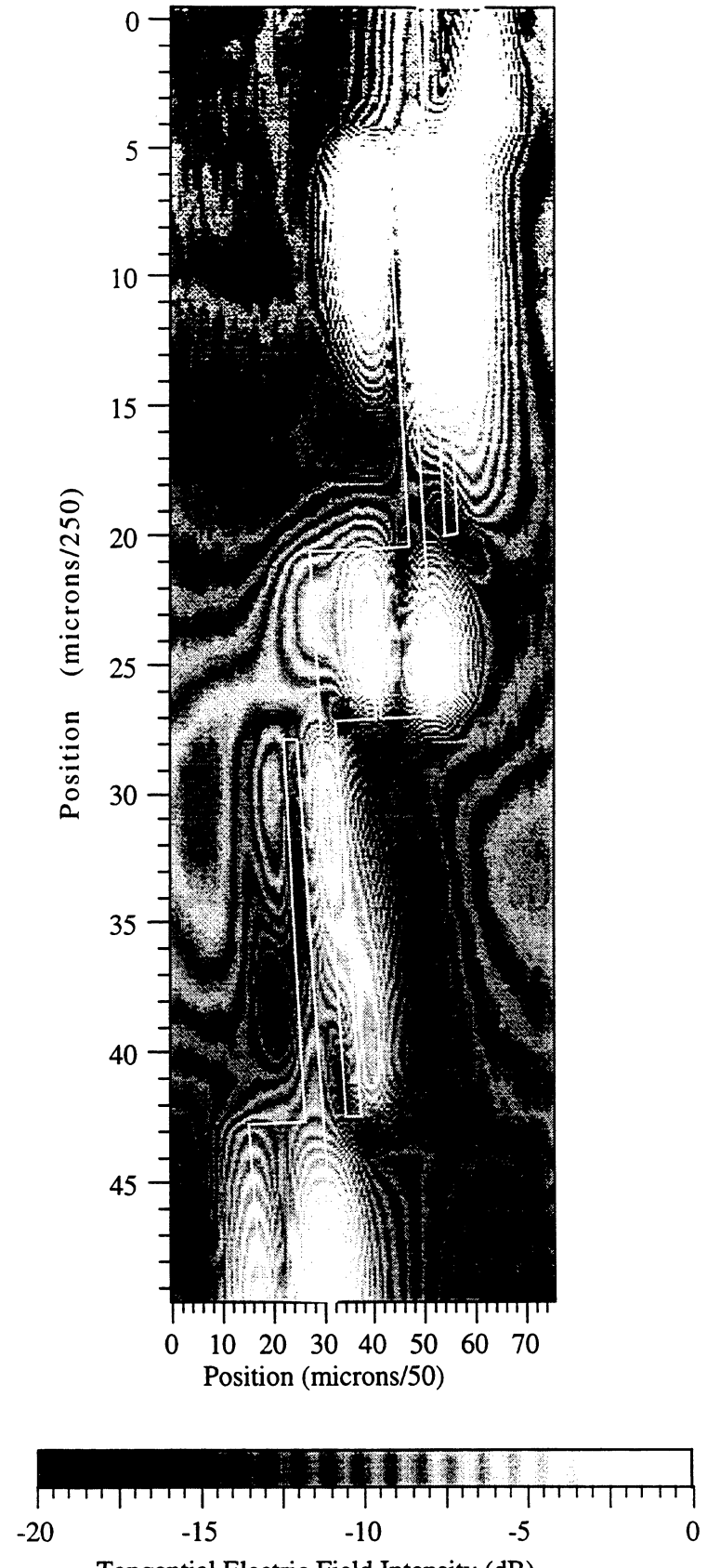

Figure 5.7: Measured tangential electric field intensity ($|E|^2$) in the transverse direction at 9 GHz (S_{21} = -2 dB) with a 150 μm long integrated dipole.

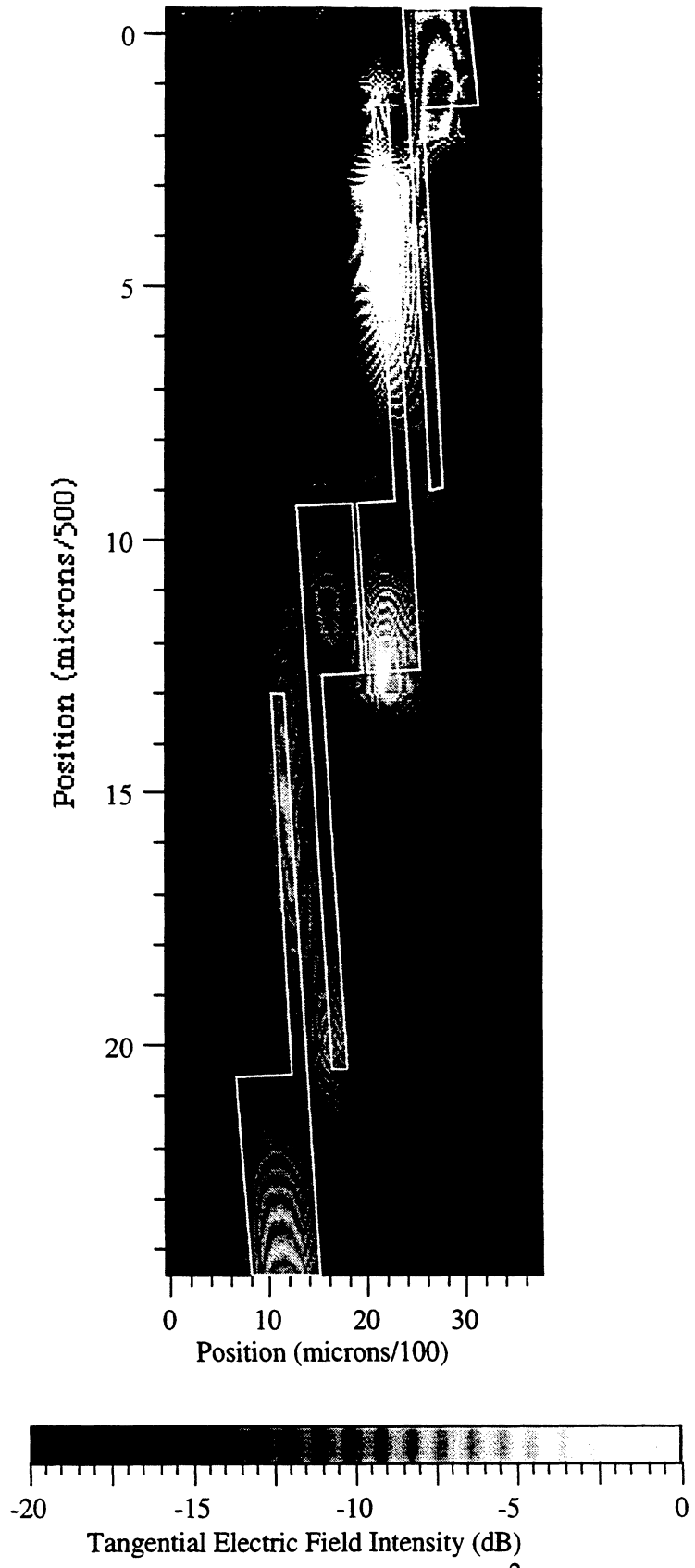

Figure 5.8: Measured tangential electric field intensity ($|E|^2$) in the longitudinal direction at 9 GHz (S_{21} = -2 dB) measured with a 150 μm long integrated dipole.

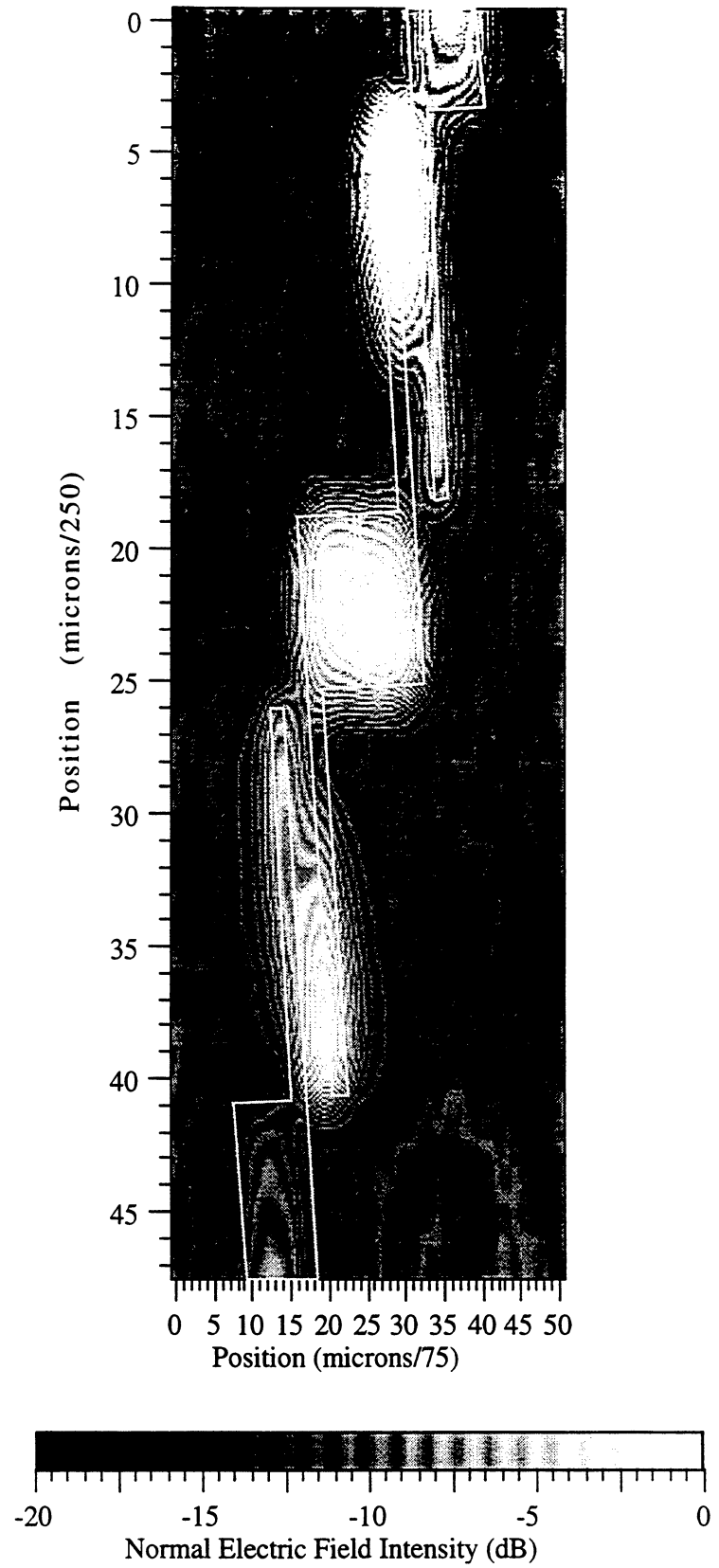

Figure 5.9: Measured normal electric field intensity ($|E|^2$) at 10 GHz (S_{21} = -2 dB) measured with a 100 μm long integrated monopole.

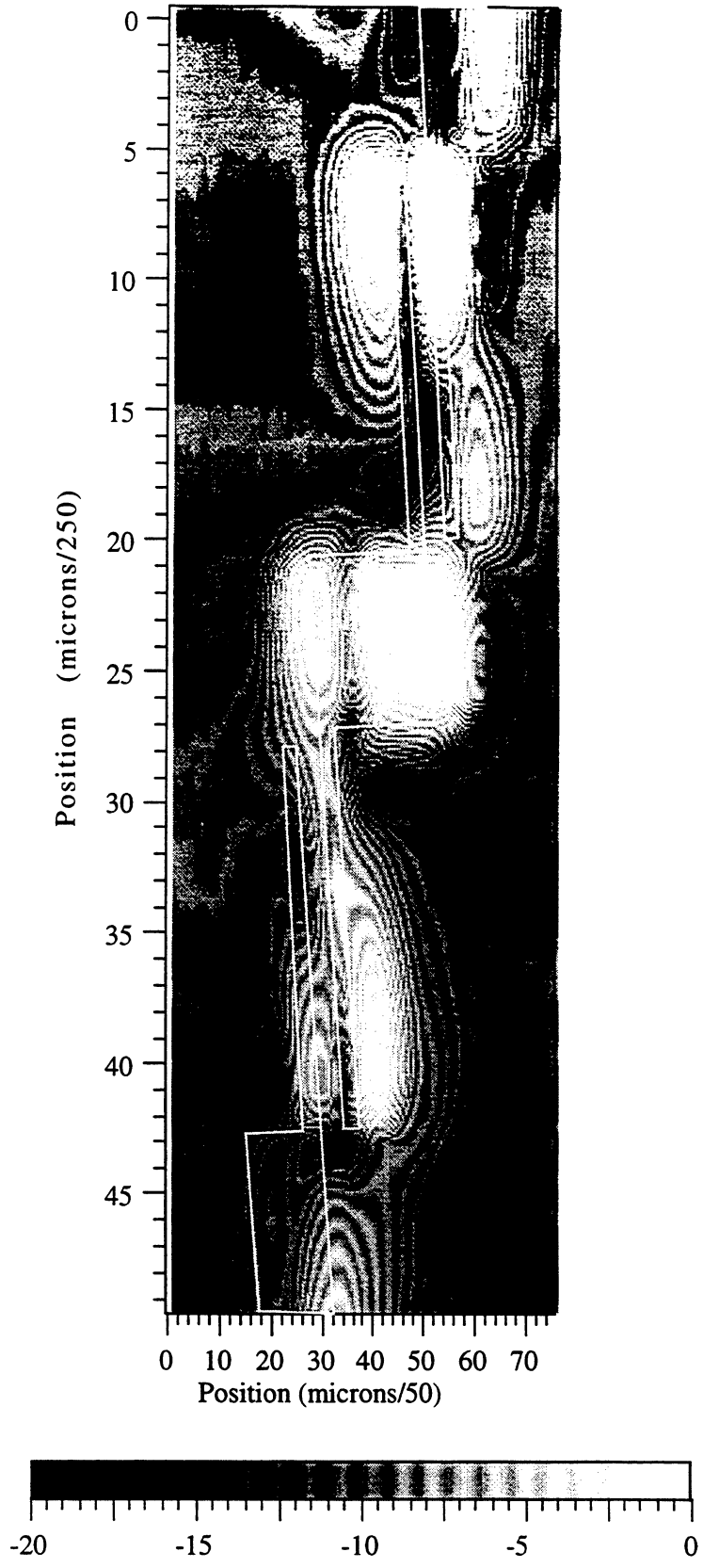

Figure 5.10: Measured tangential electric field intensity ($|E|^2$) in the transverse direction at 10 GHz (S_{21} = -2 dB) measured with a 150 μm long integrated dipole.

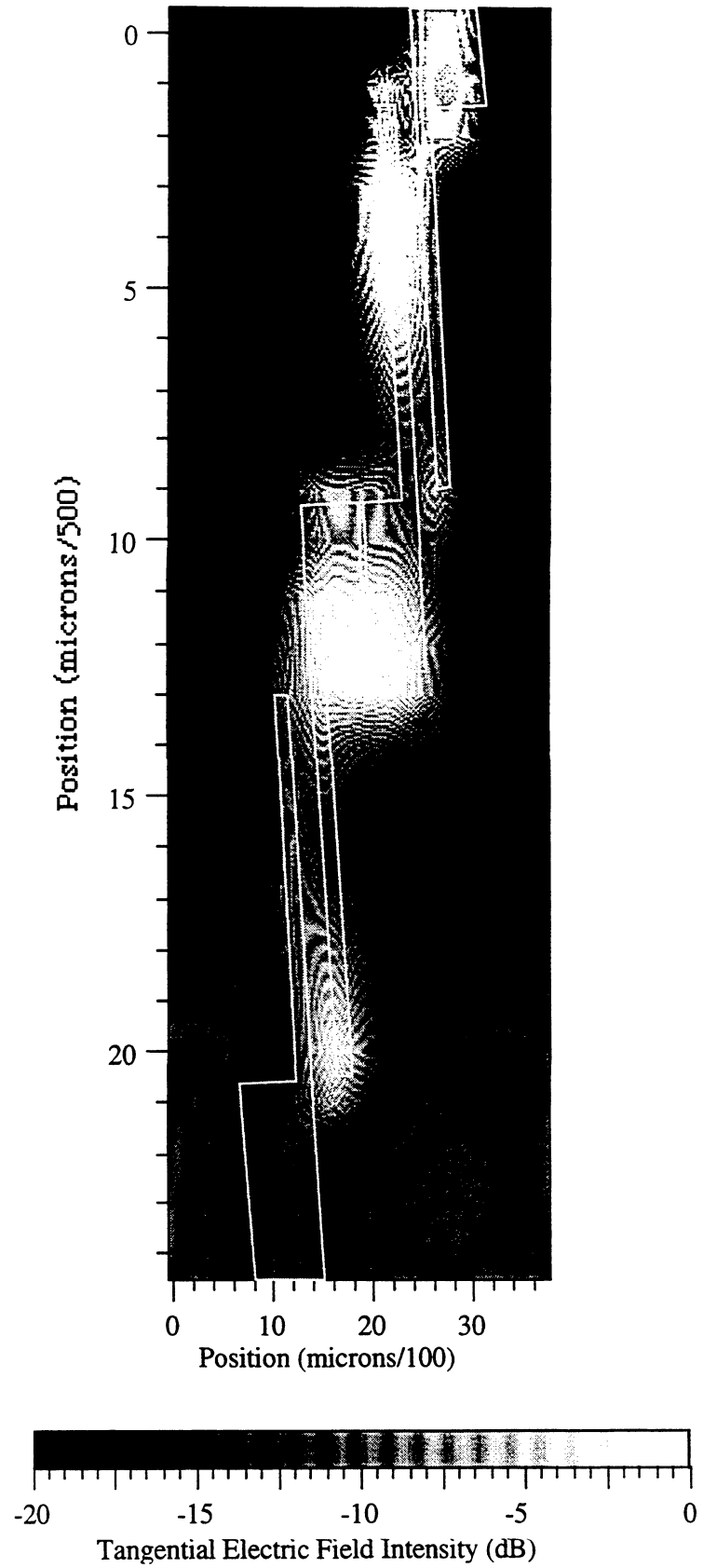

Figure 5.11: Measured tangential electric field intensity ($|E|^2$) in the longitudinal direction at 10 GHz (S_{21} = -2 dB) measured with a 150 μm long integrated dipole.

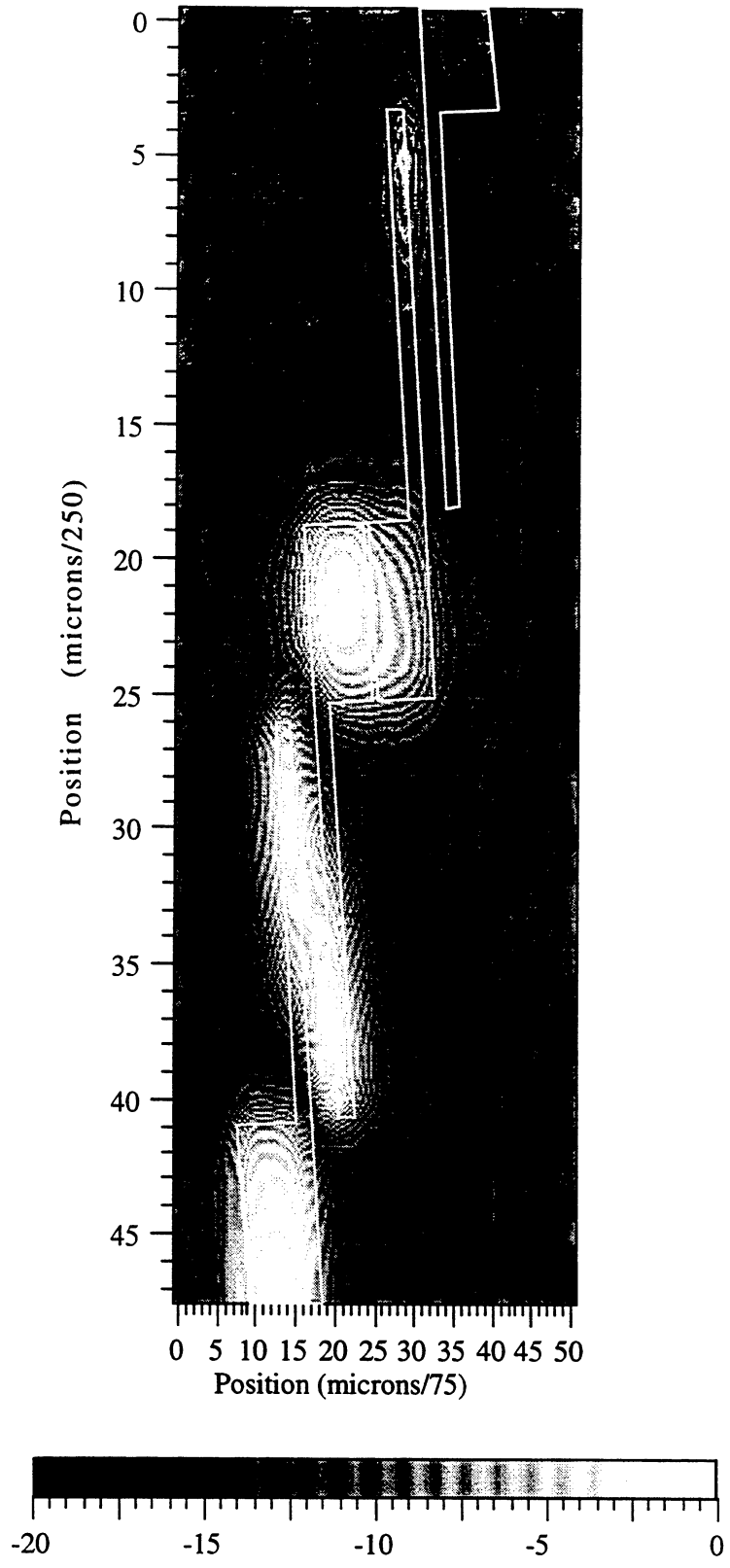

Figure 5.12: Measured normal electric field intensity ($|E|^2$) at 11 GHz (S_{21} = -9 dB) measured with a 100 μm long integrated monopole.

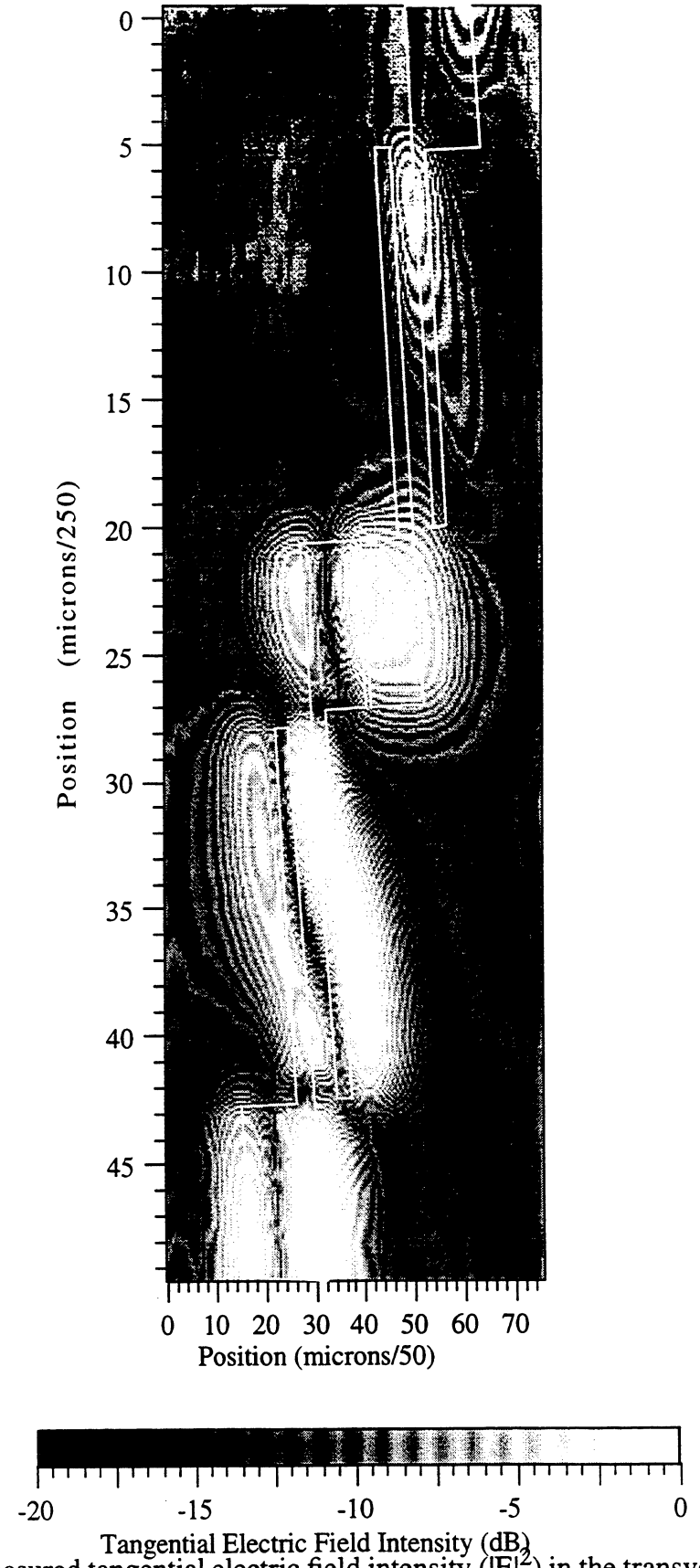

Figure 5.13: Measured tangential electric field intensity ($|E|^2$) in the transverse direction at 11 GHz (S_{21} = -9 dB) measured with a 150 μm long integrated dipole.

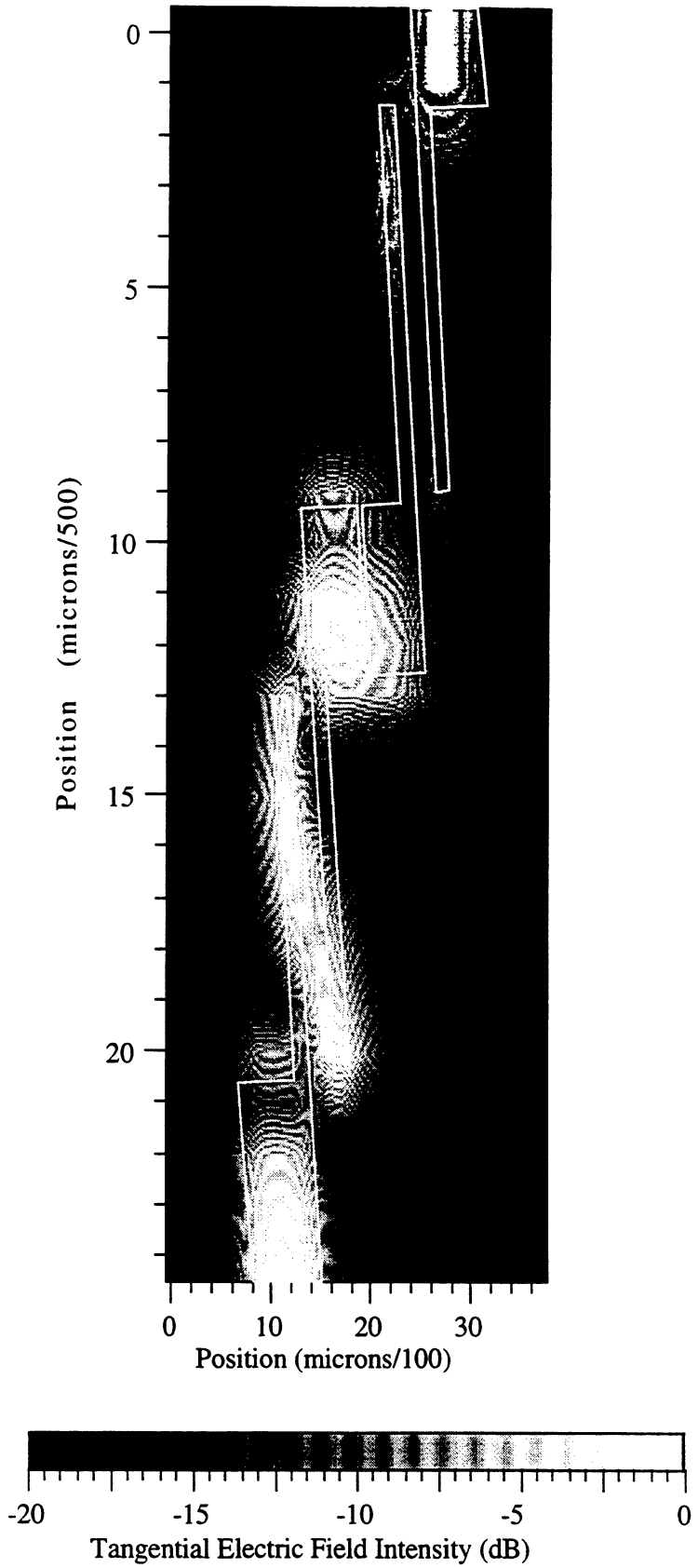

Figure 5.14: Measured tangential electric field intensity ($|E|^2$) in the longitudinal direction at 11 GHz (S_{21} = -9 dB) measured with a 150 μm long integrated dipole.

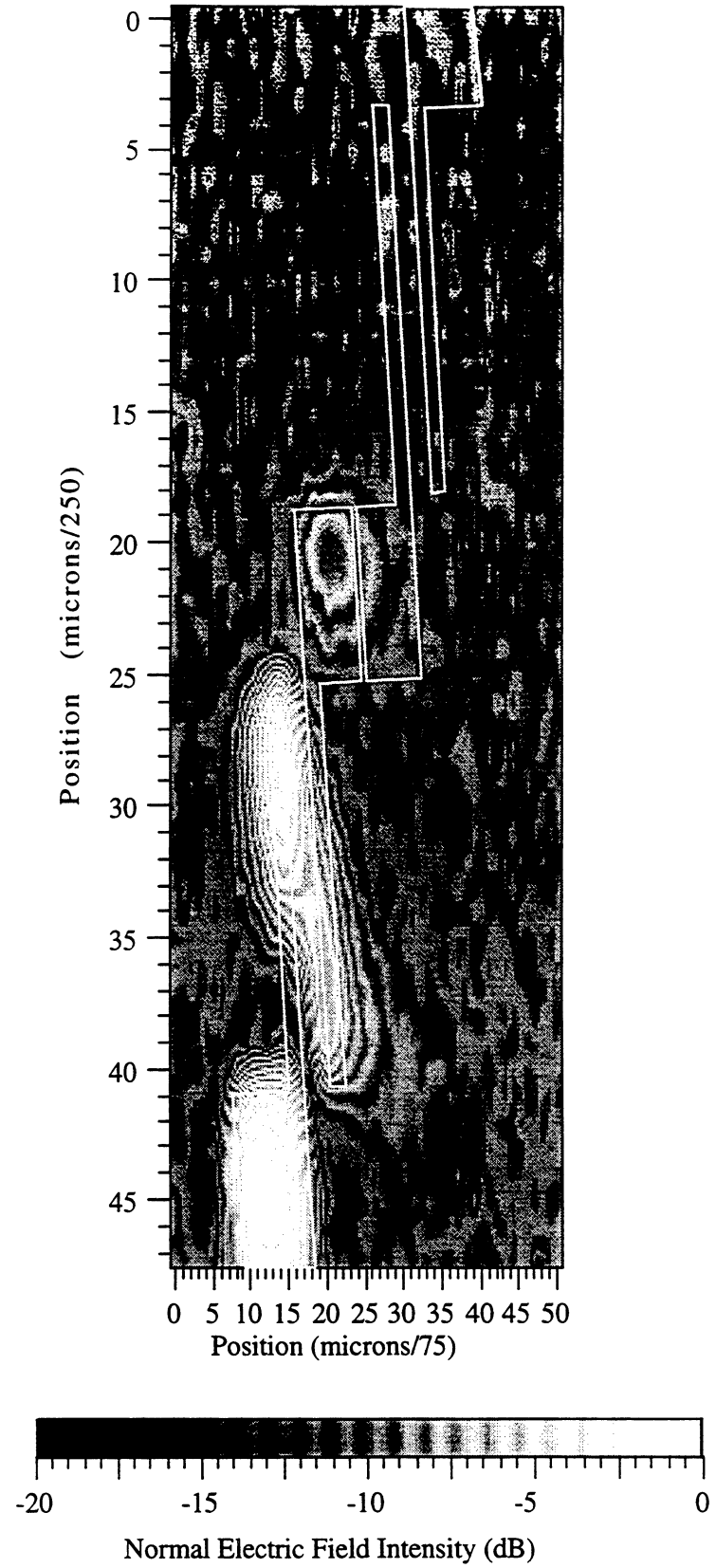

Figure 5.15: Measured normal electric field intensity ($|E|^2$) at 12 GHz (S_{21} = -25 dB) measured with a 100 μm long integrated monopole.

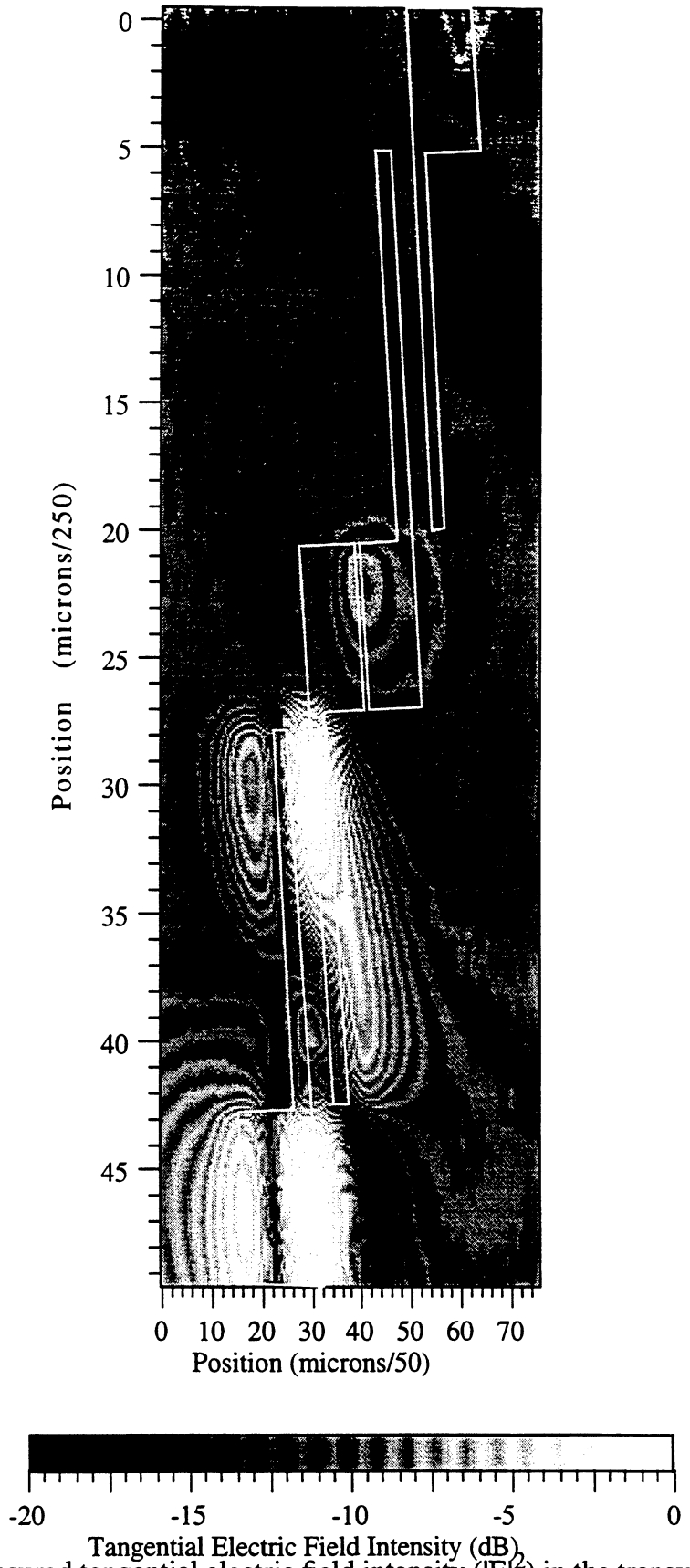

Figure 5.16: Measured tangential electric field intensity ($|E|^2$) in the transverse direction at 12 GHz (S_{21} = -25 dB) measured with a 150 μm long integrated dipole.

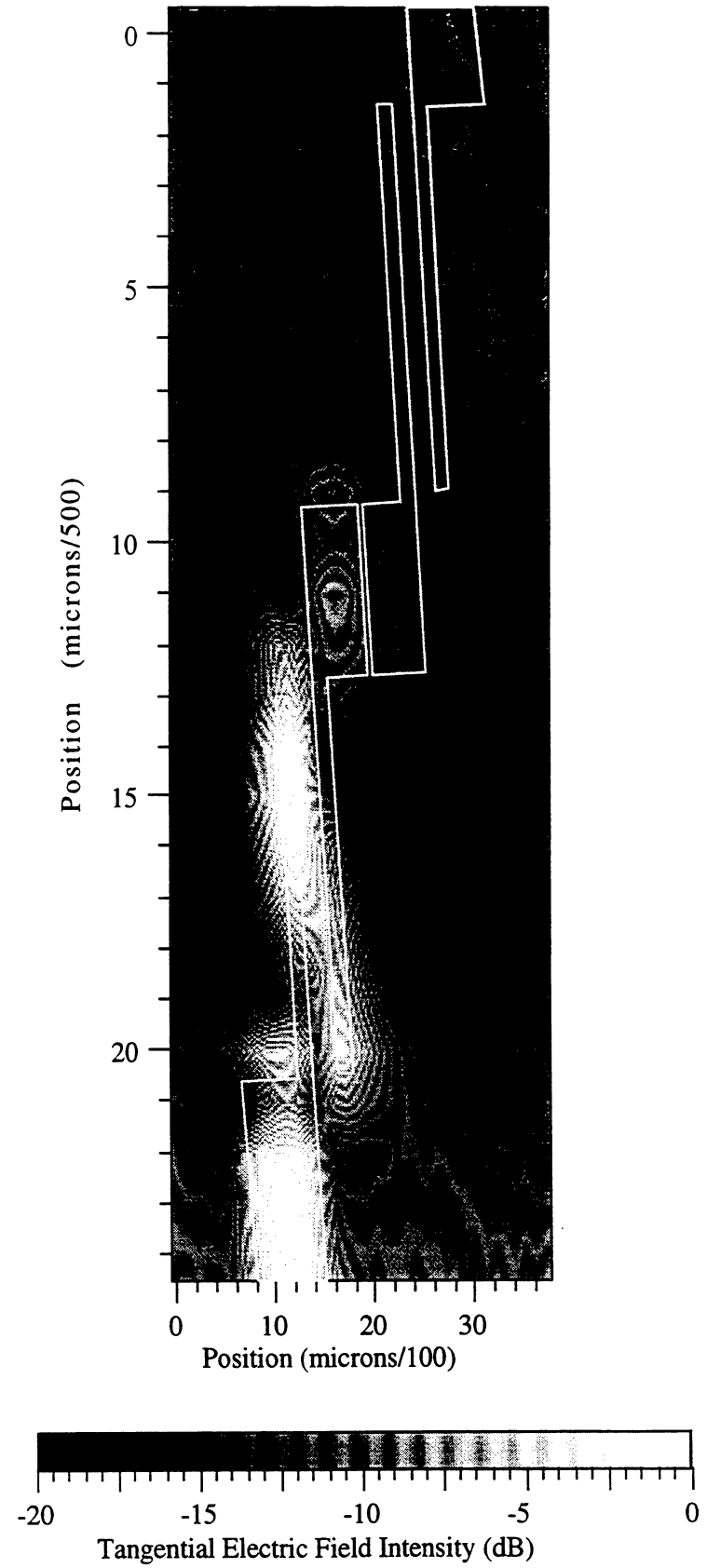

Figure 5.17: Measured tangential electric field intensity ($|E|^2$) in the longitudinal direction at 12 GHz (S_{21} = -25 dB) measured with a 150 μm long integrated dipole.

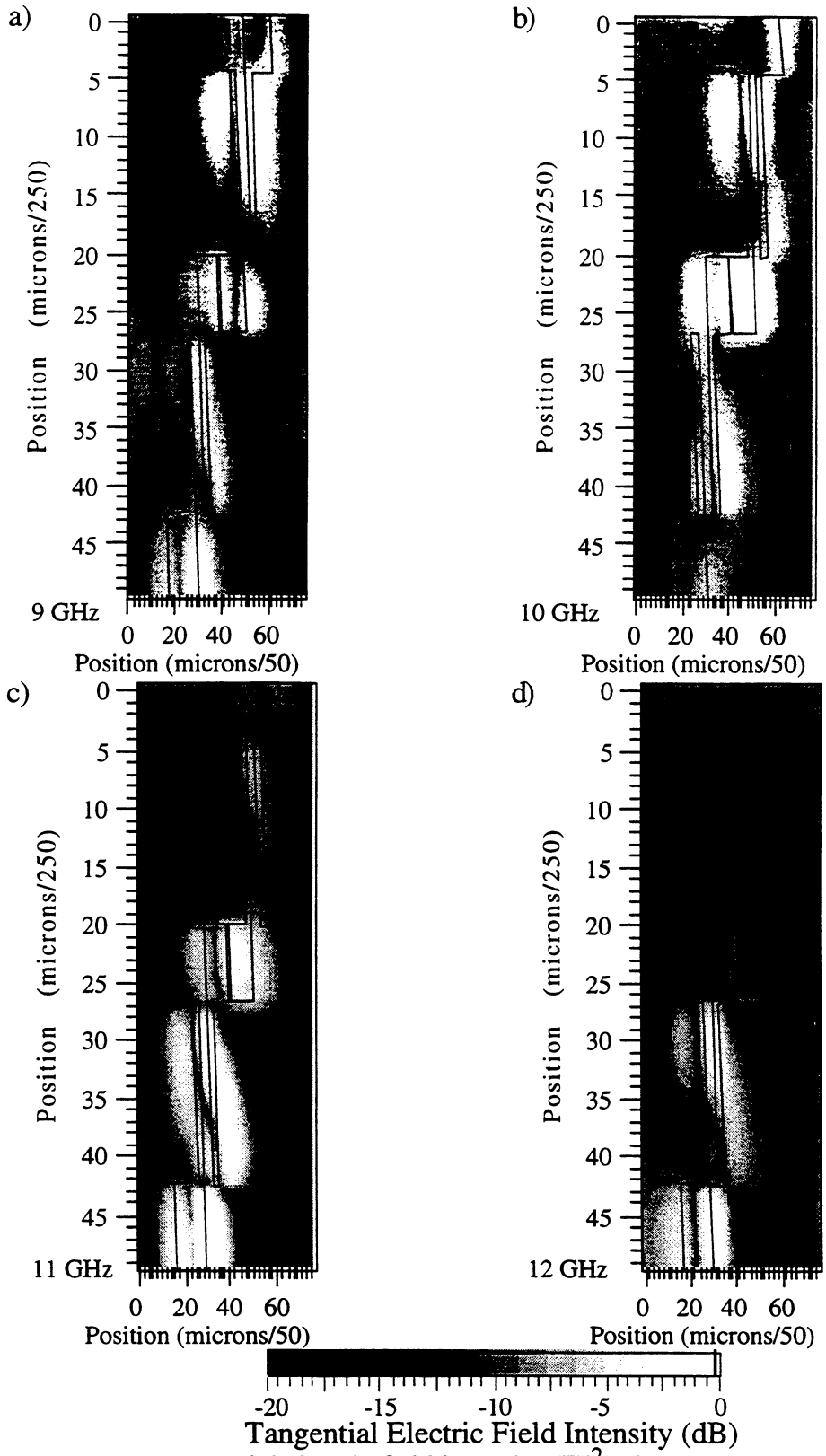

Figure 5.18: Measured tangential electric field intensity ($|E|^2$) along the horizontal axis measured with a 150 μm long dipole with an integrated Schottky diode. Images are at a) 9 GHz, b) 10 GHz, c) 11 GHz and d) 12 GHz.

5.5 Conclusions

In this chapter an experimental and theoretical comparison of the operation of a three stage coupled line bandpass filter has been presented. First, the use of the FDTD method is verified by observing good agreement between the calculated S-parameters and the measured S-parameters of the filter. Next, the normal and tangential electric field intensities obtained from the two methods at 10 GHz and at 12 GHz are compared. Integrated probes (a 100 μm monopole and a 150 μm dipole) are used to present complete electric field maps (normal and tangential) at 9 GHz, 10 GHz, 11 GHz and 12 GHz. Peak electric field locations, relative intensity values and evanescent fields can be detected with both methods, thus making the modulated scattering and FDTD techniques valuable tools for the study of the operation of microwave circuits.

CHAPTER VI

CONCLUSIONS AND FUTURE WORK

Many different electric field imaging systems have been developed to further our understanding of the internal operation of microwave circuits. In the cases where a wide bandwidth time domain waveform of the electric fields is necessary, electro-optic sampling is the most appropriate technique to be employed. In the cases where an electric field map over a microwave circuit operating at a single frequency is desired, the modulated scattering method should be used. Most of these systems are presently in the research stages of development and significant reductions in cost, improvements in speed of acquisition and further understanding of the results must take place before the electro-optic sampling technique or the modulated scattering technique gain widespread acceptance in the microwave engineering community.

In this thesis an experimental electric field imaging system that uses the method of modulated scattering is presented. The system improves upon the techniques used by Richmond [26] in that the system is completely coaxial. The experimental system presented follows the method used by Zürcher [29], but by using circulators and a system of RF switches, the bandwidth of the system has been improved by a factor of twenty. Additional information about the operation of a microwave circuit can be obtained by measuring a modulated scattered signal from the output port of the DUT as well as from the input port.

By using standard semiconductor processing techniques to make integrated Schottky diodes with the scattering antennas, the size of the probes used in this research is more than fifty times smaller than the probes used by Zürcher [29]. The computer controlled system is at present capable of measuring the electric fields between 2 GHz and 18 GHz and is adaptable to planar circuit measurements as well as free space measurements. Two types of scattering probes (hybrid and integrated) that contain monopoles and/or dipole scatterers are presented. Some probes contained a monopole and a dipole on the same probe. This design allows simultaneous measurements of the normal and tangential electric fields of the DUT with a slight sacrifice in electric field mapping accuracy due to the potential coupling between the monopole and the dipole. More work needs to be performed to determine the "cross-talk" between a monopole and a dipole scatterer on the same probe. The modulated scattering system theory is presented and verified over microstrip transmission lines and coplanar waveguide. From these electric field measurements it is possible to determine the propagation constants, device to device coupling, losses, and the existence of substrate and evanescent modes.

This dissertation presents the first experimental results from an electric field mapping system that uses the technique of modulated scattering that has been applied to planar microwave circuits at frequencies above 2 GHz and below 18 GHz. The electric field map results have been displayed in various formats in an attempt to emphasize the important features and regions of each microwave circuit. Since this research project was started in 1992, the system has been continuously improved. Even though initial tests with hybrid probes yielded electric field intensity dynamic ranges of 10 dB, the results are instructive, aid in the understanding of the modulated scattering technique and have been included in this dissertation. More recent tests with integrated probes provide finer electric field resolution and improved software yields intensity dynamic ranges of better than 30 dB. Future

efforts will apply the technique toward higher operating frequencies and work on improving the sensitivity, dynamic range and spatial resolution of the current system.

The speed at which the electric field imaging system collects an electric field map can also be improved by multiplexing an array of probes that is scanned in one direction instead of scanning a single probe in two directions. It is anticipated that an electric field scanning system will gain widespread acceptance if it can be used simultaneously with a probe station during standard network analyzer tests. Currently an electric field intensity map of 600 points takes one hour for a single frequency with 30 dB dynamic range and a 300 msec integration time. This speed of acquisition needs to be reduced before the technique becomes more than a research and development tool.

The basic theory of modulated scattering demonstrates that the measured voltage is proportional to the square of the electric field amplitude. The measured voltage also depends on the RF path loss from the DUT to the quadrature mixer and the quadrature mixer conversion loss. Many issues need to be resolved to remove this loss factor from the measurements to obtain the true electric field amplitude at each frequency. Future work should attempt to perform a frequency calibration of the system.

Further improvements need also to be made with the phase measurements of the system. The ultimate goal would be to produce the true electric field phases at each position for each electric field component. The phase results presented in this dissertation are round trip electric phase delays (for the input port) and have not been converted to the true electric field phase due to the difficulty involved in this type of conversion for complex circuits. Over simple transmission lines operating in a quasi-TEM mode, the phase delays along the transmission line can simply be divided by a factor of two to receive the true electric field phase. On circuits where higher order modes exist (eg. the bandpass filter),

this type of conversion is impractical because the higher order modes will have different propagation constants. Although the results are not presented in this dissertation, several tests were performed by measuring the scattered signal from the output port of a microstrip circuit. In this case, contours of constant phase were measured as predicted by the theory developed for modulated scattering. This additional phase information from the output port may later help derive the true electric field phase at a specific location.

Many future applications for the research presented in this dissertation exist for nonreciprocal devices such as amplifiers, digital phase shifters, mixers, etc... as well as for quasi-optical testing of complex radiating circuits such as log periodic and spiral antennas. Knowledge of the electric fields over these circuits will allow for the placement of more circuitry within the same area and will speed the circuit debug-time during the developmental stages of the microwave circuit design process. More work needs to be performed on experimentally determined design rules that can be developed and checked with the results from electromagnetic simulation packages.

Overall, the most important benefit of the modulated scattering technique is the system's adaptability to test a wide variety of circuits and systems independent of the supporting substrate. The system is modular and is very easily changed to test new circuits of interest. Any probe configuration is possible as long as the probe contains a modulating element. Although loop antennas are not developed in this work, they could be studied in the future. Higher frequency RF components can be used to extend the operation of the modulated scattering system up to 60 GHz for a coaxially based system while using the same scattering probes (provided the modulating element on the probe works up to this frequency). The RF system developed here can be used for testing the near electric fields around passive circuits, active circuits and horn antennas. Depending on the device that is

tested, the motors may need to cover a larger area and could also be changed to fit the application. The emphasis of this work has been to map the electric fields over microwave circuits with the finest resolution possible. The smallest probes used in this work are a 100 μm long monopole and a 150 μm long dipole. With these probes, the measurement limits of the electric field have not yet been reached. It is still possible to make smaller probes in closer proximity to a microwave circuit and achieve higher spatial electric field resolution.

APPENDICES

APPENDIX A

Note: The following research project is not directly related to the electric field imaging systems that have been presented earlier in this dissertation. The project described in Appendix A was the first project that I did at The University of Michigan and is placed in this appendix for completeness.

A 75 GHz TO 115 GHz QUASI-OPTICAL AMPLIFIER

A.1 Abstract

A wideband quasi-optical amplifier employing two pyramidal back-to-back horns has been developed. Using a four-stage W-band low noise amplifier (LNA) designed and fabricated by Martin Marietta Laboratories [51], the quasi-optical amplifier gives a system gain greater than 11 dB from 86 GHz to 113 GHz without any low frequency oscillations. A peak system gain of 15.5 dB is measured at 102 GHz, and the measured noise figure of the system is 7.4 dB at 94 GHz. The quasi-optical amplifier design maintains the same polarization of the received and transmitted signal, provides better than -40 dB isolation and can be fabricated monolithically at millimeter-wave frequencies.

A.2 Introduction

Recent advances in transistor technology at Martin Marietta Laboratories have led to the development of a four-stage W-band low noise amplifier (LNA) using pseudomorphic InGaAs Modulation-Doped Field Effect Transistors (MODFET's). These amplifiers have demonstrated gains up to 23 dB in a waveguide environment [51]. The amplifiers typically employ a waveguide-to-microstrip or waveguide-to-coplanar waveguide transition [51], and the waveguide fixture is expensive to build at frequencies higher than 100 GHz. For array applications it is advantageous to incorporate these amplifiers directly within a radiating structure that can be fabricated monolithically. This approach has been pursued at lower frequencies by Kim et al. [52] and Chi et al. [53]. In both techniques, the quasi-optical amplifiers employ polarization diplexing along with a differential amplifier stage. In this paper, a new quasi-optical amplifier design based on the integrated horn structure [54] is presented. There is no need for tuning polarizers and therefore this design allows a wide operating bandwidth. The design maintains the same polarization and is compatible with high gain monolithic millimeter wave amplifiers. It is possible to incorporate this design in an array on a wafer-scale level for quasi-optical power combining applications at millimeter wave frequencies.

A.3 Quasi-Optical Amplifier Design

The quasi-optical amplifier consists of two back-to-back pyramidal horns each with openings of $1.35\lambda_o$ x $1.35\lambda_o$ at the design frequency of 94 GHz. A 4.25 mm x 1.25 mm Martin Marietta Laboratories LNA chip is placed approximately $\lambda_o/2$ above the apex of each pyramidal horn (Fig. A.1a). Two back-to-back pyramidal horns were fabricated by anisotropically etching <110> silicon wafers from opposite sides and stacking eight 385 μm-thick horn sections and one 200 μm cavity spacing section. The LNA is

hybrid mounted in the etched cavity connecting the two integrated horns (Fig. A.1b). The cavity is 3.0 mm wide by 200 μm high. The thickness of the LNA GaAs substrate is 100 μm. The sidewalls of the horns and the sides of the cavity were metallized with 0.7 μm of gold through angle evaporation.

The position of the chip within the horn cavity is chosen using a 3 GHz (equivalent to 94 GHz) microwave scale model for a probe of length 600 μm and width of 190 μm on a 100 μm thick GaAs substrate (at 94 GHz). An input match (S_{11}) better than -20 dB from 2.75 GHz to 3.25 GHz (equivalent to 86.5 GHz to 102 GHz) is measured with the probe facing the interior of the horn - the input horn (Fig. A.2a). An input match better than -10 dB is measured with the probe facing out of the horn - the output horn - over the same frequency range (Fig. A.2b). The probe radiates preferentially into the dielectric side, thereby resulting in a better match for the input horn.

The LNA is mounted on a silicon wafer containing the bias lines, bias resistors and bypass capacitors (Fig. A.3). The four gates were biased at 0.25 V. The drains were biased separately and optimized for maximum gain. The bias voltages for the drains, from input to output, were 4.5 V, 3.8 V, 3.5 V, and 3.5 V, respectively. The total source-to-drain current for all four MODFET's is 24 mA. The source is grounded on the back side of the LNA chip along the receiving horn sidewall using silver epoxy and 0.7 mil gold ribbon.

A.4 Measurements

Patterns taken from a 3 GHz microwave model show a very high cross-polarization level of both the input and output integrated horns (Fig. A.4). This is attributed to the short length and large width of the waveguide-to-CPW probe. Since the probe dimensions of the LNA were fixed, we were not able to decrease the cross-polarization level. We rec-

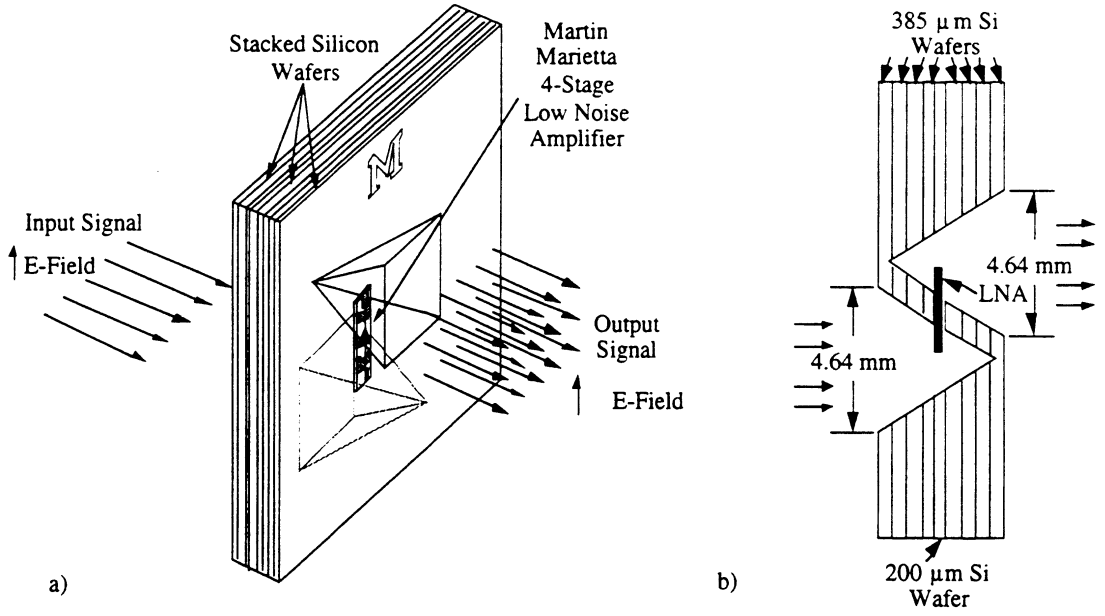

Figure A.1 Quasi-optical amplifier consisting of Martin Marietta Laboratories' low noise amplifier between two back-to-back pyramidal horns. A plane wave input signal is amplified and repeated on the opposite side with the same polarization. a) Isogonal view. b) Side view.

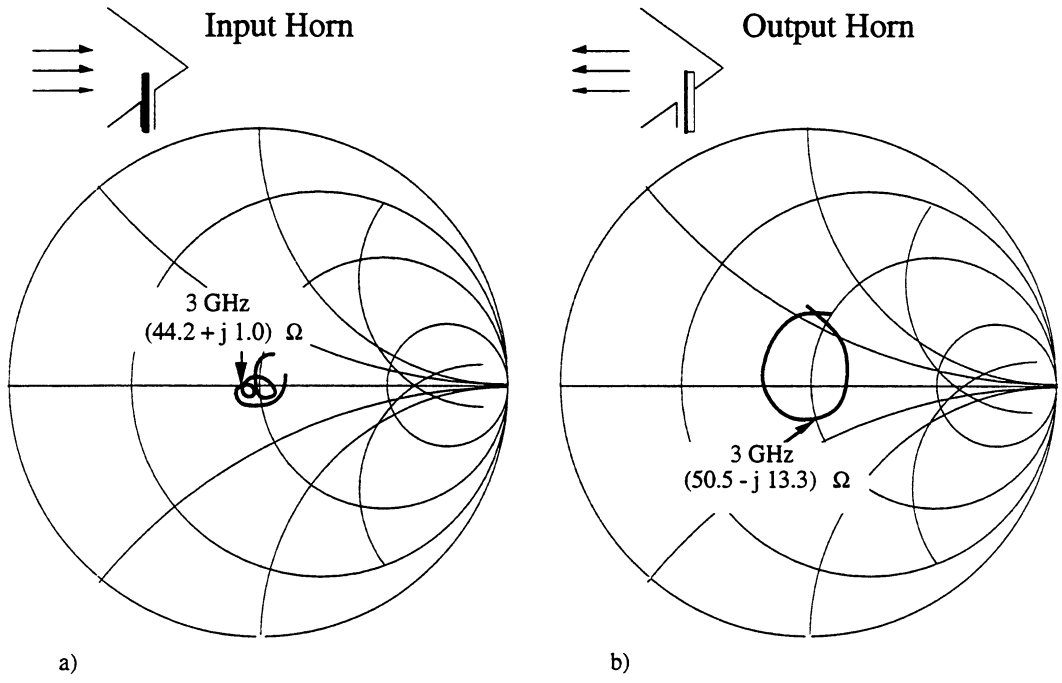

Figure A.2 Input impedance of a scaled monopole probe measured from 2.75 GHz to 3.25 GHz (equivalent to 86.5 GHz to 102 GHz) inside the a) input pyramidal horn and b) output pyramidal horn.

ommend that a longer narrower probe be used for future quasi-optical amplifier applicationswhich will result in reduced cross-polarization levels [56]. The short monopole probe also results in an asymmetry in the E-plane copolarization pattern. No pattern measurements were performed at other frequencies, but the same behavior is expected over the 2.75-3.25 GHz band (equivalent to 86.5 GHz to 102 GHz). Notice that the input pattern is better than the output pattern because the monopole probe radiates preferentially into the dielectric side of the substrate [57].

The gain of the quasi-optical amplifier structure is measured in a plane-wave experiment similar to [52]. First, the system is calibrated without the quasi-optical amplifier present. The power received during calibration, P_c, is determined from Frii's transmission formula:

$$P_c = \left(\frac{\lambda^2 G_t G_r}{(4\pi(2r))^2} \right) \tag{A-4}$$

where $2r$ is the distance between the transmitting and receiving horns, P_t is the transmitted power, G_t is the gain of the transmitting antenna (a WR-10 pyramidal horn), and G_r is the gain of the receiving antenna (a WR-10 pyramidal horn). Next, the power received, P_r, with the quasi-optical amplifier in place is given by:

$$P_r = P_t \left(\frac{G_t A_i^{eff}}{4\pi r^2} \right) G \left(\frac{G_r A_o^{eff}}{4\pi r^2} \right) \tag{A-5}$$

where G is the gain of the LNA, A_i^{eff} is the effective aperture area of the *input* horn, A_o^{eff} is the effective aperture area of the *output* horn and r is the distance between the transmitting/receiving horn and the quasi-optical amplifier. Since the effective aperture

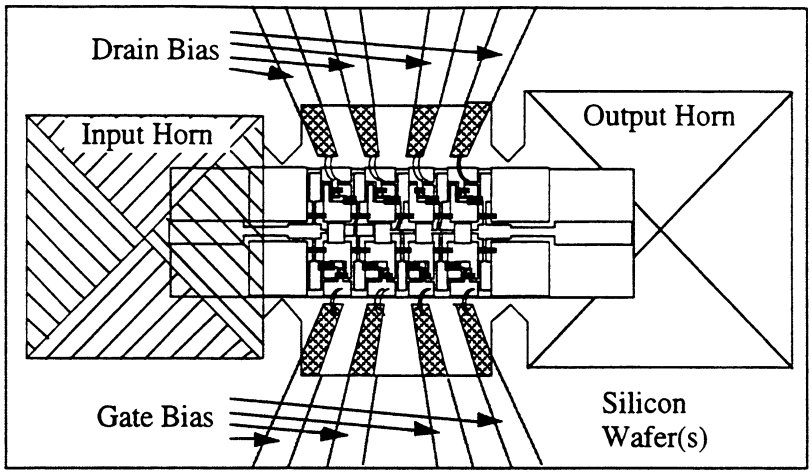

Figure A.3 Martin Marietta Laboratories' low noise amplifier (LNA) chip placed in a cavity between two horn openings. The LNA chip dimensions are 4.25 mm by 1.25 mm.

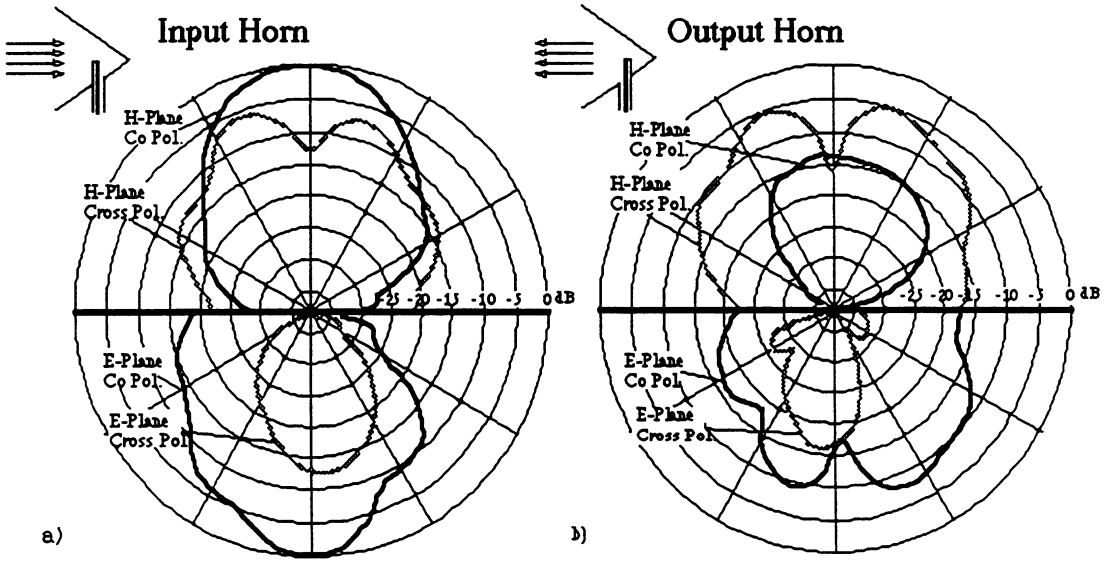

Figure A.4 Quasi-optical amplifier 3 GHz microwave model (equivalent to 94 GHz) antenna patterns. a) Antenna patterns with monopole facing the interior of the horn. b) Antenna patterns with monopole facing the exterior of the horn.

tures of the input and output integrated horns are not known accurately, the aperture efficiencies are separated from the physical area of the input and output integrated horns:

$$P_r = P_t\left(\frac{G_t\varepsilon_i^{eff}A_{phys}}{4\pi r^2}\right)G\left(\frac{G_r\varepsilon_o^{eff}A_{phys}}{4\pi r^2}\right) \tag{A-6}$$

where A_{phys} is the physical area of the input and output horns, ε_i^{eff} is the effective aperture efficiency of the *input* horn, and ε_o^{eff} is the effective aperture efficiency of the *output* horn. The gain of the quasi-optical system, G_{SYS}, is then found by dividing (A-4) by (A-6) and solving for $G\ \varepsilon_i^{eff}\ \varepsilon_o^{eff}$.

$$G_{SYS} = G\varepsilon_i^{eff}\varepsilon_o^{eff} = \left(\frac{P_r}{P_c}\right)\left(\frac{\lambda r}{2A_{phys}}\right)^2 \tag{A-7}$$

The system gain is measured over the frequency range of 75 GHz to 115 GHz. The gain of the quasi-optical amplifier,G_{SYS},, is greater than 11 dB from 85 GHz to 113 GHz and greater than 3 dB gain from 75 GHz to 115 GHz (Fig. A.5). No oscillations were found on the bias lines or in free space and the isolation is better than -40 dB when the bias is removed. The variations of the gain curve versus frequency are potentially due to the changes in the antenna pattern, cross-polarization level, input impedance, and reference power calibration. From microwave pattern modeling, we expect the co-polarized aperture efficiency of each horn to be below 60% at 94 GHz. Thus the lower limit of the gain of the amplifier chip itself would be at least 4 dB above the curve in Figure A.5. Although the exact gain of the LNA is not known, histograms of the gains of 44 different LNA's fabricated at the same time suggest a mean LNA gain of 16.3 dB around 90 GHz and a standard deviation of 3.2 dB. This value corresponds well with the measured system gains of 12.9 dB at 94 GHz and 15.5 dB at 102 GHz. If the effective aperture efficiencies

were deembedded from the gain calculation, the measured gain would increase by more than 4 dB to 16.9 dB at 94 GHz.

Figure A.6 displays the experiment for measuring the noise figure of the quasi-optical amplifier. The IF chain gain and input noise temperature is measured to be 97.0 dB and 55.3K, respectively, at 94 GHz. The conversion loss of the balanced mixer is measured to be 4.6 dB with a mixer input noise temperature of 821K. The loss of the teflon lens (f/D=0.85) is determined to be 0.30 dB. Next, we measure the noise figure of the quasi-optical amplifier to be 7.4 dB at 94 GHz using standard hot/cold load techniques. The absorber is placed very close to the input horn antenna to ensure that the whole input pattern is coupled to the hot/cold load. This value matches with an expected 7-8 dB noise figure from these specific LNA's. New LNA's from Martin Marietta Laboratories that have 23 dB gain and 4.3 dB noise figure [51] would greatly improve the performance of the quasi-optical amplifier.

A.5 Conclusions

In this paper we report a single element quasi-optical amplifier that is based on an integrated horn antenna using a LNA originally designed for operation within waveguide. Using the waveguide-to-CPW probe as the radiating element for the structure, a peak system gain of 15.5 dB at 102 GHz is measured and higher than 11 dB system gain is measured over a 27% bandwidth. The quasi-optical horn antenna can be designed to result in a much lower cross-polarization level using a long monopole probe and to couple efficiently to a Gaussian beam system using an integrated horn extension [54]. This quasi-optical amplifier maintains the same polarization of the incoming and outgoing signal. The absence of tuning polarizers allow a wider operating bandwidth for this design.

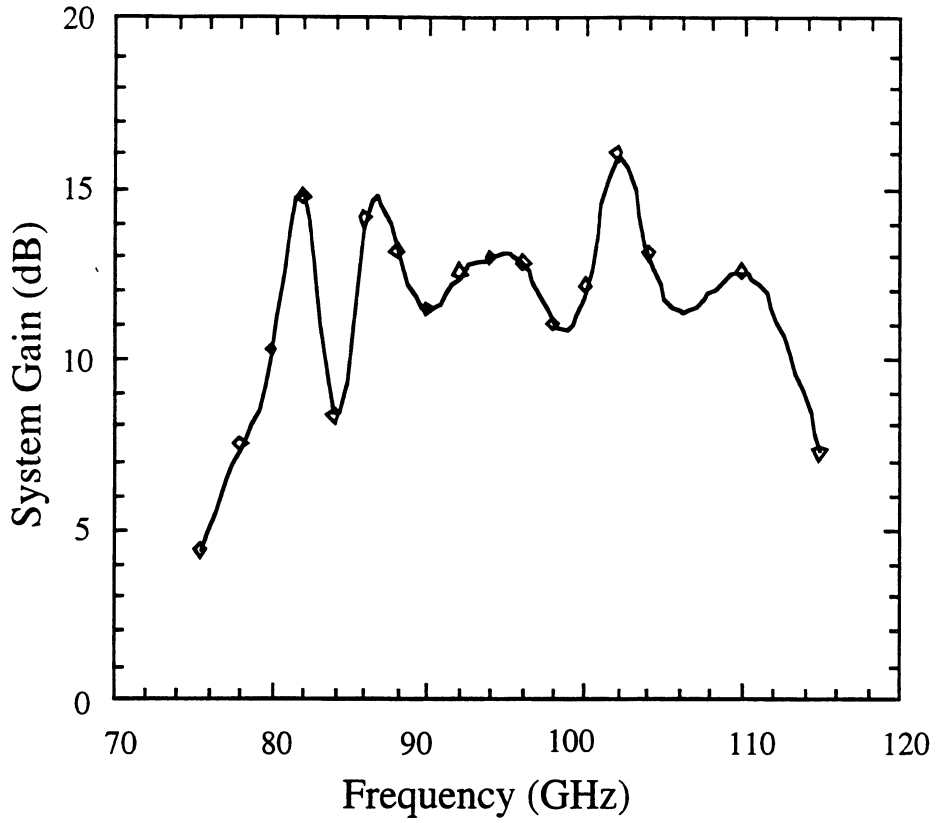

Figure A.5 Quasi-optical amplifier system gain versus frequency. The system gain includes loss due to input and output horn aperture efficiency (see text for more detail)

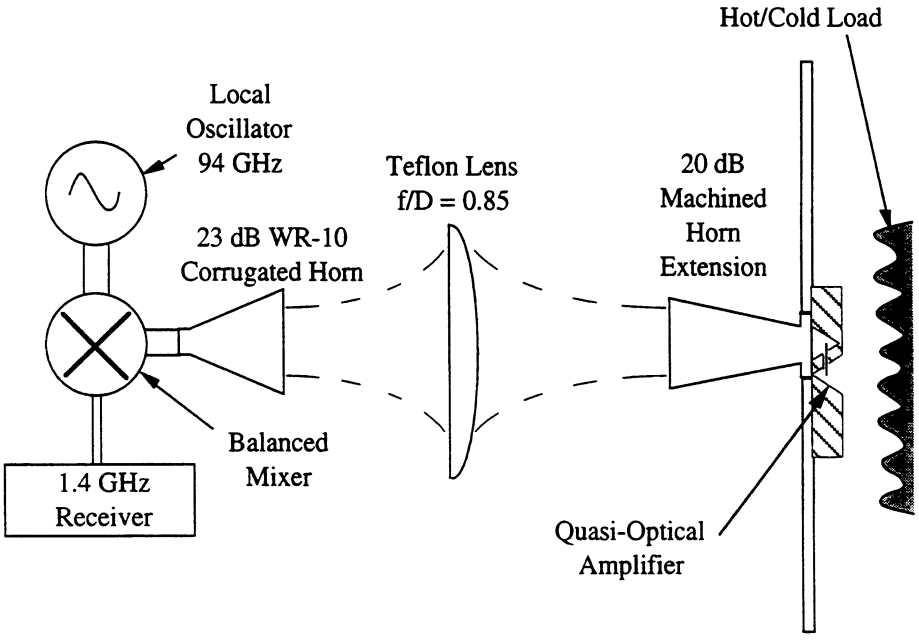

Figure A.6 Noise figure experiment using an LO frequency of 94 GHz and an IF of 1.4 GHz.

APPENDIX B

Probe Transmission Line Design

Appendix B contains the Mathematica input and output files that were used to design the feeding transmission lines to the probes that were fabricated on 125 micron thick quartz. The following design equations are from Wadell [43].

For two coplanar strips with the following geometry:

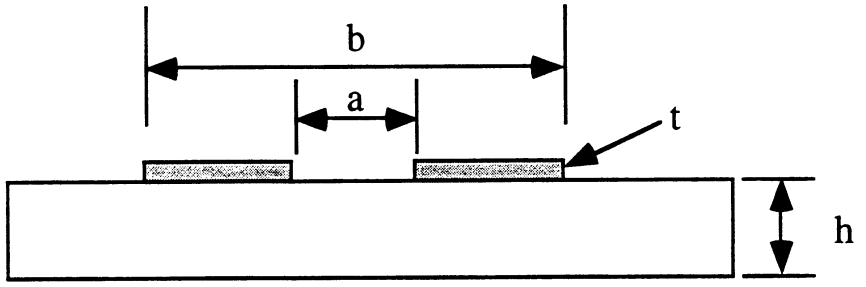

The characteristic impedance of the coplanar strip transmission line is given by the following equations:

$$Z_o = \frac{\eta_o}{\sqrt{\varepsilon_{eff}}}\left(\frac{K(k)}{K(k')}\right)$$

$$\varepsilon_{eff} = 1 + \left(\frac{\varepsilon_r - 1}{2}\right)\left(\frac{K(k')}{K(k)}\right)\left(\frac{K(k_1)}{K(k'_1)}\right)$$

$$k = \frac{a}{b}$$

$$k' = \sqrt{1.0 - k^2}$$

$$k'_1 = \sqrt{1.0 - k'^2_1}$$

$$k_1 = \frac{\sinh\left(\frac{\pi a}{4h}\right)}{\sinh\left(\frac{\pi b}{4h}\right)}$$

For three coplanar strips with the following geometry:

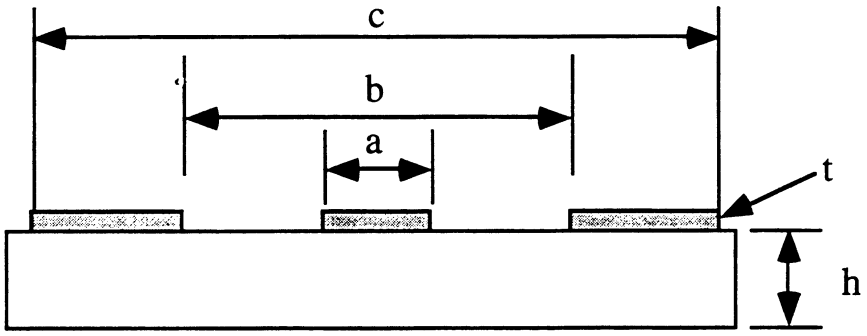

The characteristic impedance of the three coplanar strip transmission line is given by the following equations:

$$Z_o = \frac{\eta_o}{4\sqrt{\varepsilon_{eff}}}\left(\frac{K(k_1)}{K(k'_1)}\right)$$

$$\varepsilon_{eff} = 1 + \left(\frac{\varepsilon_r - 1}{2}\right)\left(\frac{K(k'_2)}{K(k_2)}\right)\left(\frac{K(k_1)}{K(k'_1)}\right) + \left(\frac{\varepsilon_r - 1}{2}\right)\left(\frac{K(k'_2)}{K(k_2)}\right)\left[\frac{K(k_1)}{K(k'_1)}\right]^2 x$$

$$\left(\frac{t}{b-a}\right) + \left[\left(\frac{t}{b-a}\right)\frac{K(k_1)}{K(k'_1)}\right]^2$$

$$k_2 = \frac{\sinh\left(\frac{\pi c}{4h}\right)}{\sinh\left(\frac{\pi b}{4h}\right)}\sqrt{\frac{\sinh^2\left(\frac{\pi b}{4h}\right) - \sinh^2\left(\frac{\pi a}{4h}\right)}{\sinh^2\left(\frac{\pi c}{4h}\right) - \sinh^2\left(\frac{\pi a}{4h}\right)}}$$

$$k_1 = \left(\frac{c}{b}\right)\sqrt{\frac{b^2 - a^2}{c^2 - a^2}}$$

$$k'_n = \sqrt{1 - k^2_n}$$

The following section is input and output of a Mathematica session that evaluates these equations as they pertain to the transmission lines developed for this work. This session is meant as a teaching aid for those who would like to use Mathematica for transmission line impedance calculations.

```
(* CPS and CPW Design Equations from Wadell  *)
(* pp. 73-74 and pp. 83-84.                  *)
(************ Initial Conditions ********************)
a=8; (* Center Gap Width                     *)
b=38; (* Center Gap Width plus 2x Conductor Width    *)
t=.5; (* Conductor Thickness                  *)
h=50; (* Substrate Height                     *)
er=3.78;(* Substrate Dielectric Constant          *)
Rs=.5; (* Surface resistivity of conductor       *)
(************ Design Equations for CPW - no ground *****)
at=a+(1.25*t/Pi)*(1.0+Log[4.0*Pi*a/t]);
bt=b-(1.25*t/Pi)*(1.0+Log[4.0*Pi*a/t]);
k=a/b;
kt=at/bt;
ktp=Sqrt[1-kt^2];
kp=Sqrt[1-k^2];
k1=Sinh[Pi*at/(4.0*h)]/Sinh[Pi*bt/(4.0*h)];
k1p=Sqrt[1-k1^2];
eeff=1.0+(0.5)*(er-1.0)*(EllipticK[kp]*EllipticK[k1])/
```

```
(EllipticK[k]*EllipticK[k1p]);
eefft=eeff-(eeff-1.0)/(1.0+((b-a)/(1.4*t))*
(EllipticK[k]/EllipticK[kp]));
ZoCPW=30.0*Pi*EllipticK[ktp]/(Sqrt[eefft]*EllipticK[kt]);
ZoCPS=(120.0*Pi)*EllipticK[k]/(Sqrt[eeff]*EllipticK[kp]);
(******* Conductor Loss Equations for CPS **********)
If[k<0.707,Pp=k*EllipticK[k]*(kp^(-1.5))/((1.0-kp)*EllipticK[kp]),
Pp=(Sqrt[k]*(1.0-k))^(-1)];
ac=(17.34*Rs*Pp/(ZoCPS*Pi*a))*(1.0+(b-a)/(2.0 a))*
((1.25/Pi)*Log[4.0*Pi*(b-a)/(2.0 t)]+1.0+((2.5 t)/(Pi*(b-a))))/
((1.0+((b-a)/a)+(1.25*t/(Pi a))*(1.0+Log[2.0*Pi*(b-a)/t]))^2)
Print["The effective dielectric constant (eeff)  is ",N[eeff]];
Print["The effective dielectric constant (eefft) is ",N[eefft]];
Print["The Characteristic Impedance of CPW is ",N[ZoCPW]];
Print["The Characteristic Impedance of CPS is ",N[ZoCPS]];
Print["The conductor loss in dB/m is ",N[ac]];

The effective dielectric constant (eeff)  is 2.45846
The effective dielectric constant (eefft) is 2.39402
The Characteristic Impedance of CPW is 112.705
The Characteristic Impedance of CPS is 121.37
The conductor loss in dB/m is 0.00558157


(* Three Conductor CPS Design Equations from Wadell  *)
(* pp. 87-88                                  *)
(************ Initial Conditions **********************)
a=10; (* Center Conductor Width                  *)
b=38; (* Center Cond. Width plus 2x Gap Width      *)
c=b+2*a; (* b+ 2x Outer Cond. Width               *)
t=.5; (* Conductor Thickness                     *)
h=50; (* Substrate Height                        *)
er=3.78;(* Substrate Dielectric Constant          *)
```

```
(************ Design Equations for CPW - no ground ***)
k1=(c/b)*Sqrt[(b*b-a*a)/(c*c-a*a)];
k1p=Sqrt[1-k1^2];

k2=(Sinh[Pi*c/(4.0*h)]/Sinh[Pi*b/(4.0*h)])*
Sqrt[((Sinh[Pi*b/(4.0*h)])^2-(Sinh[Pi*a/(4.0*h)])^2)/
((Sinh[Pi*c/(4.0*h)])^2-(Sinh[Pi*a/(4.0*h)])^2)];
k2p=Sqrt[1-k2^2];

eeff=1.0+((0.5)*(er-1.0)*(EllipticK[k2p]*EllipticK[k1])/
(EllipticK[k2]*EllipticK[k1p]))+(0.5*(er-1.0)*EllipticK[k2p]*(EllipticK[k1]^2)*t/
(EllipticK[k2]*(EllipticK[k1]^2)*(b-a)))+(2.0*t*EllipticK[k1]/((b-a)*EllipticK[k1p]))+
(t*EllipticK[k1]/((b-a)*EllipticK[k1p]))^2;

ZoCPS3=(120.0*Pi)*EllipticK[k1]/(4.0*Sqrt[eeff]*EllipticK[k1p]);
Print["The effective dielectric constant (eeff)  is ",N[eeff]];
Print["The Char. Impedance of Three Conductor CPS is ",N[ZoCPS3]];

The effective dielectric constant (eeff)  is 2.47162
The Char. Impedance of Three Conductor CPS is 120.584

(* Three Conductor CPS Design Equations from Wadell  *)
(* pp. 87-88                                  *)
(************ Initial Conditions **********************)
a=10; (* Center Conductor Width                  *)
b=.; (* Center Cond. Width plus 2x Gap Width       *)
c=b+2*a; (* b+ 2x Outer Cond. Width                *)
t=.5; (* Conductor Thickness                     *)
h=50; (* Substrate Height                        *)
er=3.78;(* Substrate Dielectric Constant          *)
(************ Design Equations for CPW - no ground ***)
k1=(c/b)*Sqrt[(b*b-a*a)/(c*c-a*a)];
k1p=Sqrt[1-k1^2];
```

```
k2=(Sinh[Pi*c/(4.0*h)]/Sinh[Pi*b/(4.0*h)])*
Sqrt[((Sinh[Pi*b/(4.0*h)])^2-(Sinh[Pi*a/(4.0*h)])^2)/
((Sinh[Pi*c/(4.0*h)])^2-(Sinh[Pi*a/(4.0*h)])^2)];
k2p=Sqrt[1-k2^2];

eeff=1.0+((0.5)*(er-1.0)*(EllipticK[k2p]*EllipticK[k1])/
(EllipticK[k2]*EllipticK[k1p]))+
(0.5*(er-1.0)*EllipticK[k2p]*(EllipticK[k1]^2)*t/
(EllipticK[k2]*(EllipticK[k1]^2)*(b-a)))+
(2.0*t*EllipticK[k1]/((b-a)*EllipticK[k1p]))+
(t*EllipticK[k1]/((b-a)*EllipticK[k1p]))^2;

ZoCPS3=(120.0*Pi)*EllipticK[k1]/(4.0*Sqrt[eeff]*EllipticK[k1p]);
pCPS3=Plot[ZoCPS3,{b,26,100}]
(* CPS and CPW Design Equations from Wadell  *)
(* pp. 73-74 and pp. 83-84.                  *)
(************ Initial Conditions **********************)
a=8; (* Center Gap Width                     *)
b=.; (* Center Gap Width plus 2x Conductor Width    *)
t=.5; (* Conductor Thickness                  *)
h=50; (* Substrate Height                     *)
er=3.78;(* Substrate Dielectric Constant           *)
(************ Design Equations for CPW - no ground *****)
at=a+(1.25*t/Pi)*(1.0+Log[4.0*Pi*a/t]);
bt=b-(1.25*t/Pi)*(1.0+Log[4.0*Pi*a/t]);
k=a/b;
kt=at/bt;
ktp=Sqrt[1-kt^2];
kp=Sqrt[1-k^2];
k1=Sinh[Pi*at/(4.0*h)]/Sinh[Pi*bt/(4.0*h)];
k1p=Sqrt[1-k1^2];
eeff=1.0+(0.5)*(er-1.0)*(EllipticK[kp]*EllipticK[k1])/
```

```
(EllipticK[k]*EllipticK[k1p]);
eefft=eeff-(eeff-1.0)/(1.0+((b-a)/(1.4*t))*
(EllipticK[k]/EllipticK[kp]));
ZoCPW=30.0*Pi*EllipticK[ktp]/(Sqrt[eefft]*EllipticK[kt]);
ZoCPS=(120.0*Pi)*EllipticK[k]/(Sqrt[eeff]*EllipticK[kp]);
pCPS=Plot[ZoCPS,{b,24,100}]
Show[pCPS,pCPS3]
```

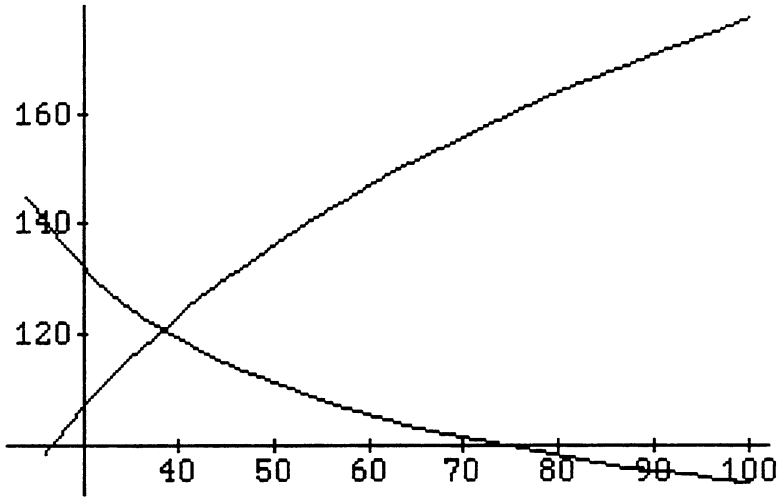

BIBLIOGRAPHY

BIBLIOGRAPHY

1. S. M. Joseph Liu, "Probe Design Extends On-Wafer Testing to 120 GHz," Microwaves and RF, pp. 104-110, June 1993.
2. 4. E. M. Godshalk, "A W-Band Wafer Probe," IEEE MTT-S International Microwave Symposium Digest, pp. 171-174, Vol. 1, 1993.
3. S. M. Joseph Liu, G. G.Boll, "A New Probe for W-Band On-Wafer Measurements," IEEE MTT-S International Microwave Symposium Digest, pp. 1335-1338, 1993.
4. R. Yu, M. Reddy, J. Pusl, S. Allen, M. Case, M. Rodwell, "Full Two-Port On-Wafer Vector Network Analysis to 120 GHz Using Active Probes," IEEE MTT-S International Microwave Symposium Digest, pp. 1339-1342, 1993.
5. R. Y. Yu, M. Case, M. Kamegawa, M. Sundaram, M. J. W. Rodwell, and A. W. Gossard, "275 GHz 3-Mask Integrated GaAs Sampling Circuit," Electronics Letters, Vol. 26, No. 13, June 21, 1990.
6. M. J. W. Rodwell, M. Kamegawa, R. Yu, M. Case, E. Carman, and K. S. Kiboney, "GaAs Nonlinear Transmission Lines for Picosecond Pulse Generation and Millimeter-Wave Sampling," IEEE Transactions on Microwave Theory and Techniques, Vol. 39, July 1991.
7. W. Mertin, C. Bohm, L. J. Balk, and E. Kubalek, "Two-dimensional field mapping in MMIC-substrates by electro-optic sampling technique," IEEE MTT-S Digest, pp. 1443-1446, 1992.
8. W. Mertin, C. Bohm, L. J. Balk, and E. Kubalek, "Two-dimensional field mapping of Amplitude and Phase of Microwave Fields inside a MMIC using the Direct Electro-Optic Technique," IEEE MTT-S Digest, pp. 1597-1600, 1994.
9. H. Cheng, J. F. Whitaker, "300 GHz Bandwidth Network Analysis Using Time-Domain Electro-Optic Sampling," IEEE MTT-S Digest, pp. 1355-1358, 1993.
10. H. J. Cheng, J. F. Whitaker, T. M. Weller, and L. P. B. Katehi, "Terahertz-Bandwidth Characteristics of Coplanar Transmission Lines on Low Permittivity Substrates," IEEE Transactions on Microwave Theory and Techniques, Vol. 42, Dec. 1994.
11. C. H. Lee, "Picosecond Optics and Microwave Technology," IEEE Transactions on Microwave Theory and Techniques, Vol. 38, pp. 596-607, May 1990.
12. W. Mertin, C. Roths, F. Taenzler, and E. Kubalek, "Probe Tip Invasiveness at Indirect Electro-Optic Sampling of MMIC," IEEE MTT-S International Microwave Symposium Digest, pp. 1351-1354, 1993.
13. W. Thomann, P. Russer, "Quasi-Simultaneous External Electro-Optic Probing of Transverse and Longitudinal Field Distributions taking into Account for Probe Tip Invasiveness," IEEE MTT-S International Microwave Symposium Digest, pp. 1601-1604, 1994.

14. G. David, W. Schroeder, D. Jäger, I. Wolff, "2D Electro-Optic Probing Combined with Field Theory Based Multimode Wave Amplitude Extraction: A New Approach to On-Wafer Measurement," IEEE MTT-S International Microwave Symposium Digest, pp. 1049-1052, 1995.

15. J. Wilson, J. F. B. Hawkes, Optoelectronics - An Introduction, 2nd Edition, Prentice Hall, New York, 1989.

16. K. Kamogawa, I. Toyoda, K. Nishikawa, T. Tokumitsu, "Characterization of a Monolithic Slot Antenna Using an Electro-Optic Sampling Technique," IEEE Microwave and Guided Wave Letters, Vol. 4, December 1994.

17. H. J. Cheng, personal communication, June 1995.

18. J. Bokor, A. M. Johnson, R. H. Storz, and W. M. Simpson, "High-Speed Circuit Measurements Using Photoemission Sampling," Applied Physics Letters, 49(4), July 28, pp. 226-228, 1986.

19. M. S. Hill, A. Gopinath, "Probing Gunn Domains at X-band Microwave Frequencies Using a Scanning Microscope," Journal of Physics D: Applied Physics, Vol. 7, pp. 69-77, 1974.

20. J. T. L. Thong, "Transit Time Effect in Electron Beam Testing Voltage Measurements," Measurement Science Technology, Vol. 3, pp. 827-837, 1992.

21. Park Scientific Instruments, "PSI Probe," Technical Newsletter from PSI, Spring 1993.

22. U. Mueller, C. Böhm, J. Sprengepiel, C. Roths, E. Kubalek and A. Beyer, "Geometrical and Voltage Resolution of Electrical Sampling Scanning Force Microscopy," IEEE Microwave Theory and Techniques Symposium Digest, pp. 1605-1608, 1994.

23. C. Böhm, C. Roths, and E. Kubalek, "Contactless Electrical Characterization of MMICs by Device Internal Electrical Sampling Scanning-Force-Microscopy," IEEE Microwave Theory and Techniques Symposium Digest, pp. 1605-1608, 1994.

24. S. S. Osofsky, S. E. Schwarz, "Design and Performance of a Non-Contacting Probe for Measurements of High Frequency Planar Circuits," IEEE Transactions on Microwave Theory and Techniques, Vol. 40, pp. 1701-1708, August 1992.

25. Y. Gao, I. Wolff, "A Miniature Magnetic Field Probe for Measuring Fields in Planar High-Frequency Circuits," IEEE Microwave Theory and Techniques Symposium Digest, pp. 1159-1162, 1995.

26. J. H. Richmond, "A Modulated Scattering Technique for the Measurement of Field Distributions," Inst. Radio Eng. Trans. MTT-3, pp. 13-15, 1955.

27. A. L. Cullen, J. C. Parr, "A New Perturbation Method for Measuring Microwave Fields in Free Space," Proceedings IEE B Vol. 102, pp. 836-844, 1955.

28. R. Justice, V. H. Rumsey, "Measurement of Electric Field Distributions," Institute of Radio Eng. Transactions, AP-3, pp. 177-180, 1955.

29. J. Zürcher, "A Near Field Measurement Method Applied to Planar Structures," Microwave Engineering Europe, pp. 43-51, June/July 1992.

30. S. A. Bokhari, J. F. Zürcher, J. R. Mosig, F. E. Gardiol, "Near Fields of Microstrip Antennas," IEEE Transactions on Antennas and Propagation, February 1995.

31. T. P. Budka, G. M. Rebeiz, "A Microwave Circuit Electric Field Imager," IEEE Microwave Theory and Techniques Symposium Digest, pp. 1139-1142, 1995.

32. T. P. Budka, E. M. Tentzeris, S. D. Waclawik, N. I. Dib, L. P. B. Katehi, G. M. Rebeiz, "An Experimental and Theoretical Comparison of the Electric Fields Above a Coupled Line Bandpass Filter," IEEE Microwave Theory and Techniques Symposium Digest, pp. 1487-1490, 1995.

33. J. F. Nye, G. Hygate, "Measuring a microwave field close to a conductor," Measurement Science Technology 2, pp. 838-845, 1991.

34. G. Hygate, J. F. Nye, "Measuring Microwave Fields Directly with an Optically Modulated Scatterer," Measurement Science Technology 1, pp. 703-709, 1990.

35. D. P. Neikirk, "Integrated Detector Arrays for High Resolution Far-Infrared Imaging," Doctoral Thesis, California Institute of Technology, Pasadena, California, 1984.

36. S. S. Gearhart, "Integrated Millimeter-Wave and Submillimeter-Wave Antennas and Schottky-Diode Receivers," Doctoral Thesis, The University of Michigan, Ann Arbor, Michigan, 1994.

37. M. Kanda, "Standard Probes for Electromagnetic Field Measurements," IEEE Transactions on Antennas and Propagation, AP-41, pp. 1349-1364, October 1993.

38. G. Smith, "Limitations on the Size of Electric-Field Probes," IEEE Transactions on Microwave Theory and Techniques, Vol. MTT-32, pp. 594-600, June 1984.

39. H. Bassen, G. Smith, "Electric Field Probes - A Review," IEEE Transactions on Antennas and Propagation, Vol. AP-31, No. 5, pp. 710-718, 1983.

40. Y. T. Lo, S. W. Lee, Antenna Handbook - Theory, Applications and Design, Van Nostrand Reinhold Company Inc., New York, 1988.

41. C. Balanis, Antenna Theory: Analysis and Design, Harper and Row, Publishers, New York, 1982.

42. R. S. Elliot, Antenna Theory and Design, Prentice-Hall, Inc., New Jersey, 1981.

43. Wadell, B. C., Transmission Line Design Handbook, Artech House, Boston, Massachusetts 1991.

44. E. M. Tentzeris, personal communication, 1995.

45. J. Gong, personal communication, 1995.

46. D. M. Pozar, Microwave Engineering, Addison-Wesley Publishing Co., Reading, Massachusetts 1993.

47. Harokopus, W. P., "High Frequency Characterization of Open Microstrip Discontinuities," Ph. D. Dissertation, The University of Michigan, Ann Arbor, Michigan, 1991.

48. K.S.Yee, "Numerical solution of initial boundary value problems involving Maxwell's equations in isotropic media," IEEE Transactions on Antennas and Propagation, Vol. AP-14, No.3, pp.302-307, May 1966.

49. G.Mur, "Absorbing boundary conditions for the finite-difference approximation of the time-domain electromagnetic-field equations," IEEE Trans. Electromagn. Compat., EMC-23, pp.377-382, Nov. 1981.

50. K.K.Mei and J.Fang, "Superabsorption-a method to improve absorbing boundary conditions", IEEE Transactions on Antennas and Propagation, AP-40, pp.1001-1010, Sept. 1992.

51. M. W. Trippe, S. Weinreb, S. W. Duncan, A. Eskandarian, B. A. Golja, D. C. Martel, G. Mendenilla, B. Power, H. B. Sequeira, S. B. Southwick, S. P. Svensson, D-W. Tu, and N. E. Byer, "mm-Wave MIMIC Receiver Components," IEEE Monolithic Circuits Symposium Digest, pp. 51-54, 1991.

52. M. Kim, J.J. Rosenberg, R.P. Smith, R.M. Weikle II, J.B. Hacker, M.P. Delisio and D.B. Rutledge, "A grid amplifier," IEEE Microwave GuidedWave Letters, Vol. 1, No. 11, pp. 322-324, 1991.

53. C. Chi and G. M. Rebeiz, "A Quasi-Optical Amplifier," IEEE Microwave and Guided Wave Letters, Vol. 3, pp. 164-166, June 1993.

54. G.V. Eleftheriades, W.A. Ali-Ahmad, L.P. Katehi and G.M. Rebeiz, "Millimeter-wave integrated horn antennas: Part I: Theory and Part II: Experiment," IEEE Transactions Antennas Propagation, Vol. AP-39, pp. 1575-1586, Nov. 1991.

55. G.V. Eleftheriades and G.M. Rebeiz, "Design and Analysis of Quasi-Integrated Horn Antennas for Millimeter and Submillimeter-Wave Applications," IEEE Transactions on Microwave Theory and Techniques, Vol. 41, No. 6/7, pp. 954-965, May 1993.

56. G. V. Eleftheriades, "Design and Analysis of Quasi-Integrated Horn Antennas for Millimeter and Submillimeter-Wave Applications," Ph.D. Thesis, University of Michigan, Ann Arbor, Michigan, 1993.

57. D. B. Rutledge, D. P. Neikirk, and D. P. Kasilingam, "Integrated Circuit Antennas," in Infrared and Millimeter-Waves, vol. 10, pp. 1-90, K. J. Button, Ed. New York: Academic Press, 1983.

58. David K. Lovelace, "Program De-embeds Wafer-Probed Data," Microwaves and RF, pp. 136-138, June 1993.

59. M. C. A. M. Koolen et al., "An Improved De-Embedding Technique for On-Wafer High-Frequency Characterization," Proceedings of the IEEE Bipolar Circuits and Technology Meeting, pp. 188-191, 1991.